Imperial College London

Department of Mechanical Engineering

Exhibition Road

London, SW7 2AZ

Development of an Implicit Framework for the Two-Fluid Model on Unstructured Grids

Paul Thomas Bartholomew

September 2017

Submitted for PhD degree of Imperial College London and the Diploma of Imperial College

Supervised by:

Prof. Berend van Wachem

Dr. Andrew J. Marquis

Copyright Declaration

Declaration of Originality

I hereby declare that the contents of this thesis is my own work. Where I have referred to the work of others, this has been appropriately referenced.

Paul Bartholomew, September 27, 2017

Abstract

The two-fluid model is an efficient method for simulating multiphase flows, based on an averaged description of the phases as interpenetrating and interacting continua. It is particularly attractive for the simulation of dispersed gas-solid flows in which the large number of particles in practical devices can impose an insurmountable computational burden for particle tracking methods, given currently available computing resources. Whilst the two-fluid model is more efficient than particle tracking methods, it results in large, strongly coupled and highly non-linear systems of equations, placing a premium on efficient solution algorithms. Additionally, the constitutive models used to describe the solid phase introduce stiff source terms, requiring a robust solution algorithm to handle them.

In this thesis a fully-coupled algorithm is developed for the two-fluid model, based on a Newton linearisation of the underlying equation system, resulting in an algorithm treating all inter-equation couplings implicitly. For comparison, a semi-coupled algorithm, based on a Picard linearisation of the two-fluid model is also implemented, yielding a smaller implicitly coupled pressure-velocity system and a segregated system for the transport of phase concentrations. Motivating this work is the highly non-linear nature of the two-fluid model and the stiff source terms arising in the models of the dispersed phase, these are treated explicitly in the semi-coupled algorithm and may impose stability limits on the algorithm. By treating these terms implicitly, it is expected that the fully-coupled solution algorithm will be more robust.

The algorithms are compared by application to test cases ranging from academic problems to problems representative of industrial applications of the two-fluid model. These comparisons show that with increasing problem complexity, the robustness of the fully-coupled algorithm leads to an overall more efficient solution than the semi-coupled algorithm.

Acknowledgement

Thanks are due to many people and if by omission I cause offence, I must apologise. First and foremost I would like to thank my supervisor Prof. Berend van Wachem whose expertise in the field of multiphase flows and advice have been invaluable throughout this project. The opportunity to work with a world leader in this field is an experience I will never forget. I would also like to thank Dr. Fred Marquis for his insight and guidance over the years and for inspiring me to pursue a career in research. This work was funded through a Doctoral Training Award from the Engineering and Physical Sciences Research Council and I am very grateful for their support.

To everyone I have had the pleasure of working with through various office moves, sharing discussions with you on a broad range of topics, both academic and otherwise, has been enlightening and your friendship has made this experience infinitely more enjoyable.

Finally I would like to thank my parents Chris and Siân Bartholomew for encouraging me in everything I have done. Without your constant support I would not have been able to achieve what I have and I dedicate this work to you.

Paul Bartholomew, September 27, 2018

Contents

List of Figures

List of Tables

Nomenclature

Acronyms

CFD Computational Fluid Dynamics

CFL Courant-Friedrich-Lewy number

CPU Central Processing Unit

DNS Direct Numerical Simulation

FC Fully-Coupled

FVM Finite Volume Method

IBM Immersed Boundary Method

idw inverse distance weighting

IPSA InterPhase Slip Algorithm

KTGF Kinetic Theory of Granular Flows

MWI Momentum Weighted Interpolation

PDF Probability Density Function

RANS Reynolds Averaged Navier Stokes

RHS Right Hand Side

SC Semi-Coupled

SIMPLE Semi-Implicit Method for Pressure Linked Equations

TVD Total Variation Diminishing

VOF Volume Of Fluid

Greek Symbols

ψ Generic variable [$\cdot$]

β Momentum exchange parameter [kg m^{-3} s^{-1}]

λ Bulk viscosity [Pa s]

ρ Density [kg m^{-3}]

Γ Diffusion coefficient []

γ_s Destruction of granular temperature through inelastic collisions [kg m^{-1} s^{-3}]

ϕ Generic variable [$\cdot$]

Θ_s Granular temperature [m^2 s^{-2}]

ψ Generic variable [$\cdot$]

ϑ Advecting velocity [m s^{-1}]

α Volume fraction [-]

μ Dynamic viscosity [Pa s]

$\boldsymbol{\delta}$ Kronecker delta

$\boldsymbol{\tau}$ Viscous stress tensor [Pa]

$\boldsymbol{\sigma}$ Stress tensor [Pa]

Latin Symbols

$\mathcal{C}(\cdot)$ Collision function [$\cdot$ s^{-1}]

$\mathcal{J}_s$ Production of granular temperature through fluctuating drag [kg m^{-1} s^{-3}]

$\mathcal{ML}$ Mass-loading [-]

$\mathcal{P}$ Production term [kg m^2 s^{-3}]

f Particle Probability Density Function

g_0 Radial distribution function [-]

$\mathbf{f}$ Force vector [N]

$\boldsymbol{\mathcal{R}}$ Reynolds stress tensor [Pa]

$\mathbf{a}$ Acceleration vector [m s^{-2}]

$\mathbf{c}^p$ Particle velocity [m s^{-1}]

$\mathbf{g}$ Gravity vector [m s^{-2}]

$\mathbf{J}$ Diffusive flux [$\cdot$ kg m^{-2} s^{-1}]

$\mathbf{u}$, $\mathbf{U}$ Velocity vector [m s^{-1}]

$\mathbf{x}$ Coordinate axis [m]

$\widehat{\mathbf{n}}$ Unit normal vector [-]

$\widehat{\mathbf{s}}$ Unit cell-to-cell vector [-]

A Area [m^2]

C^D Drag coefficient [-]

d^p Particle diameter [m]

I Interphase transfer operator [kg m^{-3} s^{-1}]

k Fluctuating turbulent kinetic energy [m^2 s^{-2}]

l Length scale [m]

l^f Interpolation coefficient [-]

m Mass [kg]

N Number of particles [-]

n	Number density of particles [m^{-3}]
p	Pressure [Pa]
Re	Reynolds number [-]
S	General source term [$\cdot\ \mathrm{s}^{-1}$]
St	Stokes number [-]
T	Temperature [K]
t	Time [s]
V	Volume [m^3]

Chapter 1

Introduction

Multiphase flows consisting of immiscible materials or "phases" can be found in a range of scientific and industrial applications from spray processes in combustion systems to interfacial flows through pipelines and large scale gas-solid flows in fluidised beds used for power generation for example. These flows may be classified according to their constituents *e.g.* gas-liquid, gas-solid, liquid-liquid, or the geometry of the phase interface; for instance, interfacial flows are characterised by bulk flows of pure[1] phases separated by large interfaces whilst dispersed multiphase flows consist of a continuous "carrier" fluid phase transporting a potentially large number of bubbles, droplets or particles. In principal, each of these problems can be approached using the same method: applying continuum mechanics within each phase and treating the phase interfaces as (moving) internal boundary conditions. This requires solving the equations of continuum mechanics within each phase in addition to tracking the position of the phase interfaces in order to apply the internal boundary conditions describing the interactions between the phases. When the number of interfaces is low, and information of the interface and its effect on the flow is important; for instance, studying the behaviour of individual bubbles, droplets or particles, such interface tracking methods may be applied. This necessarily implies a high resolution of simulation to resolve flow features around the interface and the interface itself. As the size of the domain grows, for example in the design of industrial plant, the ensuing range of scales between the interfaces and the domain of interest may be prohibitive in terms of the computational resources required to resolve the interfaces. Furthermore such level of detail may

[1] Here pure does not mean thermodynamically pure but that the bulk material consists of only a single phase *i.e.* a gas or a liquid phase.

be of limited use to the designer, for example, in the design of fluidised beds [58], information relating to individual particles is generally not required as the variables of design interest are the statistics of the particles, such as concentration, bulk velocity, rates of heat or mass transfer, *etc.*

The two-fluid model developed by Anderson and Jackson [2] and Ishii and Hibiki [48] is based on an averaged description of multiphase flows. The effect of this averaging procedure is that each phase is represented by a continuum occupying the entire domain, interpenetrating the other phase(s), whose presence is shown by their concentration. This introduces additional terms into the averaged transport equations for each phase as a result of jump conditions [48] at the phase interface representing the interactions between the phases, such as drag forces between a carrier fluid and dispersed particles. This is of particular interest for the simulation of dispersed multiphase flows in which the diameter of the particles may be of the order of 100 μm whilst the scale of the domain is of the order of 1 m. By using an averaging approach the need to resolve the flow around individual particles is removed, instead the interaction between the carrier fluid and the particles is modelled by means of a drag function. This leads to two related approaches: Eulerian-Lagrangian methods track particles as discrete point masses obeying Newton's laws of motion moving through a fluid phase; whilst Eulerian-Eulerian methods treat both the carrier and the dispersed phase as continuous fluids. In the context of developing numerical methods for the solution of dispersed multiphase flows, the representation of the dispersed phase as a fluid in the Eulerian-Eulerian two-fluid model enables the use of efficient methods developed over the past six decades to be applied to the solution of the governing equations of both phases. Furthermore, the amount of computational work is essentially independent of the number of particles[2], leading to further benefits when considering parallel implementations. In a Lagrangian particle tracking scheme an uneven distribution of particles throughout the domain may lead to load-balancing issues; whereas in an Eulerian-Eulerian simulation the distribution of work is determined by the partitioning of the mesh, for which effective algorithms have been developed to balance computational work and communication overhead.

[2]The models used to describe, for example, particle-particle interactions result in stiffer equations as the particle concentration increases, which may require additional effort to solve the nonlinearities in the equations.

1.1 Aims and Objectives

The focus of the work described in this thesis is to develop solution algorithms for the Eulerian-Eulerian two-fluid model for the simulation of dispersed gas-solid flows. It should be noted, however, that whilst this work focuses on dispersed gas-solid flows, the algorithms developed herein are generally applicable to the simulation of multiphase flows using the two-fluid model. Two algorithms are developed: one based on an implicit treatment of the pressure-velocity coupling with a segregated transport of the phases, referred to as the semi-coupled algorithm; and a novel fully-coupled algorithm treating the governing equations of the two-fluid model in a fully implicit manner.

Motivating the development of the fully-coupled algorithm is the highly non-linear nature of the two-fluid model governing equations. By treating the problem fully implicitly a superior convergence is expected compared to segregated approaches. Furthermore, the constitutive models used to describe a dispersed solid phase in the two-fluid model introduce stiff source terms. It is therefore desirable from the perspective of algorithm robustness to treat the problem fully implicitly. The developed algorithms are compared by application to a range of test cases including a fluidised bed as a representative practical application and turbulent dispersed gas-solid flow problems.

Following the development and implementation of the semi- and fully-coupled algorithms, the aim is to use them to investigate turbulent gas-solid flows. Two flows with experimental data are selected for this purpose: the backwards facing step flow of Fessler and Eaton [40] and the bluff body stabilised flow of Boree *et al.* [10].

In addition to the development of the aforementioned solution algorithms, a general problem in Computational Fluid Dynamics (CFD) is the prevention of pressure-velocity decoupling. This is a direct consequence of the discretisation of the governing equations yielding a set of algebraic equations in which changes in pressure at a point are not directly related to the velocity at that point and vice-versa, they are decoupled from each other. A well known remedy is the staggered variable arrangement proposed by Harlow and Welch [44] however this introduces significant implementation overhead, requiring a mesh per velocity component plus a mesh for the pressure field. Furthermore, it is difficult to extend staggered variable arrangements to non-Cartesian meshes as arise in the study of flows in complex domains. The problem of pressure-velocity

decoupling is exacerbated in the two-fluid model by the sharing of the pressure field between the multiple phases. A popular technique for preventing pressure-velocity decoupling on unstructured grids is the Momentum-Weighted Interpolation (MWI) technique proposed by Rhie and Chow [76]. A detailed study of MWI is undertaken to develop a form suitable for the two-fluid model which must be capable of handling the large and rapidly changing source terms and the strong interphase couplings typical of the two-fluid model. This analysis, starting from single phase flows shows that to maintain physical velocity fields in the presence of the above described source term fields the source terms must be discretised as a pressure field, consistent with the discretisation employed when discretising the fluid pressure field. It also shows that when there are large, discontinuous changes in density, as found in the mixture density in fluidised beds, it becomes necessary to apply a density weighting within MWI to prevent the lighter fluid being accelerated, resulting in instability or divergence of the solution.

1.2 Structure of Thesis

The thesis is structured as follows:

- In chapter 2 the discretisation of the governing equations of fluid flow using a collocated variable arrangement and the development of MWI for multiphase flows is presented. This includes the development of approaches for handling large and/or discontinuous source terms and discontinuous density fields, both of which feature in the two-fluid model[3], in the framework of MWI.

- In chapter 3 the semi- and fully-coupled solution algorithms are developed. An algorithm is required to solve the non-linearity inherent in the two-fluid model. The semi-coupled algorithm, based on the Picard linearisation, splits the two-fluid model equations into a pressure-velocity sub problem and a separate phase transport equation. This however results in a lag between the pressure-velocity and volume fraction solutions which may adversely affect convergence. To maintain the coupling between pressure, velocity and volume fraction, the fully-coupled algorithm uses a Newton linearisation of the two-fluid model, retaining the implicit coupling between the equations. The resulting system of

[3]In this work the density of each phase is assumed to be constant, however the local mixture density changes as a function of the local concentrations of each phase.

algebraic equations is larger, requiring greater computational effort to solve relative to the semi-coupled system of equations, although the implicit coupling is expected to enhance the robustness of the algorithm. Both algorithms are compared, using the semi-coupled algorithm as a baseline, by application to: an advected volume fraction pulse; horizontal and vertical flows; and a fluidised bed, representative of a real world application of a two-fluid model solver. The results show that in the simple cases of horizontal and vertical flow, there is little to choose between the algorithms. In simulating the fluidised bed, the fully-coupled algorithm proved more computationally efficient, however it did not exhibit the greater stability relative to the semi-coupled algorithm that was expected.

- In chapter 4 the fully-coupled algorithm is further tested by its application to turbulent gas-solid flows. Two test cases are examined: the backwards facing step investigated experimentally by Fessler and Eaton [40] and the case of particles injected into the jet of a bluff body stabilised flow investigated by Boree *et al.* [10].

- Conclusions are drawn and suggestions for further work are presented in chapter 5. In developing the MWI for multiphase flows it is shown that particular care must be taken around features of the flow field which cause discontinuities in the pressure gradient, for example discontinuities in the source term or density fields. It is shown that by treating source terms as inducing a pressure gradient they can be discretised consistently with the fluid pressure gradient, ensuring a balance of forces on the discrete level which if not satisfied results in unphysical velocity fields. It is also shown that the density weighting proposed by Denner and van Wachem [31] to handle flows with discontinuous density fields stabilises the solution by reducing the pressure gradient at the interface to the value satisfying momentum in the lighter fluid, preventing large accelerations that lead to divergence. These modifications are required due to the inability of a linear approximation of the pressure field to represent the discontinuous changes in pressure gradient, future work could involve studying alternative pressure gradient discretisations to better handle these situations. The development of the semi- and fully-coupled algorithms shows that there is generally little to choose between the two, however the fully-coupled algorithm did out perform the semi-coupled algorithm in terms of time-to-solution for the fluidised bed test case. Both algorithms are implemented using off-the-shelf black box linear equation

solvers and preconditioners as provided by the `PETSc` library [4, 5, 43], it is proposed that the fully-coupled algorithm in particular would benefit from the development of a custom preconditioner, for example a SIMPLE-type preconditioner [55].

Chapter 2

Discretisation of the Governing Equations on Collocated Meshes

In this chapter, the discretisation of the governing equations of fluid flow is presented. The discretisation is performed in the context of the Finite Volume Method (FVM) using a collocated variable arrangement, suitable for simulating flows in complex domains. A well known issue arising in the use of collocated variable arrangements is the occurrence of so-called '*chequerboard*' pressure fields due to the application of simple discretisation approaches that do not respond to changes in pressure and velocity at a point leading to a spatial decoupling of the pressure and velocity fields. This is complicated in the two-fluid model by the sharing of a single pressure field by two velocity fields. In this work, Momentum-Weighted Interpolation (MWI) attributed to the work of Rhie and Chow [76] is used to prevent the above described pressure-velocity decoupling, this is developed by considering its application to flows described by a single fluid, sharing features common to the two-fluid model such as large or discontinuous source terms.

The material in this chapter has been submitted for publication:
P. Bartholomew, F. Denner, H.M. Abdol-Azis, A.J. Marquis, B.G.M. van Wachem, *Unified formulation of the momentum-weighted interpolation for collocated variable arrangements*, (2017), submitted to Journal of Computational Physics.

2.1 Introduction

The coupling of pressure and velocity is a key difficulty of simulating incompressible flows and has been a central topic of Computational Fluid Dynamics (CFD) for the past decades [39, 71, 97]. The difficulties associate with the pressure-velocity coupling can be illustrated by assuming an isothermal, incompressible flow, which is governed by the momentum equations

$$\rho\left(\frac{\partial u_j}{\partial t}+\frac{\partial u_j u_i}{\partial x_i}\right)=-\frac{\partial p}{\partial x_j}+\frac{\partial \tau_{ij}}{\partial x_i}+S_j \tag{2.1}$$

and the continuity equation

$$\frac{\partial u_i}{\partial x_i}=0\ , \tag{2.2}$$

where ρ is the density, $\boldsymbol{u}$ the velocity, p is the pressure, $\boldsymbol{\tau}$ is the viscous stress tensor, $\boldsymbol{S}$ are the source terms, t is time and $\boldsymbol{x}$ is the coordinate axis. Aside from the question of how to solve the strongly coupled pressure and velocity fields, the governing equations of a three-dimensional incompressible flow only provide three independent equations for four unknowns (three velocity components plus pressure), which makes the formulation of an equation for pressure based on the governing flow equations non-trivial and has lead to a variety of segregated [39, 71, 94] and coupled [79, 80, 92] algorithms. Furthermore, discretising the pressure gradient on the one-dimensional equidistant mesh shown in *fig.* 2.1 using central differencing yields

$$\left.\frac{\partial p}{\partial x}\right|^P \approx \frac{p^E-p^W}{2\Delta x}\ , \tag{2.3}$$

where Δx is the mesh spacing. The pressure gradient at node P is, crucially, not dependent on the pressure value at node P, irrespective of the algorithm applied to solve the governing equations. Consequently, the governing equations permit two independent pressure fields in a *chequerboard* pattern [39, 94] as a valid solution to the discrete equations, a result that naturally extends to higher dimensions.

Pressure-velocity decoupling is a discretisation issue typically associated with incompressible flows. When compressible flows are considered, most numerical frameworks use density as a primary variable, while pressure is determined indirectly via an appropriate equation of state. Although such density-based algorithms are the method of choice when the compressibility of

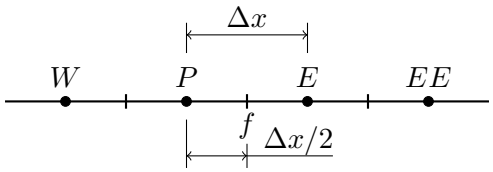

Figure 2.1: One-dimensional example of an equidistant mesh, where Δx is the mesh spacing.

the flow is appreciable, they are ill-suited for flows with low Mach numbers [17, 97], in particular in the incompressible limit. Motivated by the desire to compute flows at all speeds with the same numerical framework, a number of pressure-based algorithms for flows at all speeds have been developed, *e.g.* [12, 21, 29, 98]. However, the insignificant compressibility of flows with low Mach number admits pressure-velocity decoupling in the compressible flow solution on meshes with collocated variable arrangement.

Historically, pressure and velocity were coupled by staggering the points at which pressure and velocity are evaluated, the *staggered variable arrangement*, as proposed by Harlow and Welch [44], with velocity typically evaluated at the centres of the cell-faces, while all other variables are evaluated and stored at the cell centres. A staggered variable arrangement enforces a natural coupling between pressure and velocity, and yields a very compact stencil for the pressure gradient that drives the velocity at the adjacent cell centres through the momentum equations. There is no doubt that for Cartesian meshes, a staggered variable arrangement is efficient and effective. However, as CFD has matured as a tool, it has found ever more frequent application to analyse flows in complex geometries, represented by unstructured meshes, for which the application of a staggered variable arrangement is difficult and may include complex corrections to account for meshes of relatively poor quality [73, 96]. This difficulty, in conjunction with the bookkeeping overhead associated with staggered variable arrangements [70], has motivated the development of discretisation methods for *collocated variable arrangements*, in which all variables are stored at cell centres, that prevent the pressure-velocity decoupling ensuing as a result of the scenario presented in Eq. (2.3). Notable methods that allow robust computations on meshes with collocated variable arrangement are the MWI, based on the work of several researchers in the early 1980s [72] and widely attributed to Rhie and Chow [76], the artificial compressibility method [15] and one-sided differencing [37], of which MWI is by far the most widely used at present [67].

The principle of the MWI is to evaluate the velocity at the faces based on weighting coefficients that are derived from the discretised momentum equations, including pressure gradients. By construction, the MWI emulates a staggered variable arrangement, introducing a cell-to-cell pressure coupling and implementing a low-pass filter acting on the third and higher derivatives of pressure [28, 39, 59, 97] to suppress pressure-velocity decoupling, while preserving the second-order accuracy of traditional finite volume methods [30, 39, 97, 101]. However, as originally proposed by Rhie and Chow [76], the MWI only considers the coupling between pressure gradients with the advection and shear stress terms of the momentum equations, neglecting contributions of the transient term, source terms and originating from under-relaxation. A range of modifications to the original formulation of the MWI have been proposed that account for under-relaxation [62, 65] and transient terms [14, 20, 59, 70, 81, 90, 99, 100]. Recently, Xiao *et al.* [98] showed that neglecting transient terms in the MWI for the simulation of unsteady problems results in a dispersion error for the propagation of pressure waves in compressible flows. Including source terms in the MWI was discussed by Rahman *et al.* [75] with the motivation to maintain a strong pressure-velocity coupling, which may otherwise be masked when the source terms are large, due to the direct coupling between source terms and the pressure gradient. Subsequently, van Wachem and Gopala [86] and Mencinger and Zun [64] demonstrated that the inclusion of source terms follows directly from the governing equations, by presenting coherent derivations of the MWI from the momentum equations, and demonstrated the efficacy of the proposed formulation using multiphase flows, especially two-phase flows with surface tension that yield sharp discontinuous source terms. Building upon this work, Denner and van Wachem [31] presented an MWI formulation for flows with source terms, and including transient contributions, on arbitrary meshes. When computing flows with source terms, the MWI necessitates a *force-balanced* discretisation [30] to avoid the production of spurious velocities as a result of a mismatch of the discretisations applied to the pressure gradients and the source terms. In a force-balanced discretisation the pressure gradients and the source terms are discretised with equivalent methods, so that the forces applied to the flow by the source terms can be precisely balanced by the corresponding pressure gradients. More recent work [68, 85, 101] has focused on source terms arising in porous media, which follows a similar procedure as the inclusion of source terms in multiphase flows. Curiously, much of the published work on MWI remains focused on Cartesian meshes, although modifications required for arbitrary meshes have already been

proposed [13, 14, 23, 30, 31, 64, 102]. This spread of separate developments, typically focusing on a single aspect of MWI, has led to a large number of subtly differing approaches; to this date, a unified and consistent formulation of the MWI is not available.

The objective of this work is the derivation of a unified and consistent formulation of the MWI, which is applicable to arbitrary meshes (structured and unstructured meshes), with discontinuous source terms and varying fluid densities, suitable for the simulation of single phase and multiphase flows. The MWI is derived from the discretised momentum equations, which leads to a consistent formulation of the MWI and provides a firm theoretical basis. The presented analysis and numerical results show that the key property of the MWI is a low-pass filter enforced on the third and higher derivatives of pressure, including a cell-to-cell pressure coupling, which suppresses oscillatory solutions, while maintaining second-order accuracy with respect to the mesh spacing. In order for this filter to be retained in flows with source terms, the discretisation has to ensure that the low-pass filter is only applied to the driving pressure gradient that is associated with the fluid motion, by carefully accounting for the source terms in the MWI. To this end, a force-balanced discretisation of the source terms is proposed, that precisely matches the discretisation of the pressure gradients for smooth as well as discontinuous source terms, and preserves the force applied to the flow. A range of representative test cases are used to scrutinise the efficacy of the proposed formulation of the MWI, and to compare it to previously published formulations of the MWI. The proposed formulation of the MWI is shown to provide a robust pressure-velocity coupling, even for flows on meshes of poor quality, and for flows with discontinuous source terms, as well as discontinuous density changes of up to six orders of magnitude, with similar or reduced errors compared to existing MWI formulations.

The applied numerical frameworks for incompressible and compressible flows are briefly introduced in §2.2. In §2.3, the MWI is derived from the discretised momentum equations for arbitrary meshes and validated on structured and unstructured meshes. An extension of the MWI for the inclusion of source terms is proposed in §2.4 and the density weighting of the MWI for flows with discontinuous changes in density is discussed in §2.5. Based on the presented step-by-step analysis of the MWI, a unified formulation of the MWI is proposed in §2.6. The chapter is concluded in §2.7.

2.2 Numerical Framework

The governing equations for incompressible flow, Eq. (2.1) and Eq. (2.2), are discretised using the finite volume method, with the semi-discretised equations for cell P, shown schematically in *fig.* 2.2, given as

$$\rho^P \left(\left. \frac{\partial u_j}{\partial t} \right|^P V^P + \sum_f u_j^f \vartheta^f A^f \right) = - \left. \frac{\partial p}{\partial x_j} \right|^P + \sum_f \tau_{ij}^f \hat{n}_i^f A^f + S_j^{\star,P} V^P \ , \tag{2.4}$$

$$\sum_f \vartheta^f A^f = 0 \ , \tag{2.5}$$

where superscript f denotes the faces of cell P, A^f is the area of face f, $\hat{\boldsymbol{n}}^f$ is the unit normal vector of face f (outward pointing with respect to cell P), $\vartheta^f = \boldsymbol{u}^f \cdot \hat{\boldsymbol{n}}^f$ is the advecting velocity, $\boldsymbol{S}^{\star,P}$ are the discretised source terms, and V^P is the volume of cell P. In this study, the transient term in the momentum equations, Eq. (2.4), is discretised using the first-order or second-order backward Euler schemes, while the face velocity u_j^f is evaluated using the central differencing scheme with an implicit correction for mesh skewness [34]. Deriving a consistent discretisation for the advecting velocity

$$\vartheta^f = u_i^f \hat{n}_i^f = \overline{u}_i^f \hat{n}_i^f + f(\boldsymbol{\nabla} p, \boldsymbol{S}^\star, \rho) \tag{2.6}$$

based on the MWI, where $\overline{u}_i^f$ is interpolated from the adjacent cell centres, and constructing a force-balanced discretisation of the source term $\boldsymbol{S}^{\star,P}$ are the main objectives of this study. The MWI presented in §2.3 and its extensions to flows with source terms and density discontinuities in §2.4 and §2.5, respectively, are tested using the fully-coupled finite volume framework for single phase and multiphase flows on arbitrary meshes of Denner and van Wachem [31].

The low Mach number flows presented in §2.3.5 are simulated using the pressure-based finite volume framework for single phase flows at all speeds of Xiao *et al.* [98]. For compressible flows the momentum equations are

$$\frac{\partial \rho u_j}{\partial t} + \frac{\partial \rho u_j u_i}{\partial x_i} = - \frac{\partial p}{\partial x_j} + \frac{\partial \tau_{ij}}{\partial x_i} + S_j \tag{2.7}$$

and the continuity equation is

$$\frac{\partial \rho}{\partial t} + \frac{\partial \rho u_i}{\partial x_i} = 0 \ . \tag{2.8}$$

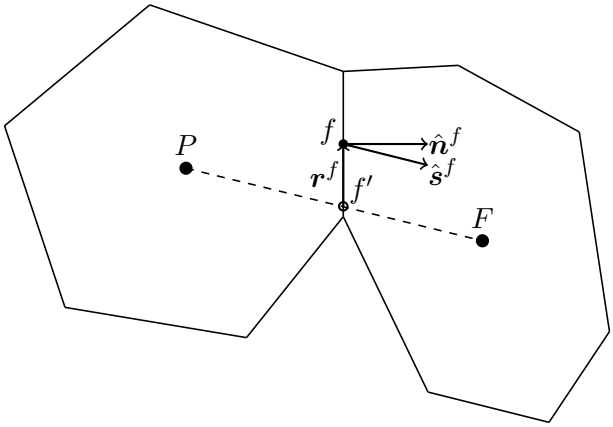

Figure 2.2: Schematic illustration of cell P with its neighbour cell F and the shared face f, where $\hat{\boldsymbol{n}}^f$ is the unit normal vector of face f and $\hat{\boldsymbol{s}}^f$ is the unit vector connecting cells P and F (both outward pointing with respect to cell P), with f' the interpolation point associated with face f and $\boldsymbol{r}^f$ the vector from interpolation point f' to face centre f.

In addition to the momentum and continuity equations, compressible flow is governed by the energy equation

$$\frac{\partial \rho h}{\partial t} + \frac{\partial \rho u_i h}{\partial x_i} = \frac{\partial p}{\partial t} + \frac{\partial}{\partial x_i}\left(\tau_{ij} u_j\right) + S_i u_i \ , \tag{2.9}$$

where $h = c_p T + \boldsymbol{u}^2/2$ is the total enthalpy, c_p is the specific heat capacity at constant pressure, and T is the temperature. Without loss of generality, heat conduction is neglected in this work. The considered fluid is assumed to be an ideal gas with the density given by the equation of state

$$\rho = \frac{p}{(\gamma - 1) c_v T} \ , \tag{2.10}$$

with $\gamma = c_p/c_v$ the heat capacity ratio and c_v the specific heat capacity at constant volume. In particular, the continuity equation, Eq. (2.8), is discretised as [98]

$$\frac{\partial \rho}{\partial t} + \sum_f \rho^{f,n} \vartheta^{f,n+1} A^f + \sum_f \rho^{f,n+1} \vartheta^{f,n} A^f - \sum_f \rho^{f,n} \vartheta^{f,n} A^f = 0 \ , \tag{2.11}$$

following a Newton-linearisation of the advection term, where superscript $n+1$ denotes values that are implicitly solved for and superscript n denotes deferred values from the previous iteration. This Newton-linearisation of the advection term of the discretised continuity equation, Eq. (2.11), allows simulations without MWI, contrary to the employed incompressible framework. The interested reader is referred to the work of Xiao *et al.* [98] for a detailed description of this

numerical framework and discretisation.

2.3 Momentum-Weighted Interpolation

The MWI is derived from the momentum equations with the aim of providing a consistent formulation of the advecting velocity ϑ^f, Eq. (2.6), for arbitrary meshes and to analyse the general properties of the MWI. Using an appropriate approximation for the values at face centre f, such as a linear interpolation of values at adjacent cell centres, a first-order Euler scheme to discretise the transient term and neglecting source terms, Eq. (2.4) is given at cell centre P as

$$\left(a^P + \frac{\rho^P}{\Delta t} V^P\right) u_j^P + \sum_f a^F u_j^F = -\left.\frac{\partial p}{\partial x_j}\right|^P V^P + \frac{\rho^{P,O} u_j^{P,O}}{\Delta t} V^P \ , \tag{2.12}$$

where Δt is the applied time-step, superscript O denotes values from the previous time-level, superscript F represents the neighbour cell of cell P that is adjacent to face f, as schematically illustrated in *fig.* 2.2, and a is the sum of the coefficients of the advection term and the shear stress term arising from the discretisation applied to the momentum equations. By defining

$$\tilde{u}_j^P = -\frac{1}{a^P} \sum_f a^F u_j^F \ , \tag{2.13}$$

$$d^P = \frac{V^P}{a^P} \ , \tag{2.14}$$

$$c^P = \frac{\rho^P}{\Delta t} \ , \tag{2.15}$$

Eq. (2.12) can be rewritten as

$$\left(1 + c^P d^P\right) u_j^P = \tilde{u}_j^P - d^P \left.\frac{\partial p}{\partial x_j}\right|^P + c^P d^P u_j^{P,O} \ . \tag{2.16}$$

Note that in the analysis presented here, a backwards Euler scheme with first-order accuracy is used for time integration; the extension to higher-order accurate transient schemes is straightforward [20, 54]. Assuming Eq. (2.16) can be similarly formulated for any control volume, an equivalent equation is written for cell F

$$\left(1 + c^F d^F\right) u_j^F = \tilde{u}_j^F - d^F \left.\frac{\partial p}{\partial x_j}\right|^F + c^F d^F u_j^{F,O} \tag{2.17}$$

and, in analogy to a staggered control volume, at face f

$$\left(1 + c^f d^f\right) u_j^f = \tilde{u}_j^f - d^f \left.\frac{\partial p}{\partial x_j}\right|^f + c^f d^f u_j^{f,O} \ , \tag{2.18}$$

thus mimicking a staggered variable arrangement. However, in the absence of a staggered variable arrangement, the information required to close Eq. (2.18) is not directly available and, consequently, approximations for $\tilde{u}_j^f$, c^f, d^f and $(\partial p/\partial x_j)^f$ are required.

With the aim of obtaining an expression for the velocity u_j^f, $\tilde{u}_j^f$ is approximated by linear interpolation as

$$\tilde{u}_j^f \approx \overline{\tilde{u}}_j^f = l^f \tilde{u}_j^P + \left(1 - l^f\right) \tilde{u}_j^F \ , \tag{2.19}$$

where l^f is the linear interpolation coefficient. Note that this definition for $\tilde{u}_j^f$ is chosen so that the expression for u_j^f is time-step independent, *i.e.* the steady-state solution should not contain any terms that are dependent on the time-step and the MWI should recover the steady-state solution if a transient flow reaches a steady state [66]. Substituting Eq. (2.16) and Eq. (2.17) into Eq. (2.19), the face velocity u_j^f, given by Eq. (2.18), becomes

$$\left(1 + c^f d^f\right) u_j^f = \left.\overline{(1 + cd)\, u_j}\right|^f - \left(d^f \left.\frac{\partial p}{\partial x_j}\right|^f - \left.\overline{d\frac{\partial p}{\partial x_j}}\right|^f\right) + \left(c^f d^f u_j^{f,O} - \left.\overline{c d u_j^O}\right|^f\right) \ , \tag{2.20}$$

where $\overline{(\cdot)}^f$ denotes a value at face f obtained by linear interpolation from the adjacent cell centres. With $\Delta t \to \infty$ for a steady-state solution, $c \to 0$ and Eq. (2.20) reduces to

$$u_j^f = \overline{u}_j^f - \left(d^f \left.\frac{\partial p}{\partial x_j}\right|^f - \left.\overline{d\frac{\partial p}{\partial x_j}}\right|^f\right) \ , \tag{2.21}$$

which is independent of the time-step Δt.

2.3.1 Velocity Interpolation

The face velocity $\overline{u}_i^f$ is interpolated with a linear interpolation

$$\overline{u}_i^f = l^{f,(\mathrm{idw})} u_i^P + \left(1 - l^{f,(\mathrm{idw})}\right) u_i^F \ , \tag{2.22}$$

where

$$l^{f,(\mathrm{idw})} = \frac{\Delta q^{Ff}}{\Delta q^{Pf} + \Delta q^{Ff}} \tag{2.23}$$

is the interpolation coefficient obtained by *inverse distance weighting*, indicated by the superscript "(idw)", and Δq^{Pf} and Δq^{Ff} are the distances between cell centre P and face f and between cell centre F of the adjacent cell and face f, respectively. The accuracy of the interpolated face velocity $\overline{u}_i^f$ reduces when the interpolation point f' along the vector connecting the cell centres P and F does not coincide with the centre of face f, see *fig.* 2.2, commonly referred to as *mesh skewness*. In order to retain the accuracy of the linear interpolation, a gradient-based correction is added to the interpolation of the face velocity [28, 53], with the face velocity following as

$$\overline{u}_i^f = l^{f,(\mathrm{idw})} u_i^P + \left(1 - l^{f,(\mathrm{idw})}\right) u_i^F + \left.\overline{\frac{\partial u_i}{\partial x_j}}\right|^f r_j^f \ , \tag{2.24}$$

where $\boldsymbol{r}^f$ is the vector from interpolation point f' to face centre f, see *fig.* 2.2. Note that the precise type of interpolation is not critical and the correction of mesh skewness is optional, as it does not have a direct influence on the efficacy of the MWI in providing a robust pressure-velocity coupling, although the interpolation given in Eq. (2.24) is desirable with respect to the accuracy of the interpolation on non-Cartesian meshes [53, 67].

2.3.2 The Pressure Gradients

The discretisation and interpolation of the pressure gradients in the MWI has a direct influence on the low-pass filter properties with regards to the pressure field, which is widely considered to be the key characteristic of the MWI [30, 31, 39, 75, 99], and the efficacy of the associated pressure-velocity coupling. First, the interpolation on an equidistant mesh is discussed, and the low-pass filter on the pressure field is derived, to illustrate the key concepts of the MWI. This is followed by a generalisation of the interpolation and the low-pass filter to non-equidistant meshes.

2.3.2.1 Equidistant Mesh

The applied numerical framework is based on a finite volume method, so that the straightforward discretisation of the pressure gradients on the one-dimensional equidistant mesh shown in *fig.* 2.1

follows as

$$\left.\frac{\partial p}{\partial x}\right|^{f} \approx \frac{p^{E}-p^{P}}{\Delta x} \ , \tag{2.25}$$

$$\left.\frac{\partial p}{\partial x}\right|^{P} \approx \frac{p^{E}-p^{W}}{2\Delta x} \ , \tag{2.26}$$

$$\left.\frac{\partial p}{\partial x}\right|^{E} \approx \frac{p^{EE}-p^{P}}{2\Delta x} \ . \tag{2.27}$$

As the mesh is equidistant, a linear interpolation of the pressure gradients at cells P and E with a 1/2-weighting is given as

$$\left.\overline{\frac{\partial p}{\partial x}}\right|^{f} \approx \frac{1}{2}\left(\left.\frac{\partial p}{\partial x}\right|^{P} + \left.\frac{\partial p}{\partial x}\right|^{E}\right) \ . \tag{2.28}$$

Inserting the discretised pressure gradients given in Eq. (2.25) - Eq. (2.27), including the interpolation given in Eq. (2.28) and neglecting the weighting term d^{f} for simplicity, the pressure term of Eq. (2.21) at face f is given as

$$\left.\frac{\partial p}{\partial x}\right|^{f} - \frac{1}{2}\left(\left.\frac{\partial p}{\partial x}\right|^{P} + \left.\frac{\partial p}{\partial x}\right|^{E}\right) \approx \frac{1}{4\Delta x}\left(p^{W} - 3p^{P} + 3p^{E} - p^{EE}\right) \ . \tag{2.29}$$

For comparison, the third-order derivative of pressure at face f is given as

$$\left.\frac{\partial^{3} p}{\partial x^{3}}\right|^{f} \approx \frac{1}{\Delta x}\left(\left.\frac{\partial^{2} p}{\partial x^{2}}\right|^{E} - \left.\frac{\partial^{2} p}{\partial x^{2}}\right|^{P}\right) \approx -\frac{1}{\Delta x^{3}}\left(p^{W} - 3p^{P} + 3p^{E} - p^{EE}\right) + \mathcal{O}\left(\Delta x^{4}\right) \ , \tag{2.30}$$

which shows that the pressure term in Eq. (2.29) is proportional to the third-order derivative of pressure,

$$\left.\frac{\partial p}{\partial x}\right|^{f} - \frac{1}{2}\left(\left.\frac{\partial p}{\partial x}\right|^{P} + \left.\frac{\partial p}{\partial x}\right|^{E}\right) \approx -\left.\frac{\partial^{3} p}{\partial x^{3}}\right|^{f} \frac{\Delta x^{2}}{4} \ . \tag{2.31}$$

It is this relationship that dampens out non-physical pressure oscillations on meshes with collocated variable arrangement [30, 39, 75, 94, 99]. Approximating the pressure gradient at face f with standard finite differences as in Eq. (2.25), provides a spatial cell-to-cell coupling of the pressure field and matches the discretised pressure gradient that would be employed if f would correspond to a control volume in a staggered variable arrangement. Moreover, the pressure term is proportional to Δx^{2}, see Eq. (2.31), and, hence, the second-order accuracy of the finite-volume framework is preserved [97]. The extension to multiple dimensions is straightforward by

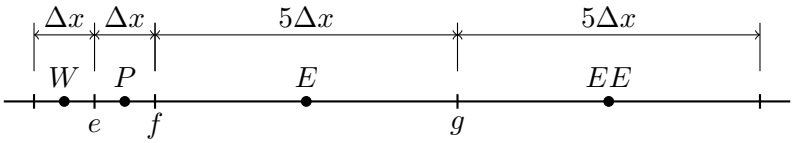

Figure 2.3: One-dimensional example of a mesh with a change in mesh spacing.

computing the cell-centred gradients using the divergence theorem, given for cell P as

$$\left.\frac{\partial p}{\partial x_i}\right|^P \approx \frac{1}{V^P}\sum_f \overline{p}^f \hat{n}_i^f A^f \ , \tag{2.32}$$

where f are all faces adjacent to cell P, and analogously for cell E.

2.3.2.2 Non-Equidistant Meshes

The choice of interpolation coefficient for the pressure gradients on non-equidistant meshes is a controversial issue in the literature and has not been conclusively settled. The use of a linear interpolation with weighting coefficients based on the mesh geometry is frequently advocated [12, 13, 14, 20, 21, 23, 25, 64, 70], *e.g.* inverse distance weighting [13, 14, 20, 64] or volume weighting [25], for the interpolation of the pressure gradients. However, previous studies [30, 31, 39, 99] suggested the use of the 1/2-weighting given in Eq. (2.28) also for non-equidistant meshes, in order to retain the filter properties of the MWI. Pascau [70] also suggested the use of a harmonic average for all interpolations in the MWI, but did not further elaborate on the suitability of harmonic averaging.

Consider the example illustrated in *fig.* 2.3, where the mesh spacing suddenly changes by a factor of $\Delta x^E/\Delta x^P = 5$ in the cells adjacent to face f. Applying inverse distance weighting to interpolate the cell-centred pressure values to faces e, f and g, the derivatives required for the pressure term of the MWI follow as

$$\left.\frac{\partial p}{\partial x}\right|^f \approx \frac{p^E - p^P}{3\Delta x} \ , \tag{2.33}$$

$$\left.\frac{\partial p}{\partial x}\right|^P \approx \frac{\overline{p}^f - \overline{p}^e}{\Delta x} = \frac{1}{\Delta x}\left(\frac{1}{6}p^E + \frac{2}{6}p^P - \frac{3}{6}p^W\right) \ , \tag{2.34}$$

$$\left.\frac{\partial p}{\partial x}\right|^E \approx \frac{\overline{p}^g - \overline{p}^f}{5\Delta x} = \frac{1}{5\Delta x}\left(\frac{1}{2}p^{EE} + \frac{1}{3}p^E - \frac{5}{6}p^P\right) \ , \tag{2.35}$$

and the pressure term of the MWI, which is also interpolated with inverse distance weighting, becomes

$$\left.\frac{\partial p}{\partial x}\right|^f - \left(\frac{5}{6}\left.\frac{\partial p}{\partial x}\right|^P + \frac{1}{6}\left.\frac{\partial p}{\partial x}\right|^E\right) \approx -\frac{1}{180\Delta x}\left(3p^{EE} - 33p^E + 105p^P - 75p^W\right) \ . \tag{2.36}$$

The third derivative of pressure in this case is

$$\left.\frac{\partial^3 p}{\partial x^3}\right|^f \approx \frac{1}{3\Delta x}\left(\left.\frac{\partial^2 p}{\partial x^2}\right|^E - \left.\frac{\partial^2 p}{\partial x^2}\right|^P\right) \approx \frac{1}{225\Delta x^3}\left(3p^{EE} - 33p^E + 105p^P - 75p^W\right) + \mathcal{O}\left(\Delta x^4\right) \ , \tag{2.37}$$

so that the pressure term of the MWI is

$$\left.\frac{\partial p}{\partial x}\right|^f - \left(\frac{5}{6}\left.\frac{\partial p}{\partial x}\right|^P + \frac{1}{6}\left.\frac{\partial p}{\partial x}\right|^E\right) \approx -\left.\frac{\partial^3 p}{\partial x^3}\right|^f \frac{5}{4}\Delta x^2. \tag{2.38}$$

Similar relationships can be found in the same manner for any ratio $\Delta x^E/\Delta x^P$ and it can, therefore, be concluded, that the pressure term of the MWI is formally equivalent to the corresponding third derivative of pressure,

$$\left.\frac{\partial p}{\partial x}\right|^f - \left.\overline{\frac{\partial p}{\partial x}}\right|^f \approx \left.\frac{\partial p}{\partial x}\right|^f - \left[l^{f,(\mathrm{idw})}\left.\frac{\partial p}{\partial x}\right|^P + \left(1 - l^{f,(\mathrm{idw})}\right)\left.\frac{\partial p}{\partial x}\right|^P\right] \propto -\left.\frac{\partial^3 p}{\partial x^3}\right|^f , \tag{2.39}$$

if inverse distance weighting is applied consistently for all interpolations of pressure and its gradients.

If the cell-centred pressure gradients are, however, evaluated with face values obtained with inverse distance weighting, see Eq. (2.34) and Eq. (2.35), but interpolated in the MWI with 1/2-weighting, the resulting pressure term, for instance given for a cell-size ratio of $\Delta x^E/\Delta x^P = 5$ as

$$\left.\frac{\partial p}{\partial x}\right|^f - \frac{1}{2}\left(\left.\frac{\partial p}{\partial x}\right|^P + \left.\frac{\partial p}{\partial x}\right|^E\right) \approx -\frac{1}{12\Delta x}\left(3p^{EE} - p^E + p^P - 3p^W\right) \ , \tag{2.40}$$

is not proportional to the corresponding third derivative of pressure, Eq. (2.37), and does not formally provide the low-pass filter on the pressure field. Yet, if the 1/2-weighting is applied throughout, *i.e.* for the interpolation of $\overline{p}^e$, $\overline{p}^f$ and $\overline{p}^g$ as well as in the interpolation of the cell-centred pressure gradients in the MWI, the filter on the pressure field, then given by Eq. (2.31), would be retained, albeit at the cost of reducing the accuracy of the pressure gradient evaluation.

This reduced accuracy of the pressure gradient introduces an error in the momentum equation that, based on the Taylor expansion

$$\overline{p}^{f,(1/2)} = \overline{p}^{f,(\mathrm{idw})} + \left(x^{f,(1/2)} - x^{f,(\mathrm{idw})}\right) \left.\frac{\partial p}{\partial x}\right|^f + \mathcal{O}\left(\left(x^{f,(1/2)} - x^{f,(\mathrm{idw})}\right)^2\right) \ , \tag{2.41}$$

where superscript "(1/2)" denotes interpolation with 1/2-weighting, is proportional to the distance $x^{f,(1/2)} - x^{f,(\mathrm{idw})}$ and, thus, increases linearly with increasing cell-size ratio of adjacent cells. The influence of these different interpolation techniques is further analysed from a practical viewpoint using numerical results in §2.3.5.1.

2.3.3 Weighting Coefficients c and d

In Eq. (2.20) the weighting coefficients c and d appear in various forms, at face f as well as interpolated to face f from the values at adjacent cells P and F. This can be further simplified by observing that the pressure term of the MWI has to vanish and $\boldsymbol{u}^f = \overline{\boldsymbol{u}}^f$, if the pressure gradient is constant or varies linearly (assuming a steady state), for which $\partial^3 p/\partial x^3 = 0$. Furthermore, $\boldsymbol{u}^{f,O} = \overline{\boldsymbol{u}}^{f,O}$ if an initially transient flow assumes a steady-state solution.

To assure $\boldsymbol{u}^f = \overline{\boldsymbol{u}}^f$ if the gradient of pressure is constant or varies linearly, the coefficient of the interpolated face velocity $\overline{\boldsymbol{u}}^f$ has to be unity. Hence,

$$\left.\overline{1 + cd}\right|^f = 1 + c^f d^f \ , \tag{2.42}$$

and similarly for the coefficients of the previous time-step

$$\left.\overline{cd}\right|^f = c^f d^f \tag{2.43}$$

to obtain $\boldsymbol{u}^{f,O} = \overline{\boldsymbol{u}}^{f,O}$ at steady state. Taking Taylor expansions of the pressure gradients about the face centre f on an equidistant mesh,

$$\left.\frac{\partial p}{\partial x_i}\right|^P = \left.\frac{\partial p}{\partial x_i}\right|^f - \frac{\Delta x}{2} \left.\frac{\partial^2 p}{\partial {x_i}^2}\right|^f + \frac{\Delta x^2}{8} \left.\frac{\partial^3 p}{\partial {x_i}^3}\right|^f - \mathcal{O}(\Delta x^3) \ , \tag{2.44}$$

$$\left.\frac{\partial p}{\partial x_i}\right|^F = \left.\frac{\partial p}{\partial x_i}\right|^f + \frac{\Delta x}{2} \left.\frac{\partial^2 p}{\partial {x_i}^2}\right|^f + \frac{\Delta x^2}{8} \left.\frac{\partial^3 p}{\partial {x_i}^3}\right|^f + \mathcal{O}(\Delta x^3) \ , \tag{2.45}$$

the pressure term of the MWI is given as

$$d^f \left.\frac{\partial p}{\partial x_i}\right|^f - d\overline{\left.\frac{\partial p}{\partial x_i}\right|^f} = \left(d^f - \frac{d^P + d^F}{2}\right) \left.\frac{\partial p}{\partial x_i}\right|^f + \frac{\Delta x}{2}\left(\frac{d^P - d^F}{2}\right) \left.\frac{\partial^2 p}{\partial {x_i}^2}\right|^f - \frac{\Delta x^2}{8}\left(\frac{d^P + d^F}{2}\right) \left.\frac{\partial^3 p}{\partial {x_i}^3}\right|^f . \tag{2.46}$$

Therefore, for the pressure term of the MWI to vanish for a constant or linearly varying pressure gradient, d^f becomes

$$d^f = \frac{d^P + d^F}{2} \tag{2.47}$$

with

$$d^P - d^F = 0 \tag{2.48}$$

which is satisfied by the approximation

$$d^P \approx d^F \ . \tag{2.49}$$

While the approximation given in Eq. (2.49) has been applied in a somewhat *ad-hoc* manner by other researchers [20, 21, 23, 31, 59, 99, 101], generally without justification beyond the difference $d^P - d^F$ is assumed to be small [75, 99], the above analysis shows that it is necessary to obtain a physical solution.

Inserting the approximations defined in Eq. (2.42), Eq. (2.43), Eq. (2.47) and Eq. (2.49) into Eq. (2.20), and dividing by $1 + c^f d^f$, the face velocity becomes

$$u_i^f = \overline{u}_i^f - \hat{d}^f \left(\left.\frac{\partial p}{\partial x_i}\right|^f - \overline{\left.\frac{\partial p}{\partial x_i}\right|^f} \right) + c^f \hat{d}^f \left(u_i^{f,O} - \overline{\left.u_i^O\right|^f} \right) \ , \tag{2.50}$$

where

$$\hat{d}^f = \frac{d^f}{1 + c^f d^f} \ . \tag{2.51}$$

The corrections to the interpolated velocity provided by the pressure term and the transient term in Eq. (2.50) vanish if the pressure gradient is constant or varies linearly and if the flow assumes a steady state, respectively. The coefficients c^f and d^f do, therefore, not affect the low-pass filter or the cell-to-cell pressure coupling of the pressure term.

2.3.4 Advecting Velocity

Noting that the velocity $\boldsymbol{u}^f$, given by Eq. (2.50), appears in the discretised governing equations, Eq. (2.4) and Eq. (2.5), as the dot product with the face normal vector $\hat{\boldsymbol{n}}^f$, an *advecting velocity* $\vartheta^f = \boldsymbol{u}^f \cdot \hat{\boldsymbol{n}}^f$ can be defined using the MWI (*cf.* [23, 31, 39]). Applying the closures as described in the previous sections, §2.3.1-§2.3.3, this advecting velocity is given as

$$\vartheta^f = \overline{u}_i^f \hat{n}_i^f - \hat{d}^f \left(\frac{p^F - p^P}{\Delta x} - \left. \overline{\frac{\partial p}{\partial x_i}} \right|^f \hat{n}_i^f \right) + c^f \hat{d}^f \left(\vartheta^{f,O} - \overline{u}_i^{f,O} \hat{n}_i^f \right) \ . \tag{2.52}$$

When the vectors $\hat{\boldsymbol{s}}^f$ and $\hat{\boldsymbol{n}}^f$ are not parallel, as for instance in the example given in *fig.* 2.2, the pressure gradients at cell centres are misaligned to the pressure gradient at the face, because

$$\frac{p^F - p^P}{\Delta s^f} \approx \left. \frac{\partial p}{\partial x_i} \right|^f \hat{s}_i^f \not\approx \left. \frac{\partial p}{\partial x_i} \right|^f \hat{n}_i^f \ , \tag{2.53}$$

where Δs^f is the distance between cell centres P and F ($\Delta s^f = \Delta x$ on an orthogonal mesh where $\hat{\boldsymbol{s}}^f = \hat{\boldsymbol{n}}^f$). Consequently, the pressure term of the MWI is no longer guaranteed to constitute a low-pass filter with respect to the third and higher derivatives of pressure. The pressure filter can be restored by applying a deferred-correction approach [27, 28], as previously applied to the MWI by Zwart [102] and Denner and van Wachem [31], and similarly proposed by Ferziger and Perić [39], decomposing the product $\boldsymbol{\nabla} p^f \cdot \hat{\boldsymbol{n}}^f$ into an orthogonal and a non-orthogonal part. The pressure gradient at face f is then defined as

$$\left. \frac{\partial p}{\partial x_i} \right|^f \hat{n}_i^f \approx \zeta^f \left. \frac{\partial p}{\partial x_i} \right|^f \hat{s}_i^f + \left. \overline{\frac{\partial p}{\partial x_i}} \right|^f (\hat{n}_i^f - \zeta^f \hat{s}_i^f) \approx \zeta^f \frac{p^F - p^P}{\Delta s^f} + \left. \overline{\frac{\partial p}{\partial x_i}} \right|^f (\hat{n}_i^f - \zeta^f \hat{s}_i^f) \ , \tag{2.54}$$

where ζ^f is the scaling factor of the decomposition. Inserting Eq. (2.54) into the pressure term of Eq. (2.52), the pressure term for non-orthogonal meshes follows as

$$\left(\left. \frac{\partial p}{\partial x_i} \right|^f - \left. \overline{\frac{\partial p}{\partial x_i}} \right|^f \right) \hat{n}_i^f \Rightarrow \zeta^f \left(\left. \frac{\partial p}{\partial x_i} \right|^f - \left. \overline{\frac{\partial p}{\partial x_i}} \right|^f \right) \hat{s}_i^f \ . \tag{2.55}$$

Hence, the correction assures that the entire pressure term of the MWI is projected onto the vector $\hat{\boldsymbol{s}}^f$ connecting the adjacent cell centres, a prerequisite to retain the filter properties of the MWI on arbitrary meshes. The scaling factor ζ^f of the decomposition can be chosen arbitrarily in the range $0 \leq \zeta^f \leq 1$; the filter properties of the MWI are mesh-independent for $\zeta^f = 1$.

Denner and van Wachem [31] applied $\zeta^f = (\hat{n}_i^f \hat{s}_i^f)^{-1}$, which increases the weight of the pressure filter with increasing non-orthogonality of the mesh, while Zwart [102] suggested the use of $\zeta^f = \hat{n}_i^f \hat{s}_i^f$, which reduces the weight of the pressure filter with increasing non-orthogonality of the mesh.

In summary, applying the approximations presented above, the advecting velocity for steady-state and transient flows on arbitrary meshes is given as

$$\vartheta^f = \overline{u}_i^f \hat{n}_i^f - \zeta^f \hat{d}^f \left(\frac{p^F - p^P}{\Delta s^f} - \left. \overline{\frac{\partial p}{\partial x_i}} \right|^f \hat{s}_i^f \right) + c^f \hat{d}^f \left(\vartheta^{f,O} - \overline{u}_i^{f,O} \hat{n}_i^f \right) \ , \tag{2.56}$$

where inverse distance weighting should be applied for the interpolations. Applying this advecting velocity in the discretisation of the governing equations, Eq. (2.4) and Eq. (2.5), assuming source terms (separately discussed in §2.4) are negligible, enforces the spatial coupling of the pressure field that is otherwise missing. A careful choice of the approximations results in a low-pass filter that targets third-order and higher oscillations of pressure, that appear in a decoupled pressure field.

2.3.4.1 Momentum-Weighted Interpolation as a Low-Pass Pressure Filter

As shown in Eq. (2.31), the pressure term in the MWI is proportional to the third-order derivative of pressure, the MWI may thus be written as

$$\vartheta^f \approx \overline{u}_i^f \widehat{n}_i^f - \widehat{d}^f \frac{\Delta x^2}{4} \left. \frac{\partial^3 p}{\partial x_i^3} \right|^f \widehat{n}_i^f \ . \tag{2.57}$$

Using this representation, it will be shown that MWI operates as a low-pass filter acting on third-order and higher derivatives of pressure. To illustrate this, consider the case of fully developed flow and suppose that the discrete velocity field and pressure gradient are correct and satisfy the momentum and continuity equations, *i.e.*

$$u_j^P = \text{const.} \tag{2.58}$$

$$\left. \frac{\partial p}{\partial x_j} \right|^P = \text{const.} \tag{2.59}$$

at each cell centre. As the analysis surrounding Eq. (2.3) in §2.1 shows, the discretisation does not prevent odd-even decoupling of the pressure field. Considering also the discrete continuity equation for incompressible flow results in a constant advecting velocity, and substituting Eq. (2.58) into Eq. (2.57) yields

$$\widehat{d}^f \frac{\Delta x^2}{4} \left. \frac{\partial^3 p}{\partial x_i^3} \right|^f \widehat{n}_i^f = \text{const.} \tag{2.60}$$

The only value of the third-order derivative satisfying both the constraints imposed by Eq. (2.59) and Eq. (2.60) is zero, an alternating value as that which would arise in odd-even decoupling of the pressure field would violate the discrete continuity equation, whilst a constant non-zero value is incompatible with Eq. (2.59). Pressure fields with only lower order derivatives, in particular constant or linearly varying gradients, are however unaffected by Eq. (2.60), therefore MWI can be considered as a filter acting on third-order and higher derivatives of pressure to prevent pressure-velocity decoupling.

2.3.5 Numerical Experiments

Two representative test cases are considered, the propagation of acoustic waves in §2.3.5.1 and the flow in a lid-driven cavity in §2.3.5.2, to assess the different formulations of the MWI discussed in this section. The propagation of acoustic waves allows a detailed analysis of the effect of the pressure interpolation and the filter properties of the MWI, while the lid-driven cavity demonstrates the versatility and robustness of the proposed formulation.

2.3.5.1 Propagation of Acoustic Waves

The propagation of acoustic waves is simulated on one- and two-dimensional non-equidistant meshes. Three different formulations of the pressure gradients in the MWI and in the momentum equations, based on the analysis presented in §2.3.2, are considered:

1. The pressure at faces and the discretised pressure gradients in the MWI are interpolated with inverse distance weighting, abbreviated “p-idw, MWI-idw”;

2. The pressure at faces is interpolated with inverse distance weighting, while the discretised pressure gradients in the MWI are interpolated with 1/2-weighting, abbreviated “p-idw, MWI-1/2”;

3. The pressure at faces and the discretised pressure gradients in the MWI are interpolated with 1/2-weighting, abbreviated "p-1/2, MWI-1/2".

It is important to remember at this point, as previously discussed in §2.3.2, that the same discretised cell-centred pressure gradients are applied in the momentum equations and the MWI, and that the interpolated pressure at faces is used to determine these discretised cell-centred pressure gradients via the divergence theorem, see Eq. (2.32). The acoustic waves are excited by the velocity at the domain-inlet, $u_{\text{in}} = u_0 + \Delta u_0 \sin(2\pi f t)$, where $u_0 = 0.30886\,\text{m}\,\text{s}^{-1}$ is the initial velocity, $\Delta u_0 = 0.01 u_0$ is the excitation amplitude and $f = 1000\,\text{s}^{-1}$ is the excitation frequency. Initially, the pressure is $p_0 = 10^5\,\text{Pa}$ and the temperature is $T_0 = 24.80\,\text{K}$. The heat capacity ratio and the specific heat capacity at constant volume are $\gamma = 1.4$ and $c_v = 720\,\text{J}\,\text{kg}^{-1}\,\text{K}^{-1}$, respectively, from which a density of $\rho_0 = 14\,\text{kg}\,\text{m}^{-3}$ and a speed of sound of $u_{\text{s},0} = \sqrt{\gamma p_0/\rho_0} = 100\,\text{m}\,\text{s}^{-1}$ follow. Hence, the wavelength of the acoustic waves is $\lambda_0 = u_{\text{s},0}/f = 0.1\,\text{m}$. The flow is assumed to be inviscid, meaning the amplitude of the acoustic waves is not attenuated by viscous stresses. Since the density and velocity amplitudes are small, with $\Delta\rho_0 \ll \rho_0$ and $\Delta u_0 \ll u_{\text{s},0}$, the theoretical pressure amplitude of the acoustic waves follows from linear acoustic theory [1] as $\Delta p_0 = u_{\text{s},0}\rho_0\Delta u_0 = 4.32\,\text{Pa}$.

The one-dimensional domain is represented by a mesh with a sharp change in mesh spacing at $x = 0$, similar to the mesh shown in *fig.* 2.3, changing from a small mesh spacing Δx_{S} to a large mesh spacing $\Delta x_{\text{L}} = \lambda_0/20$. Figure 2.4 shows the pressure profiles on the meshes with $\Delta x_{\text{L}}/\Delta x_{\text{S}} \in \{5, 20\}$ for the three considered formulations of the pressure gradients. In all cases, the pressure profile is not visually affected by the choice of the pressure gradient formulation or the cell-size ratio of the mesh, with the predicted amplitude of the pressure wave in the range $4.30\,\text{Pa} \leq \Delta p \leq 4.35\,\text{Pa}$, which is in excellent agreement with the theoretical value of $\Delta p_0 = 4.32\,\text{Pa}$. Interestingly, the pressure amplitude of the acoustic waves does not diminish as they propagate through the domain, indicating that the proposed formulation of the MWI does *not* introduce spurious pressure contributions or damping that alters the pressure field, provided that the pressure waves are appropriately resolved in space and time. However, the profiles of the velocity gradient, shown in *fig.* 2.5, reveal distinct differences between the pressure gradient formulation that uses exclusively inverse distance weighting ('p-idw, MWI-idw'), which does not exhibit any dependency on the cell-size ratio $\Delta x_{\text{L}}/\Delta x_{\text{S}}$, and the other two considered

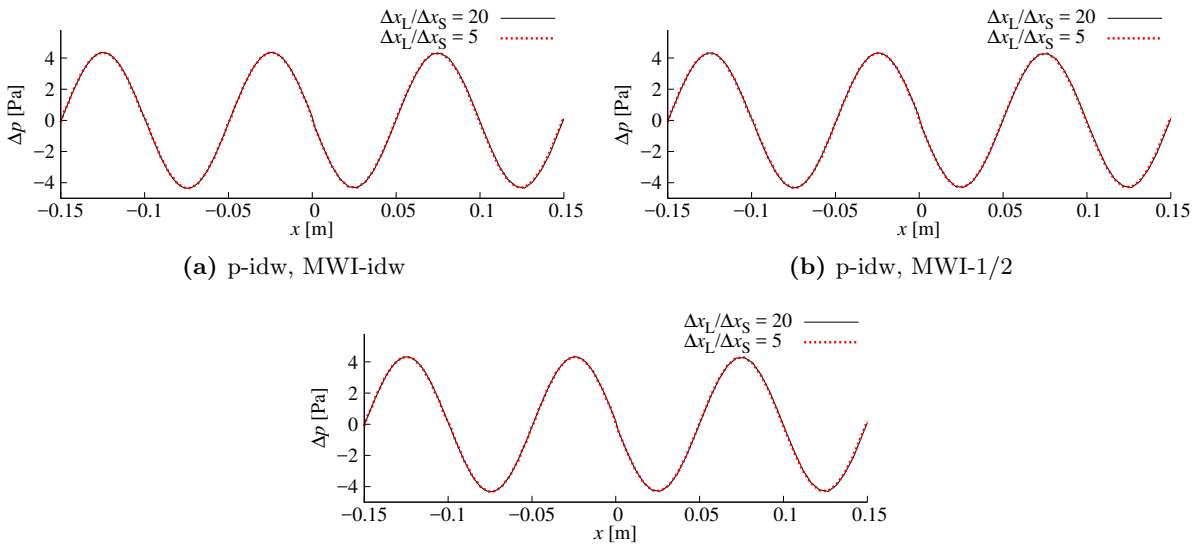

(a) p-idw, MWI-idw

(b) p-idw, MWI-1/2

(c) p-1/2, MWI-1/2

Figure 2.4: Pressure profiles of acoustic waves in a one-dimensional domain with velocity amplitude $\Delta u_0 = 0.01 u_0$ and frequency $f = 1000\,\mathrm{s}^{-1}$, on meshes with different cell-size ratios $\Delta x_\mathrm{L}/\Delta x_\mathrm{S}$ of the change in mesh spacing at $x = 0$, for different interpolation procedures of the pressure at faces and of the cell-centred pressure gradients.

formulations of the pressure gradient ('p-idw, MWI-1/2' and 'p-1/2, MWI-1/2'), which exhibit a considerable error at the position of the change in mesh spacing ($x = 0$). In fact, *fig.* 2.6 shows that this error grows linearly with $\Delta x_\mathrm{L}/\Delta x_\mathrm{S}$, as expected from Eq. (2.41).

Simulating the propagation of these acoustic waves on the hybrid quatrilateral/triangular two-dimensional mesh shown in *fig.* 2.7 (with periodic boundary conditions in the y-direction) using the formulations 'p-idw, MWI-idw' and 'p-idw, MWI-1/2' yields similar conclusions. The pressure profiles obtained with both formulations, shown in *fig.* 2.8a, are in excellent agreement with each other and show no visible dependency on the mesh. Moreover, the pressure amplitude ($\Delta p = 4.33\,\mathrm{Pa}$ with both formulations) and wavelength ($\lambda = 0.1\,\mathrm{m}$ with both formulations) compare very well with the corresponding theoretical values ($\Delta p_0 = 4.32\,\mathrm{Pa}$, $\lambda_0 = 0.1\,\mathrm{m}$). However, a visible error in the profile of the velocity gradient can be identified in *fig.* 2.8b for the 'p-idw, MWI-1/2' formulation at the positions ($x = 0.25\,\mathrm{m}$ and $x = 0.30\,\mathrm{m}$) where the mesh size (and cell type) changes. Although, contrary to the corresponding one-dimensional case, this error is not entirely eliminated with the 'p-idw, MWI-idw' formulation, which is attributed to mesh skewness, the error is significantly reduced.

In the formulation using 'p-idw, MWI-1/2', the error originates in the MWI, because the

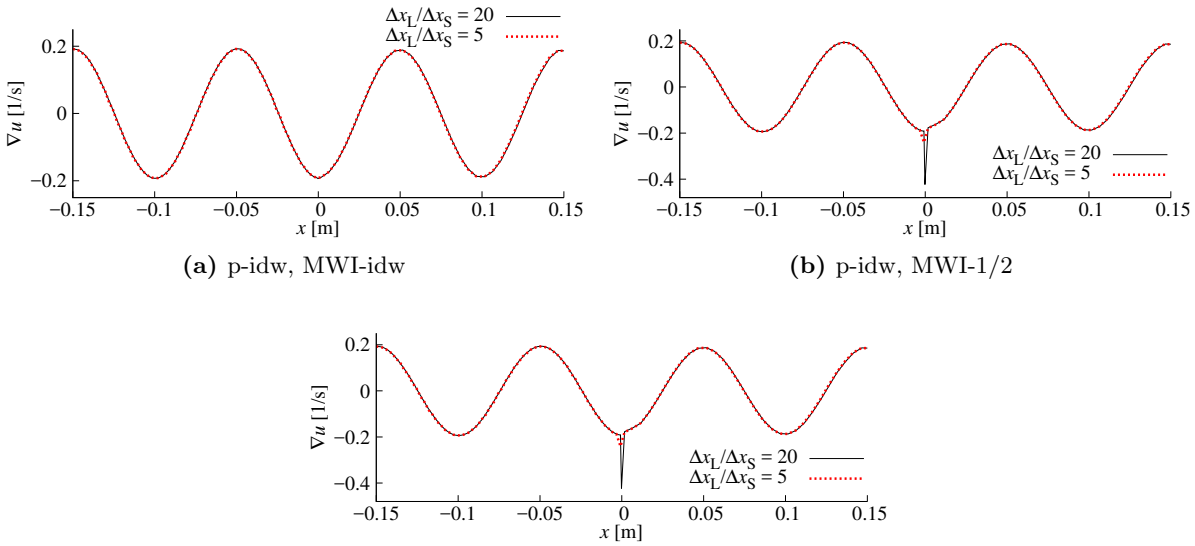

(a) p-idw, MWI-idw

(b) p-idw, MWI-1/2

(c) p-1/2, MWI-1/2

Figure 2.5: Profiles of the velocity gradient of acoustic waves in a one-dimensional domain with velocity amplitude $\Delta u_0 = 0.01 u_0$ and frequency $f = 1000\,\mathrm{s}^{-1}$, on meshes with different cell-size ratios $\Delta x_\mathrm{L}/\Delta x_\mathrm{S}$ of the change in mesh spacing at $x = 0$, for different interpolation procedures of the pressure at faces and of the cell-centred pressure gradients.

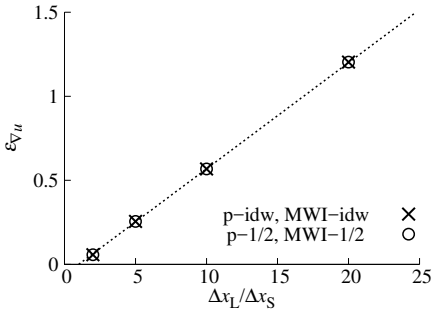

Figure 2.6: Error in velocity gradient ∇u for acoustic waves in a one-dimensional domain as a function as cell-size ratio $\Delta x_\mathrm{L}/\Delta x_\mathrm{S}$, observed in cells adjacent to the change in mesh spacing, for different interpolation procedures of the pressure at faces and of the cell-centred pressure gradients.

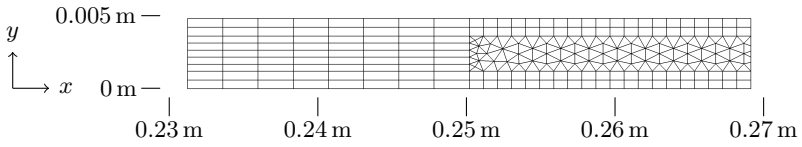

Figure 2.7: Hybrid quatrilateral/triangular two-dimensional mesh with dimensions $0.55\,\mathrm{m} \times 0.005\,\mathrm{m}$, used to simulate the propagation of acoustic waves. The coordinates in the x- and y-direction are shown as a reference. The triangular mesh section extends from $x = 0.25\,\mathrm{m}$ to $x = 0.30\,\mathrm{m}$. Note that not the entire extent of the mesh in the x-direction is shown, in order for the change in mesh type and mesh spacing to be clearly visible.

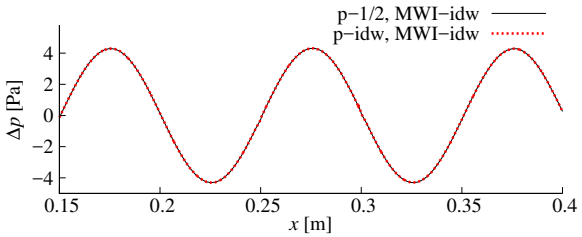

(a) Pressure p

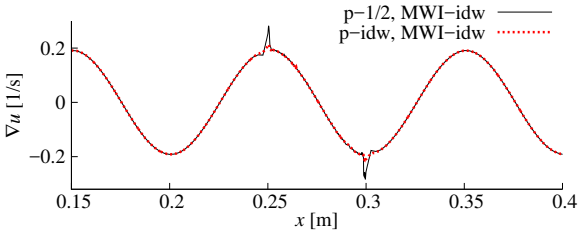

(b) Velocity gradient ∇u

Figure 2.8: Profiles of (a) the pressure and (b) the velocity gradient of acoustic waves, with velocity amplitude $\Delta u_0 = 0.01 u_0$ and frequency $f = 1000\,\mathrm{s}^{-1}$, on the hybrid quatrilateral/triangular two-dimensional mesh shown in *fig.* 2.7, using different interpolation procedures of the pressure at faces and of the cell-centred pressure gradients. The transition from quatrilateral to triangular mesh and vice versa is at $x = 0.25\,\mathrm{m}$ and $x = 0.30\,\mathrm{m}$, respectively.

pressure term of the MWI is not equivalent to the corresponding third derivative of pressure and, hence, violates the filter of the MWI, *cf.* Eq. (2.37) and Eq. (2.40). For the formulation with 'p-1/2, MWI-1/2', the pressure term of the MWI formally is equivalent to the corresponding third derivative of pressure and satisfies the low-pass filter on the pressure field. However, due to the interpolation of the face values of pressure with 1/2-weighting, the cell-centred pressure gradients adjacent to the change in mesh spacing are inaccurate and, therefore, introduce an error in the momentum equations. Interestingly, the error introduced in the MWI by the 'p-idw, MWI-1/2' formulation and the error introduced in the momentum equations by the 'p-1/2, MWI-1/2' formulation have identical magnitudes, see *fig.* 2.6. This implies that the formulation of the MWI presented in this section is consistently derived from the momentum equations.

Despite the seemingly significant theoretical differences between the considered pressure term formulations, see §2.3.2, the impact on the accuracy of the results is very modest. Although the propagation of acoustic waves is a very sensitive test case with respect to the applied numerical methods [66, 98], as even small inconsistencies or a lack of convergence lead to a visible change in the amplitude and speed of the waves, the propagation of the acoustic waves is predicted with high accuracy with all considered formulations. This suggests that the interpolation coefficients of the linear interpolation of the cell-centred pressure gradients in the MWI is not a primary factor for a robust pressure-velocity coupling on meshes with reasonably smooth changes of mesh resolution.

2.3.5.2 Lid-Driven Cavity

A lid-driven cavity, schematically shown in *fig.* 2.9, is simulated to demonstrate the impact of the different MWI formulations. The two-dimensional domain has dimensions $1\,\mathrm{m} \times 1\,\mathrm{m}$, with the top wall moving at a constant velocity of $u_\mathrm{w} = 1\,\mathrm{m\,s^{-1}}$. As indicated in *fig.* 2.9, a no-slip condition is applied at the top wall, while all other walls are assumed to be free-slip to accentuate the differences introduced by MWI. Three different meshes are considered, shown in *fig.* 2.10; an equidistant Cartesian mesh with 50×50 cells, a triangular mesh with 3916 cells, and a non-orthogonal quatrilateral mesh with 50×50 cells. The scaling factor of the non-orthogonal correction is $\zeta^f = 1$ for the presented simulations.

Figures 2.11a - 2.11c show the pressure contours computed on the three meshes for a Reynolds number of $\mathrm{Re} = \rho L u_\mathrm{w}/\mu = 1000$, where $L = 1\,\mathrm{m}$ is the size of the domain and μ is the

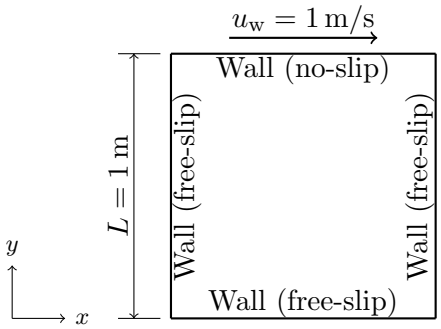

Figure 2.9: Schematic illustration of the two-dimensional lid-driven cavity and its boundary conditions, with the dimensions $1\,\mathrm{m} \times 1\,\mathrm{m}$ and the top wall moving at a constant velocity of $u_w = 1\,\mathrm{m\,s^{-1}}$.

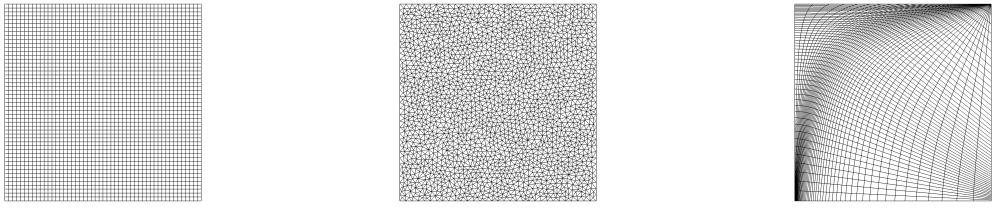

(a) Equidistant Cartesian mesh **(b)** Triangular mesh **(c)** Non-orthogonal quatrilateral mesh

Figure 2.10: The (a) equidistant Cartesian mesh with 50×50 cells, (b) triangular mesh with 3916 cells and (c) non-orthogonal quatrilateral mesh with 50×50 cells, used to simulate a lid-driven cavity with $\mathrm{Re} = 1000$.

dynamic viscosity, when the flow has reached a steady state. On all three meshes a stable and oscillation-free result is obtained. Furthermore, the profiles of both velocity components u and v, shown in *fig.* 2.12, are in very good agreement on all meshes, demonstrating the efficacy of the proposed formulation of the MWI on arbitrary meshes. The pressure along the y-centreline of the domain is shown in *fig.* 2.13a on Cartesian meshes with different resolution, indicating that the pressure profile converges with increasing mesh resolution. In fact, as observed in *fig.* 2.13b, the discretisation of the advecting velocity with MWI does not affect the second-order accuracy of the applied finite volume method, confirming the theoretical analysis in §2.3.2. When the simulation on the non-orthogonal mesh is restarted applying the advecting velocity ϑ^f as given by Eq. (2.52), *i.e.* without the projection of the pressure term in the MWI presented in Eq. (2.55) to correct for mesh non-orthogonality, yields significant pressure oscillations after only one time-step $\Delta t = 5 \times 10^{-3}$s, as observed in *fig.* 2.11d, and the solution algorithm diverges a few time-steps later. This shows clearly the substantial improvement of accuracy and stability provided by the non-orthogonal correction presented in Eq. (2.55), and demonstrates the consequences when the low-pass filter of the MWI is severely compromised.

The utility of the MWI to eliminate pressure-velocity decoupling becomes strikingly apparent when the lid-driven cavity is considered with a compressible fluid; with and without MWI. The previous simulations are modified such that the fluid has a heat capacity ratio of $\gamma = 1.4$ and a specific heat capacity at constant volume of $c_v = 720\,\mathrm{J\,kg^{-1}\,K^{-1}}$, which approximately corresponds to the properties of air at room temperature. The flow has an initial pressure of $p_0 = 10^5\,\mathrm{Pa}$ and an initial temperature of $T_0 = 347.22\,\mathrm{K}$, so that the density is $\rho_0 = 1\,\mathrm{kg\,m^{-3}}$. Hence, the speed of sound is $u_{\mathrm{s},0} = \sqrt{\gamma p_0/\rho_0} = 374.17\,\mathrm{m\,s^{-1}}$, which corresponds to a Mach number of $\mathrm{M} = u_{\mathrm{w}}/u_{\mathrm{s},0} = 2.67 \times 10^{-3}$. Figure 2.14a shows the pressure contours at steady state using the advecting velocity ϑ^f given in Eq. (2.56), on the equidistant Cartesian mesh with 50×50 cells. As expected, unphysical pressure oscillations as a result of pressure-velocity decoupling are absent and the pressure distribution is in excellent agreement with the incompressible result shown in *fig.* 2.11a. Restarting the compressible simulation with this result but omitting the MWI in the formulation of the advecting velocity, so that $\vartheta^f = \overline{u}_i^f \hat{n}_i^f$, clearly discernible pressure oscillations develop, as seen in *fig.* 2.14b. Note that the result shown in *fig.* 2.14b is an instantaneous snapshot and that the observed pressure oscillations grow over time until the solution algorithm diverges. These pressure oscillations are diminished when p_0 and T_0 are

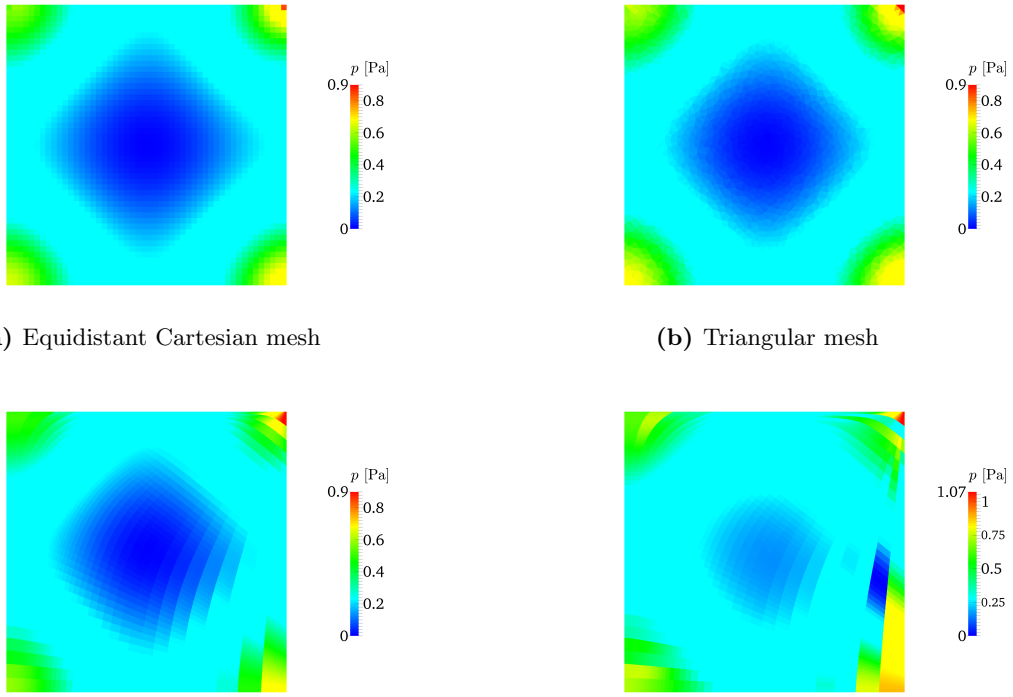

(a) Equidistant Cartesian mesh

(b) Triangular mesh

(c) Non-orthogonal quatrilateral mesh (with non-orthogonal correction)

(d) Non-orthogonal quatrilateral mesh (without non-orthogonal correction)

Figure 2.11: Contours of pressure p of the lid-driven cavity (Re = 1000), on (a) the equidistant Cartesian mesh, (b) the triangular mesh, (c) the non-orthogonal quatrilateral mesh with the MWI pressure term projected along $\hat{\boldsymbol{s}}^f$ (*i.e.* with non-orthogonal correction), and (d) the non-orthogonal quatrilateral mesh without non-orthogonal correction. The advecting velocity with non-orthogonal correction given in Eq. (2.56) is applied in (a)-(c), and the advecting velocity without non-orthogonal correction given in Eq. (2.52) is applied in (d).

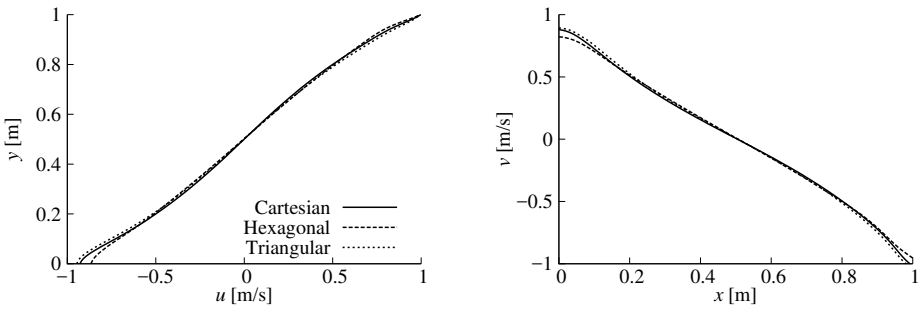

(a) u-velocity

(b) v-velocity

Figure 2.12: Profiles of (a) the u-velocity component and (b) the v-velocity component along the centreline of the lid-driven cavity domain for all three meshes at steady state. The advecting velocity given in Eq. (2.56) is applied.

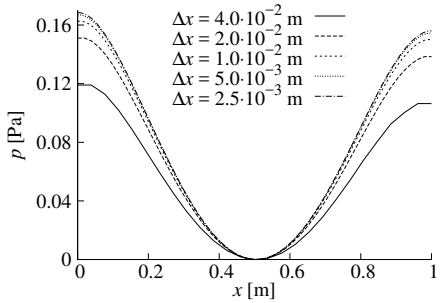

(a) Pressure profile along the y-centerline on Cartesian meshes with different mesh resolutions.

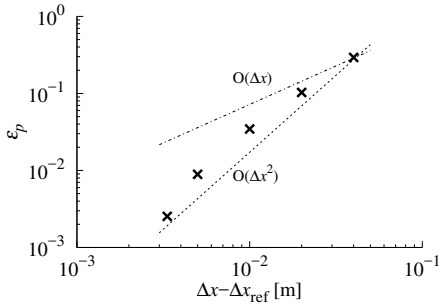

(b) Pressure error $\varepsilon_p = (p - p_{\text{ref}})/p_{\text{ref}}$ of the pressure taken at the left boundary on the y-centreline, as a function of mesh spacing $\Delta x - \Delta x_{\text{ref}}$, where subscript "ref" denotes the value on the reference mesh with $\Delta x_{\text{ref}} = 2.5 \times 10^{-3}\,\text{m}$.

Figure 2.13: Pressure along the centreline of the lid-driven cavity domain at steady state, on Cartesian meshes with mesh spacing $\Delta x = \{4 \times 10^{-2}, 2 \times 10^{-2}, 10^{-2}, 5 \times 10^{-3}, 3.\overline{3} \times 10^{-3}, 2.5 \times 10^{-3}\}\,\text{m}$.

modified to obtain a Mach number of M = 0.1 (but keeping $\rho_0 = 1\,\text{kg}\,\text{m}^{-3}$), as observed in *fig.* 2.15, because the pressure-density coupling described by the equation of state, Eq. (2.10), provides an indirect constraint on the pressure. These results demonstrate the necessity to account for pressure-velocity decoupling in low Mach number flows if a collocated variable arrangement is used with a pressure-based algorithm. In the fully compressible flow regime, for M $\geq$ 0.1, the pressure-density coupling is sufficiently strong to suppress pressure-velocity decoupling and diminish unphysical pressure oscillations.

2.4 Source Terms

The advecting velocity defined by Eq. (2.56) is applicable to steady-state and transient flows on arbitrary meshes and, as long as sources terms vary smoothly, this is sufficient for many applications. However, in the presence of source terms that are discontinuous or, more generally, have large gradients, previous studies [31, 64, 86] have shown that the effect of these source terms on the pressure field have to be accounted for in the MWI.

The reason for including these source terms in the MWI can be illustrated by assuming a quiescent flow, with an external force applied by means of a source term $\boldsymbol{S}$. The momentum

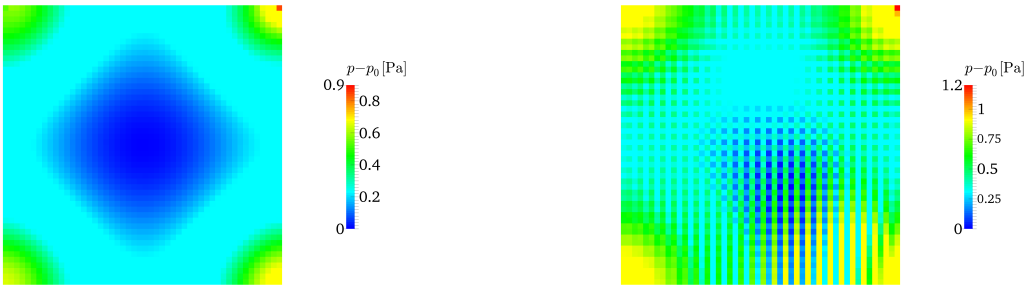

(a) With MWI **(b)** Without MWI

Figure 2.14: Contours of the pressure p of the lid-driven cavity (Re = 1000) on the equidistant Cartesian mesh. The flow is compressible with Mach number M = 2.67×10^{-3}. In (a) the pressure is shown at steady state obtained with the advecting velocity ϑ^f discretised with MWI given in Eq. (2.56), while in (b) the pressure is shown after restarting the simulation with the advecting velocity defined as $\vartheta^f = \overline{u}_i^f \hat{n}_i^f$ (*i.e.* without MWI).

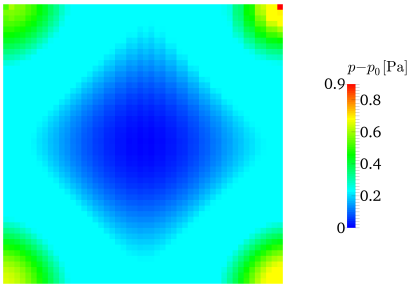

Figure 2.15: Contours of the pressure p of the lid-driven cavity (Re = 1000) at steady state, on the equidistant Cartesian mesh. The flow is compressible with Mach number M = 0.1. The advecting velocity is discretised without MWI as $\vartheta^f = \overline{u}_i^f \hat{n}_i^f$.

equations, Eq. (2.1), in semi-discretised form reduce for this case to

$$0 = -\left.\frac{\partial p}{\partial x_i}\right|^P + S_i^P \ . \tag{2.61}$$

The corresponding advecting velocity, Eq. (2.56), which is $\vartheta^f = 0$ since the flow is quiescent, becomes

$$\vartheta^f = \frac{\Delta p^f}{\Delta s^f} - \left.\overline{\frac{\partial p}{\partial x_i}}\right|^f \hat{s}_i^f = 0 \ , \tag{2.62}$$

with $\Delta p^f = p^F - p^P$. Inserting Eq. (2.61) into Eq. (2.62) follows as

$$\frac{\Delta p^f}{\Delta s^f} = \overline{S}_i^f \hat{s}_i^f \ , \tag{2.63}$$

a relationship previously used by Rahman *et al.* [75] for the inclusion of source terms in the MWI. However, Eq. (2.63) can only be satisfied if the source term results in a uniform or linearly varying pressure field. Hence, in order for the discretisation to be truly force-balanced, meaning that the discretisation of the pressure gradients and the source terms are equivalent, a source term $\boldsymbol{S}^\star$ has to be constructed that can match the discretised pressure gradient in all circumstances.

Equation (2.61) suggests that source terms cause a pressure gradient, an observation also exploited in previous studies [31, 64, 86, 101], in addition to the pressure gradient associated with the underlying flow $\widetilde{\boldsymbol{\nabla} p}$, henceforth called the *driving pressure gradient*, with the pressure gradient being

$$\left.\frac{\partial p}{\partial x_i}\right|^P = \left.\widetilde{\frac{\partial p}{\partial x_i}}\right|^P + S_i^{P,\star} \ . \tag{2.64}$$

It is the pressure gradient associated with the velocity field, *i.e.* the driving pressure gradient, that is relevant for the pressure-velocity coupling, while all other contributions to the pressure gradient, *i.e.* source terms, should be excluded. The advecting velocity including source terms should, hence, be

$$\vartheta^f = \overline{u}_i^f \hat{n}_i^f - \zeta^f \hat{d}^f \left(\left.\widetilde{\frac{\partial p}{\partial x_i}}\right|^f - \left.\overline{\widetilde{\frac{\partial p}{\partial x_i}}}\right|^f \right) \hat{s}_i^f + c^f \hat{d}^f \left(\vartheta^{f,O} - \overline{u}_i^{f,O} \hat{n}_i^f \right) \ . \tag{2.65}$$

Therefore, the discretisation of the source terms has to precisely match the discretisation of the

pressure gradients to avoid spurious corrections of the MWI that manifest as unphysical fluid accelerations.

2.4.1 Discretisation of Source Terms

The analysis of the pressure term in §2.3.2 shows that, to preserve the low-pass filter on the pressure field, the cell-centred pressure gradient has to be evaluated using the divergence theorem, given by Eq. (2.32). This can be reformulated in terms of Δp^f as

$$\left.\frac{\partial p}{\partial x_i}\right|^f \approx \frac{1}{V^P}\sum_f w_i^f \Delta p^f = \frac{1}{V^P}\sum_f \left[l^f p^P + (1-l^f)p^F\right]\hat{n}_i^f A^f - \frac{p^P}{V^P}\underbrace{\sum_f \hat{n}_i^f A^f}_{=0} \ , \tag{2.66}$$

with $\boldsymbol{w}^f = (1-l^f)\hat{\boldsymbol{n}}^f A^f$. Using a finite volume method, the last term on the right-hand side of Eq. (2.66) is by definition zero and, thus, Eq. (2.66) is equivalent to Eq. (2.32). If the interpolation of the pressure at face f is amended by additional correction terms, such as the gradient-based skewness correction in Eq. (2.24), the general formulation for the pressure gradient reads

$$\left.\frac{\partial p}{\partial x_i}\right|^f \approx \frac{1}{V^P}\sum_f \left(w_i^f \Delta p^f + k_i^f\right) \ , \tag{2.67}$$

where $\boldsymbol{k}^f$ is the correction coefficient of the interpolation, *e.g.* $k_i^f = \boldsymbol{r}^f \cdot \overline{\boldsymbol{\nabla} p}^f \hat{n}_i^f A^f$ for mesh skewness. The discretisation of the source terms should follow the same template as the discretisation of the pressure gradients, with the cell-centred source terms discretised as

$$S_i^{P,\star} = \frac{1}{V^P}\sum_f \left(w_i^f \Delta S^f + k_i^f\right) = \frac{1}{V^P}\sum_f \left(w_i^f \overline{S}_j^f \hat{s}_j^f \Delta s^f + k_i^f\right) \ , \tag{2.68}$$

with

$$\frac{\Delta S^f}{\Delta s^f} = \overline{S}_j^f \hat{s}_j^f \ , \tag{2.69}$$

similar to the definition of the pressure gradient at face centres given in Eq. (2.53).

The discretisation of the source term given in Eq. (2.68) is consistent with the discretisation of the pressure gradients and, therefore, ensures a force-balanced discretisation. However, this discretisation may modify the actual force applied to the fluid by the discretised source term. The interpolation of the source term at face f from the cell-centred values at P and F has to

assure that the discretised source terms apply the correct force to the flow. Returning to the simplified one-dimensional, quiescent flow and assuming, for now, that Eq. (2.61) is satisfied by the discretised source terms and pressure gradients, the pressure difference $\Delta p^f = p^F - p^P$ is given by

$$\Delta p^f = \Delta q^{Pf} S^P + \Delta q^{Ff} S^F \ , \tag{2.70}$$

with Δq^{Pf} and Δq^{Ff} the distance between cell centre P and face f and between cell centre F and face f, respectively. Since the force applied to the flow by the source term is integrated over the distance (or area/volume in two/three dimensions), the contribution of the source term to the pressure gradient increases with the distance between cell centre and face centre. Consequently, the force applied by the discretised source terms is preserved with distance weighting, given as

$$\overline{\boldsymbol{S}}^f = l^{f,(\mathrm{dw})} \boldsymbol{S}^P + \left(1 - l^{f,(\mathrm{dw})}\right) \boldsymbol{S}^F \ , \tag{2.71}$$

where

$$l^{f,(\mathrm{dw})} = \frac{\Delta q^{Pf}}{\Delta q^{Pf} + \Delta q^{Ff}} \ , \tag{2.72}$$

contrary to the *inverse* distance weighting in Eq. (2.23).

Adding the discretised source terms as defined above to Eq. (2.56), the advecting velocity is defined as

$$\vartheta^f = \overline{u}_i^f \hat{n}_i^f - \zeta^f \hat{d}^f \left[\frac{\Delta p^f}{\Delta s^f} - \overline{S}_i^f \hat{s}_i^f - \left(\overline{\left.\frac{\partial p}{\partial x_i}\right|}^f - \overline{S}_i^{f,\star} \right) \hat{s}_i^f \right] + c^f \hat{d}^f \left(\vartheta^{f,O} - \overline{u}_i^{f,O} \hat{n}_i^f \right) , \tag{2.73}$$

with $\overline{\boldsymbol{S}}^f$ obtained by Eq. (2.71), while the interpolation of $\overline{\boldsymbol{\nabla} p}^f$ and $\overline{\boldsymbol{S}}^{f,\star}$ has to be conducted in the same way, following the explanation given in §2.3.2 for pressure. In to order preserve the low-pass pressure filter of the MWI, the source terms are projected along vector $\hat{\boldsymbol{s}}^f$ in the same way as the pressure term described in §2.3.4. For Eq. (2.73) to be equivalent to Eq. (2.65), and for the discretisation to be force-balanced, the discretised source term $\boldsymbol{S}^{P,\star}$ also has to be applied in the discretised momentum equations, see Eq. (2.4), so that the momentum equations for the quiescent flow discussed above, 2.61, become

$$0 = - \left. \frac{\partial p}{\partial x_i} \right|^P + S_i^{P,\star} \ . \tag{2.74}$$

2.4.2 Numerical Experiments

The proposed discretisation of the source terms and the robust pressure-velocity coupling provided by the MWI in flows with source terms is tested for discontinuous source terms in one-dimensional flows on equidistant and non-equidistant meshes, as well as in a two-dimensional flow on a hybrid quatrilateral/triangular mesh.

A one-dimensional, incompressible flow is simulated, for which the continuity equation enforces a constant velocity in the entire domain. The domain has a length of $L = 1\,\mathrm{m}$ and is represented by an equidistant mesh. Two cases are considered: one with a stepped source term, given by

$$S(x) = \begin{cases} 1, & \text{for } 0.25\,\mathrm{m} \leq x \leq 0.75\,\mathrm{m} \\ 0, & \text{otherwise,} \end{cases} \tag{2.75}$$

and one with a ramped source term, given by

$$S(x) = \begin{cases} 0, & \text{for } x < 0.25\,\mathrm{m} \\ \dfrac{x - 0.25}{0.5}, & \text{for } 0.25\,\mathrm{m} \leq x \leq 0.75\,\mathrm{m} \\ 1, & \text{otherwise.} \end{cases} \tag{2.76}$$

In both cases, the exact solution satisfies

$$\frac{\partial p}{\partial x}(x) = S(x), \ \frac{\partial u}{\partial x} = 0, \tag{2.77}$$

and the error of the computed solution is

$$\varepsilon_u(x) = \frac{u(x) - u_{\mathrm{in}}}{u_{\mathrm{in}}} \ , \tag{2.78}$$

where u_{in} is the velocity at the domain-inlet. The velocity errors $\varepsilon_u(x)$ for both cases after one time-step are shown in *fig.* 2.16 using different source term treatments; MWI without source terms (abbreviated "MWI"), MWI with source terms S included as-is (similar to [75], abbreviated "MWI-S"), and MWI with source terms $S^\star$ that are discretised as proposed in §2.4.1 (abbreviated "MWI-S*"). Both cases demonstrate that a discrepancy between the discretisation of the pressure gradient and the discretisation of the source term causes an artificial acceleration

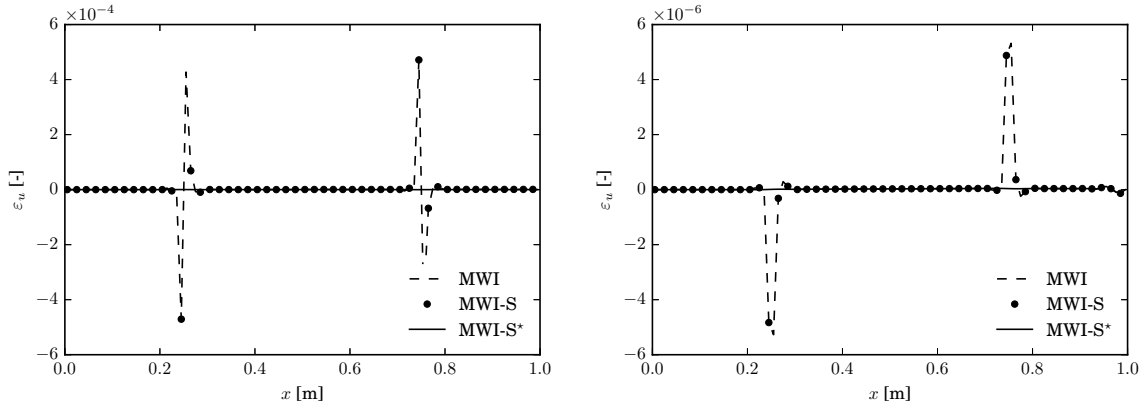

(a) Stepped source term

(b) Ramped source term

Figure 2.16: Velocity errors obtained after one time-step for (a) the stepped source term and (b) the ramped source term in a one-dimensional flow with different source term treatments: MWI without source terms (abbreviated "MWI"), MWI with source terms included as-is (abbreviated "MWI-S"), and MWI with source terms that are discretised as proposed in §2.4.1 (abbreviated "MWI-S⋆").

that leads to an incorrect velocity. Using the source term discretisation proposed in Eq. (2.68), the fluid does not accelerate, matching the exact solution. Away from the discontinuities, all three approaches agree with the exact solution. The ramped case demonstrates that a linear change in pressure gradient, here generated by a linear variation in source term, does not affect the pressure-velocity coupling and low-pass filter of the MWI, as discussed in §2.3.3, while velocity errors ensue at the points where the source term varies non-linearly ($x = 0.25\,\mathrm{m}$ and $x = 0.75\,\mathrm{m}$), if the source term is not discretised consistently.

To test the effect of a non-equidistant mesh and demonstrate the efficacy of the proposed interpolation of the source terms using distance weighting, proposed in Eq. (2.71), a source term is applied at the central cell P of a one-dimensional domain. The applied non-equidistant mesh has an increasing mesh spacing towards the centre of the domain, schematically shown in *fig.* 2.17. As in the previous case, continuity dictates a constant velocity in the domain, while the source term leads to a change in pressure, with the pressure difference being

$$\Delta p = p^E - p^W = S^P \Delta x^P \ . \tag{2.79}$$

As the source term is only applied in cell P, the discretised pressure of the exact solution varies

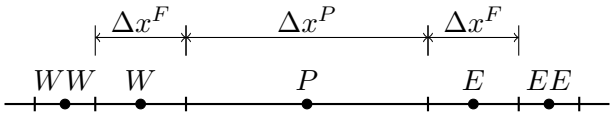

Figure 2.17: Schematic illustration of the one-dimensional domain with a non-equidistant mesh that has an increasing mesh spacing towards the centre of the domain. Cell P with mesh spacing Δx^P is at the centre of the domain, with its neighbour cells W and E that both have mesh spacing Δx^F.

linearly in cell P, but is constant in its neighbour cells, with $\nabla p^W = \nabla p^E = 0$. Figure 2.18a shows the pressure field computed with distance weighted interpolation and inverse distance weighted interpolation applied to the source term, alongside the exact solution. In both cases the source terms are discretised consistently with the pressure gradients, as proposed in Eq. (2.68). Consequently, errors in the velocity field are negligible in both cases. However, the applied interpolation has a significant effect on the computed pressure field, as observed in *fig.* 2.18a. The pressure difference is predicted accurately when the source terms are interpolated using distance weighting, as proposed in Eq. (2.71), while the pressure difference is underpredicted when inverse distance weighting is applied. Varying the cell-size ratio between cell P and its neighbours W and E, the pressure difference remains in excellent agreement with the exact result when the proposed distance weighted interpolation is applied, as observed in *fig.* 2.18b. Applying inverse distance weighting for the interpolation, however, the error in pressure difference compared to the exact result, shown in *fig.* 2.18b, increases linearly with the ratio $\Delta x^P / \Delta x^F$.

The most attractive aspect of the collocated variable arrangement, and hence MWI, is the ease with which arbitrary meshes can be handled. This means the discretisation of source terms proposed in §2.4.1 must also be applicable on arbitrary meshes. A two-dimensional mesh with dimensions $1\,\mathrm{m} \times 0.2\,\mathrm{m}$ consisting of (Cartesian) quatrilateral cells and an embedded region of triangular cells, extending in the range $0.25\,\mathrm{m} \leq x \leq 0.75\,\mathrm{m}$ and $0.05\,\mathrm{m} \leq y \leq 0.15\,\mathrm{m}$, shown in *fig.* 2.19, is used to test the source term discretisation on arbitrary meshes. The triangular cells combine the effects of changes in cell size, skewness and non-orthogonality. Using the stepped source term described by Eq. (2.75), the source term covers the same x-range as the triangular section of the mesh and extends over the complete height of the domain. The flow is introduced with a uniform velocity at the domain-inlet, with free-slip boundary conditions applied to the top and bottom walls. As the source term is constant over the height of the domain, the velocity

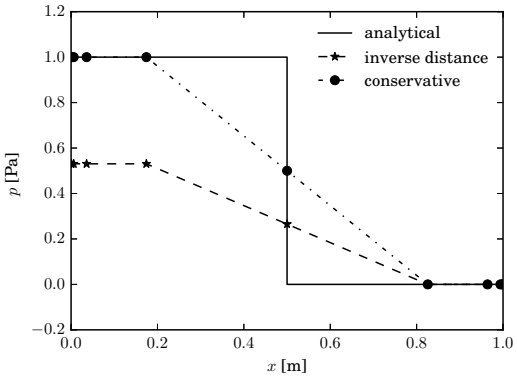

(a) Pressure distribution for a cell-size ratio of $\Delta x^F/\Delta x^P = 0.53$. The markers correspond to the actual cell centres of the simulations.

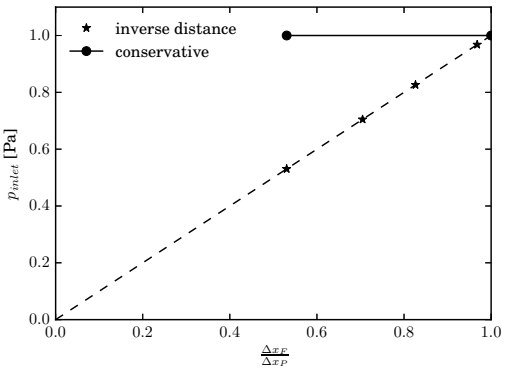

(b) Computed pressure at the domain-inlet as a function of cell-size ratio $\Delta x^F/\Delta x^P$.

Figure 2.18: Pressure distribution and pressure at the domain-inlet of the one-dimensional flow with point source at the centre of the domain on a mesh with increasing mesh spacing towards the centre of the domain.

is expected to remain one-dimensional and uniform. The velocity error ε_u along the centreline is shown in *fig.* 2.20. As for the previously discussed test cases, the proposed discretisation and distance weighted interpolation does not yield any noticeable errors. Not including the source terms or including the source terms without taking special care of the discretisation, leads to significant errors in the velocity field.

2.5 Density Discontinuities

In addition to varying or discontinuous source terms, a feature of many multiphase flows are discontinuous density fields, which results in discontinuous pressure gradients and leads, in turn, to oscillatory solutions or failure to reach a solution [31]. Rearranging the momentum equations, Eq. (2.1), as an expression for the pressure gradient,

$$\frac{\partial p}{\partial x_j} = -\rho \left(\frac{\partial u_j}{\partial t} + u_i \frac{\partial u_j}{\partial x_i} \right) + \frac{\partial \tau_{ij}}{\partial x_i} + S_j \ , \tag{2.80}$$

shows that the pressure gradient is proportional to the density. Due to the use of linear interpolation in the discretisation of the pressure field, this discontinuity cannot be represented by the discrete representation of the pressure gradient, leading to discrepancies between the discretised momentum equations and the equation for the advecting velocity at the face.

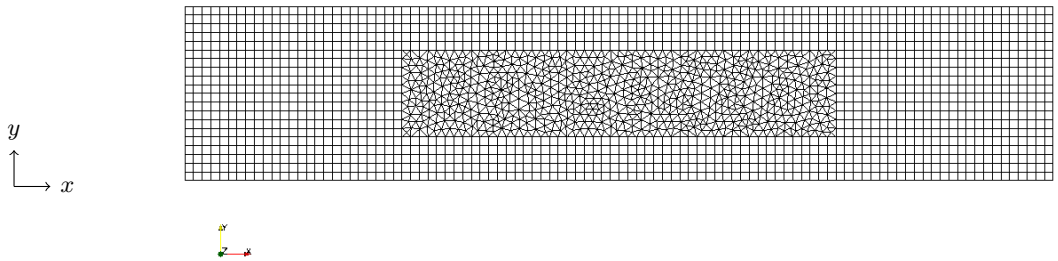

Figure 2.19: Hybrid quatrilateral/triangular two-dimensional mesh with dimensions $1\,\mathrm{m} \times 0.2\,\mathrm{m}$, used to test the discretisation of source terms. The triangular region extends in the range $0.25\,\mathrm{m} \leq x \leq 0.75\,\mathrm{m}$ and $0.05\,\mathrm{m} \leq y \leq 0.15\,\mathrm{m}$.

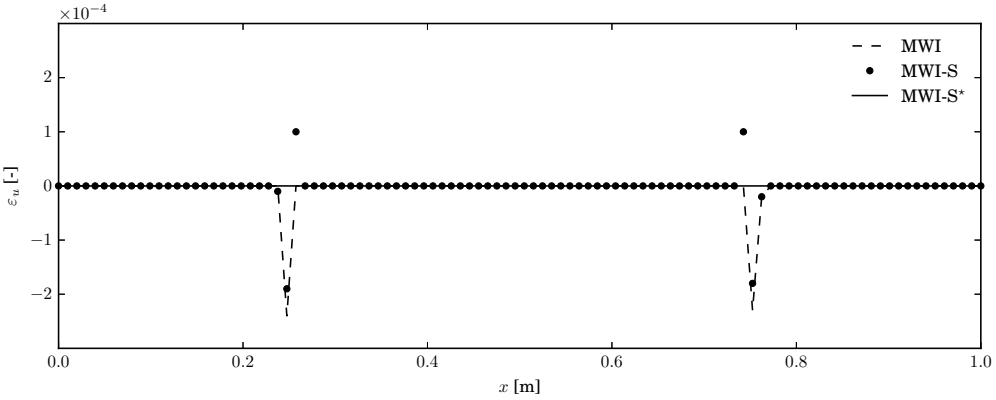

Figure 2.20: Velocity errors obtained after one time-step for the stepped source term in a two-dimensional flow, plotted along the centreline of the domain with different source term treatments: MWI without source terms (abbreviated "MWI"), MWI with source terms included as-is (abbreviated "MWI-S"), and MWI with source terms that are discretised as proposed in §2.4.1 (abbreviated "MWI-S⋆").

To illustrate the problem that arises, a one-dimensional, inviscid, incompressible two-phase flow, with the two bulk phases separated by a sharp interface, subject to a constant acceleration in the absence of source terms is considered. Because both fluids are incompressible, the velocity field should be spatially uniform. Hence, the discretised momentum equations reduce in this case to

$$\left.\frac{\partial p}{\partial x_i}\right|^P = -\rho^P \left.\frac{\partial u_i}{\partial t}\right|^P = -\rho^P a_i \ , \tag{2.81}$$

where $\boldsymbol{a}$ is the spatially uniform acceleration of the flow. Similar to Eq. (2.80), the discretised momentum equations, Eq. (2.81), shows that the pressure gradient is proportional to the cell-averaged density and is, therefore, discontinuous where the density is discontinuous. In the limit of large density ratios, the pressure gradient in the heavier fluid is significantly larger than in the lighter fluid, *i.e.*

$$\max\left\{\frac{\partial p}{\partial x_j}\right\} \gg \min\left\{\frac{\partial p}{\partial x_j}\right\} \ , \tag{2.82}$$

and the pressure term in the MWI of the advecting velocity, Eq. (2.56), is

$$\lim_{\rho_{\max}/\rho_{\min}\to\infty} \left.\frac{\partial p}{\partial x_i}\right|^f = \max\left\{ l^f \left.\frac{\partial p}{\partial x_i}\right|^P , \ (1-l^f) \left.\frac{\partial p}{\partial x_i}\right|^F \right\} \ , \tag{2.83}$$

where l^f is the interpolation coefficient. As a result, the discrete pressure gradient is underpredicted in the heavier phase and overpredicted in the lighter phase, which leads to an artificial acceleration of the flow in the vicinity of the interface. In the case of extremely large density ratios, the large and unphysical force applied to the lighter phase may lead to divergence of the solution algorithm [31].

2.5.1 Density Weighting in the MWI

Denner and van Wachem [31] proposed to weight the pressure gradients in the MWI by the corresponding density, with the pressure term in the MWI of the advecting velocity, Eq. (2.56), becoming

$$\frac{1}{\rho^f}\left.\frac{\partial p}{\partial x_i}\right|^f - \frac{1}{2}\left(\frac{1}{\rho^P}\left.\frac{\partial p}{\partial x_i}\right|^P + \frac{1}{\rho^F}\left.\frac{\partial p}{\partial x_i}\right|^F\right) = \left.\frac{\partial p}{\partial x_i}\right|^f - \frac{\rho^f}{2}\left(\frac{1}{\rho^P}\left.\frac{\partial p}{\partial x_i}\right|^P + \frac{1}{\rho^F}\left.\frac{\partial p}{\partial x_i}\right|^F\right) \approx 0 \ , \tag{2.84}$$

where the cell-centred pressure gradients are interpolated with 1/2-weighting and with the face

density evaluated by harmonic averaging $\rho^f = 2/(\rho^{P^{-1}} + \rho^{F^{-1}})$. The generalisation of this density weighting is straightforward, with the pressure term of the MWI given as

$$\left.\frac{\partial p}{\partial x_i}\right|^f - \rho^f \left(\left.\frac{l^f}{\rho^P}\frac{\partial p}{\partial x_i}\right|^P + \left.\frac{1-l^f}{\rho^F}\frac{\partial p}{\partial x_i}\right|^F \right) , \tag{2.85}$$

where l^f is the interpolation coefficient, and the face density defined by

$$\frac{1}{\rho^f} = \frac{l^f}{\rho^P} + \frac{1-l^f}{\rho^F} . \tag{2.86}$$

Note that the interpolation coefficients of the cell-centred pressure gradients add up to unity,

$$\rho^f \left(\frac{l^f}{\rho^P} + \frac{1-l^f}{\rho^F} \right) = 1 , \tag{2.87}$$

which is crucial for a consistent and bounded interpolation. In the limit of large density ratios, for instance with $\rho^F/\rho^P \to \infty$, the face density becomes

$$\lim_{\rho^F/\rho^P \to \infty} \rho^f = \frac{\rho^P}{l^f} \tag{2.88}$$

and the pressure term in Eq. (2.85) follows as

$$\left.\frac{\partial p}{\partial x_i}\right|^f - \frac{\rho^P}{l^f} \left(\left.\frac{l^f}{\rho^P}\frac{\partial p}{\partial x_i}\right|^P + \left.\frac{1-l^f}{\rho^F}\frac{\partial p}{\partial x_i}\right|^F \right) = \left.\frac{\partial p}{\partial x_i}\right|^f - \left.\frac{\partial p}{\partial x_i}\right|^P . \tag{2.89}$$

Thus, the cell-to-cell change in pressure tends to the value corresponding to the minimum pressure gradient on either side of the density discontinuity. This has a stabilising effect in the discretisation, because instead of applying a force that is too large in the lighter fluid, leading to large accelerations, a force that is too small is applied to the heavier fluid. Consequently, the errors associated with a discontinuous change in density are substantially reduced and the numerical solution remains stable.

2.5.2 Application to Two-Phase Flows

An accelerating incompressible two-phase flow in a one-dimensional domain is simulated, in which the bulk phases with different densities are separated by a sharp interface. The flow is initially

quiescent and the lighter fluid occupies the entire domain. The heavier fluid is introduced at the inlet with velocity

$$u_{\text{in}}(t) = a\,t \ , \tag{2.90}$$

where a is a constant acceleration and t is time, and the discretised momentum equation is given by Eq. (2.81). In theory, the solution is a spatially uniform, time-varying velocity given by Eq. (2.90), with a discontinuity in the pressure gradient field at the interface due to the discontinuity in density. The two-phase flow is simulated using the Volume-of-Fluid (VOF) method [45], where the local volume fraction of each bulk phase is represented by the colour function γ, with $\gamma = 0$ for the light phase and $\gamma = 1$ for the heavy phase. The interface is present in cells with $0 < \gamma < 1$. A compressive VOF method [32] is used to advect the interface with the underlying flow. The local density is defined based on the local colour function value as $\rho(x) = \gamma(x)\rho_{\text{H}} + [1 - \gamma(x)]\rho_{\text{L}}$, where ρ_{H} and ρ_{L} are the density of the heavy fluid and the light fluid, respectively. The numerically computed pressure gradients are compared with the exact solution

$$\left.\frac{\partial p}{\partial x}(x)\right|_{\text{exact}} = -a\rho(x) \ , \tag{2.91}$$

where the value of $\rho(x)$ is determined by the interface location $x_\Sigma(t) = at^2/2$ as

$$\rho(x) = \begin{cases} \rho_{\text{H}} & \text{if } x < x_\Sigma \\ \rho_{\text{L}} & \text{if } x > x_\Sigma \end{cases} . \tag{2.92}$$

Figure 2.21a shows the pressure gradients of the numerical solution obtained with and without density weighting for a two-phase flow with a density ratio of $\rho_{\text{H}}/\rho_{\text{L}} = 50$. Both cases exhibit errors in the computed pressure gradient. The exact solution is two constant gradients with a discontinuity at the interface, whereas over- and undershoots are evident in the numerical results. However, with the density weighting in the MWI the maximum magnitude of the error is $< 10\%$ compared to the exact value, whereas the maximum magnitude of the error increases to more than 50% without the density weighting in the MWI. The ensuing errors in the velocity field, shown in *fig.* 2.21b, confirm that the errors are diminished when the density weighting is applied in the MWI. Figure 2.22 shows the same case, but for two fluids with density ratios $\rho_{\text{H}}/\rho_{\text{L}} = 10^3$ and $\rho_{\text{H}}/\rho_{\text{L}} = 10^6$. Only results obtained with the density-weighted MWI are shown

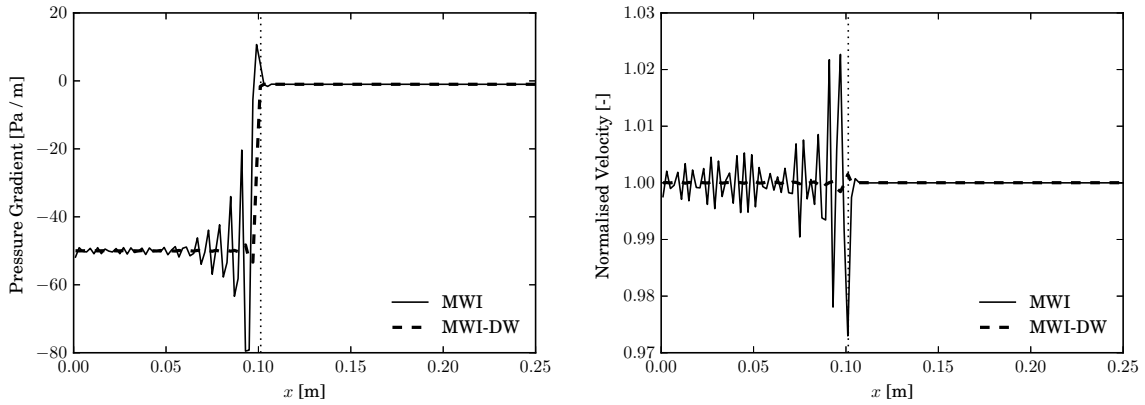

(a) Pressure gradient

(b) Normalised velocity

Figure 2.21: Pressure gradient and normalised velocity of the one-dimensional two-phase flow with density ratio $\rho_{\mathrm{H}}/\rho_{\mathrm{L}} = 50$, without density weighting in the MWI (abbreviated "MWI") and with density weighting in the MWI (abbreviated "MWI-DW"). The location of the interface is indicated by a dotted line.

in *fig.* 2.22, because a converged numerical solution without density weighting is not available for these cases. Despite the large density ratios, the pressure gradients are predicted accurately when the density weighting is applied in the MWI, with only small errors.

The presented results, notably a comparison of Figs. 2.22a and 2.22b, suggest that the magnitude of the error associated with the pressure gradient increases with increasing density ratio. In fact, as seen in *fig.* 2.23, the error magnitude of the computed pressure gradient increases linearly with density ratio. Hence, the relative error in pressure introduced by the density-weighted MWI is independent of the density ratio. Furthermore, the presented results suggest that the error of the computed pressure gradient is largely contained in the heavier phase, which is desirable as it reduces spurious accelerations of the flow, and, hence, in conjunction with the linear relationship between density ratio and associated errors, indicates that the density-weighted MWI assures a stable result for a wide range of density ratios. To this end, Denner and van Wachem [33] reported stable results for a two-phase flow with a density ratio of $\rho_{\mathrm{H}}/\rho_{\mathrm{L}} = 10^{24}$, without any noticeable errors, far exceeding density ratios of typical multiphase flows.

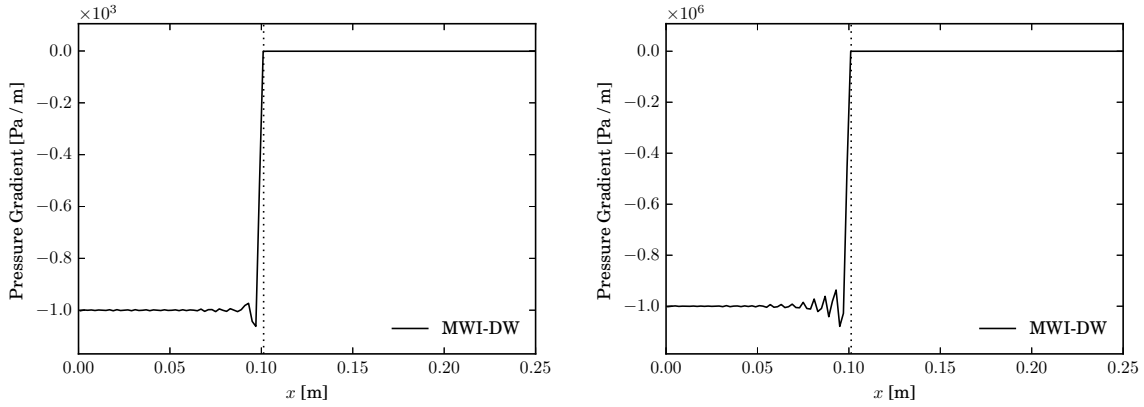

(a) $\rho_{\mathrm{H}}/\rho_{\mathrm{L}} = 10^3$ **(b)** $\rho_{\mathrm{H}}/\rho_{\mathrm{L}} = 10^6$

Figure 2.22: Pressure gradient of the one-dimensional two-phase flow with density ratios $\rho_{\mathrm{H}}/\rho_{\mathrm{L}} = 10^3$ and $\rho_{\mathrm{H}}/\rho_{\mathrm{L}} = 10^6$, with density weighting in the MWI. The location of the interface is indicated by a dotted line.

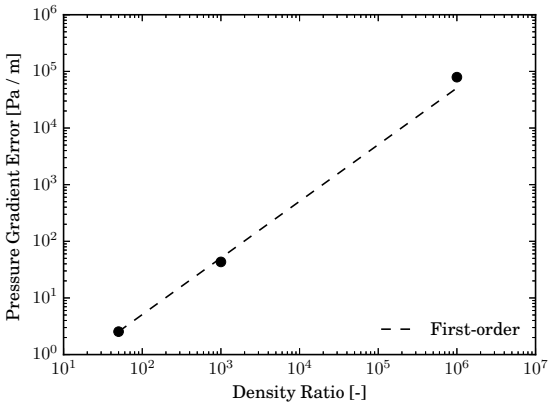

Figure 2.23: Maximum magnitude of the pressure gradient errors for the one-dimensional two-phase flow as a function of the density ratio $\rho_{\mathrm{H}}/\rho_{\mathrm{L}}$, obtained with density weighting in the MWI.

2.6 Unified Formulation of the Momentum-Weighted Interpolation

The detailed derivation and analysis of the MWI in §2.3, as well as its extensions to include source terms in §2.4 and account for large density ratios in §2.5, shows that a consistent formulation of the MWI has many subtleties. Even small inconsistencies in the formulation or discretisation of the MWI, such as the interpolation of the cell-centred pressure gradients discussed in §2.3.2, can have a noticeable effect on the quality of the numerical results. The discretisation of the driving pressure term is shown to be at the heart of the MWI, as it provides the crucial cell-to-cell coupling of the pressure and constitutes a low-pass filter with respect to the third and higher derivatives of the driving pressure. The results presented in §2.3.5 and §2.4.2 demonstrate that preserving this low-pass filter on the driving pressure field is critical for a robust pressure-velocity coupling and accurate numerical results; the cell-to-cell pressure coupling provided by the MWI is not by itself sufficient to prevent pressure-velocity decoupling, as observed in §2.3.5.2. Following the presented step-by-step analysis, a unified formulation of the advecting velocity defined in Eq. (2.73) using MWI is proposed to be constructed as follows:

- The type of interpolation applied for $\overline{u}_i^f$ and $\overline{u}_i^{f,O}$ is not important for the efficacy of the MWI, as discussed in §2.3.1, but of course influences the accuracy of the computed advecting velocity. Thus, $\overline{u}_i^f$ and $\overline{u}_i^{f,O}$ are computed by Eq. (2.24). This is consistent with previous studies [13, 14, 31, 98, 101].

- The interpolation of the cell-centred pressure gradients $\overline{\boldsymbol{\nabla} p}^f$ and of the cell-centred source terms $\overline{\boldsymbol{S}}^{f,\star}$ is conducted with inverse distance weighting, which is required to accurately satisfy the filter properties of the MWI, as shown by the theoretical analysis in §2.3.2 and the numerical results presented in §2.3.5.1.

- The source terms at faces $\overline{\boldsymbol{S}}^f$ are interpolated with distance weighting, proposed in Eq. (2.71), to preserve the applied force on the flow, as discussed in §2.4.1.

- The source terms at cell centres $\boldsymbol{S}^\star$ are computed as proposed in Eq. (2.68), a discretisation that matches the discretisation of the pressure gradients on the discrete level, as demonstrated in §2.4.2, and, hence, together with the distance-weighted interpolation of $\overline{\boldsymbol{S}}^f$ proposed in Eq. (2.71), provides a force-balanced discretisation.

- The coefficients c^f and d^f, with $\hat{d}^f = d^f/(1+c^f d^f)$, are evaluated at faces only, to retain the filter properties of the MWI. It is important to understand that these coefficients are merely weighting factors for terms that should be small in the converged solution; they ought to have a meaningful order of magnitude, but their precise value is secondary. The appropriateness of the definitions for c^f and d^f given in §2.3.3, in particular Eq. (2.42), Eq. (2.43) and Eq. (2.49), is demonstrated by the results in §2.3.5.1 and §2.4.2.

- In order to account for mesh non-orthogonality, an issue discussed in §2.3.4, the pressure term and the source terms are projected along the unit vector $\hat{\boldsymbol{s}}^f$, which connects the adjacent cell centres, by an orthogonal/non-orthogonal decomposition. Results presented in §2.3.5.2 demonstrate that this is essential for the integrity of the filter properties of the MWI and to avoid pressure-velocity decoupling on meshes with large non-orthogonality. The scaling factor of the decomposition is proposed to be $\zeta^f = 1$, which corresponds to an orthogonal decomposition [27], so that the decomposition does not affect the weighting of the pressure and source terms (*i.e.* the filter on the third derivative of the driving pressure $\widetilde{p}$).

- The pressure term and the source terms are density weighted as proposed in Eq. (2.85) and Eq. (2.86), to minimise the errors associated with large discontinuous changes in density and stabilise the solution, discussed in §2.5.1.

To summarise, applying these discretisation rules and recommendations to Eq. (2.73), the advecting velocity follows as

$$
\begin{aligned}
\vartheta^f = & \left[l^{f,(\mathrm{idw})} u_i^P + \left(1 - l^{f,(\mathrm{idw})}\right) u_i^F + \left.\overline{\frac{\partial u_i}{\partial x_j}}\right|^f r_j^f \right] \hat{n}_i^f \\
& - \hat{d}^f \left\{ \frac{p^F - p^P}{\Delta s^f} - \rho^f \left[\left. \frac{l^{f,(\mathrm{idw})}}{\rho^P} \frac{\partial p}{\partial x_i} \right|^P + \frac{1 - l^{f,(\mathrm{idw})}}{\rho^F} \left. \frac{\partial p}{\partial x_i} \right|^F \right] \hat{s}_i^f \right\} \\
& + \hat{d}^f \left\{ \left[l^{f,(\mathrm{dw})} S_i^P + \left(1 - l^{f,(\mathrm{dw})}\right) S_i^F \right] \hat{s}_i^f - \rho^f \left[\frac{l^{f,(\mathrm{idw})}}{\rho^P} S_i^{P,\star} + \frac{1 - l^{f,(\mathrm{idw})}}{\rho^F} S_i^{F,\star} \right] \hat{s}_i^f \right\} \\
& + c^f \hat{d}^f \left\{ \vartheta^{f,O} - \left[l^{f,(\mathrm{idw})} u_i^{P,O} + \left(1 - l^{f,(\mathrm{idw})}\right) u_i^{F,O} + \left.\overline{\frac{\partial u_i}{\partial x_j}}\right|^{f,O} r_j^f \right] \hat{n}_i^f \right\} \ .
\end{aligned}
\tag{2.93}
$$

This formulation provides a robust pressure-velocity coupling and a low-pass filter on third and higher derivatives of the driving pressure on arbitrary meshes, it is time-step independent and

satisfies the steady-state solutions of steady-state ($\Delta t \to \infty$) as well as initially transient (Δt is finite) problems. Furthermore, this formulation provides stable results for any density ratio and it reduces to the normal velocity at cell faces, $\vartheta^f = \overline{\boldsymbol{u}}^f \cdot \hat{\boldsymbol{n}}^f$, for steady-state solutions with constant or linearly changing driving pressure.

2.7 Conclusions

When simulating flows in and around complex geometries, the discretisation of the governing equations is greatly simplified by using a collocated variable arrangement. In simulations of incompressible and low Mach number flows this gives rise to pressure-velocity decoupling, with the characteristic chequerboard pressure field, if a straightforward discretisation is employed [71]. The MWI, typically attributed to have been introduced by Rhie and Chow [76], is a widely used method to couple pressure and velocity in collocated variable arrangements and as a remedy for pressure-velocity decoupling. However, in the current literature there are many varieties of MWI, and it is so far unclear what the optimal formulation is.

In this chapter, a unified formulation of the MWI for arbitrary meshes has been derived based on physically consistent arguments, including extensions for discontinuous source terms and discontinuous changes in density. The presented step-by-step derivation and analysis of the MWI has been used to develop theoretical justifications for the discretisation of velocity, pressure and source terms, including the applied interpolation and weighting coefficients, under the main assumption that MWI enforces a low-pass filter acting on the discrete pressure field, thereby imposing a direct relationship between neighbouring pressure values that suppresses oscillatory solutions. This theoretical analysis has been further supported with numerical results of representative test cases on arbitrary (structured and unstructured) meshes, demonstrating the impact of the MWI in general as well as the impact of the low-pass filter enforced by the MWI. With regards to discontinuous or strongly varying source terms, only the driving pressure gradient, *i.e.* the pressure gradient associated with the flow, should be coupled to the velocity field. Failing to account for source terms in the MWI can lead to decoupled solutions and artificial accelerations of the fluid in cases which include sharp gradients and discontinuities of source terms, as demonstrated in the presented results. The proposed reconstruction of the discrete source term provides an exact balance with the discretised pressure gradient, a

so-called force-balanced discretisation, and conserves the force applied to the flow, on arbitrary meshes. Furthermore, the application of a density weighting in the MWI has been analysed from a theoretical perspective and shown to have a stabilising effect on flows with large density ratios. Without such a treatment, the fluid would be accelerated without limit, resulting in divergence of the solution algorithm. MWI can also play a vital role in simulating low Mach number flows using pressure-based algorithms to overcome the weak pressure-density coupling when the compressibility of the flow is negligible, as demonstrated by the presented results.

In summary, MWI is very effective in maintaining pressure-velocity coupling in simulations of incompressible and low Mach number flows on meshes with collocated variable arrangement, but the effect of external forces, and of the discrete approximations itself, on the discretised pressure gradient have to be carefully accounted for to obtain physically realistic results and robust solutions. In all considered cases, the proposed MWI has been shown to offer superior accuracy and stability compared to the considered alternatives, in particular with regards to meshes with large non-orthogonality and in flows that are subject to discontinuous source terms or large density differences.

Chapter 3

Solution of the Two-Fluid Model

In this chapter the semi- and fully-coupled algorithms for solving the two-fluid model are developed. The two-fluid model with closures used for gas-solid flows is presented and discretised following chapter 2. The semi- and fully-coupled algorithms are developed by applying Picard and Newton linearisation, respectively to the resulting system of non-linear equations and proposals made to enhance the numerical properties of the fully-coupled algorithm. The chapter is concluded by comparing the semi- and fully-coupled algorithms by application to a range of test cases, culminating in the simulation of a fluidised bed.

3.1 Introduction

Dispersed two-phase flows, consisting of droplets or particles carried by a continuous fluid, are commonly found in nature and in a variety of engineering, industrial and scientific applications. The ability to be able to predict these flows with computational models is therefore very important. However, the computational prediction of these flows is still very complicated, both from a numerical as well from a physical point of view. The challenge lies in the fact that such flows typically contain many millions or billions of particles, resulting in a significant, or insurmountable, computational cost when aiming to resolve the behaviour of every individual particle and/or droplet [3, 47]. Here the dispersed phase will be referred to as particles, but this is interchangeable with droplets.

Rather than tracking individual particles, the two-fluid model [2, 47] employs a statistical

averaging of the behaviour of the dispersed phase as well as the continuous fluid surrounding the particles. The resulting continuum description of the particles allows the use of efficient solver algorithms developed for fluid flows, hence the computational effort required is no longer directly related to the number of particles. However, the drawback of averaging is that the information relating to individual particles is lost, and only their statistics are known as a function of time and space. This necessitates the application of closure models.

The resulting system of statistical equations describing the fluid and dispersed continua are similar to the Navier Stokes equations for each of the phases. However, additional variables and terms are introduced, such as the volume fractions and inter-phase exchange terms. Moreover, the equation system also contains a transport equation for volume fraction, which can be interpreted as a continuity equation for the corresponding phase. To obtain a solution to this system of equations is still computationally expensive, compounded by the need to satisfy various non-linearities, placing a premium on an efficient algorithm. Further complicating the solution of the two-fluid system is the large and rapid variation of fluid properties and source terms in combination with strong inter-phase coupling terms arising from the interactions of the phases, such as drag.

Most current solution frameworks for the two-fluid model treat each of the equations in a segregated fashion. They are typically based on the solution of the single phase Navier-Stokes equations, such as the widely used Inter-Phase Slip Algorithm (IPSA), developed by Spalding [84] as an evolution of the Semi-Implicit Method for Pressure Linked Equations (SIMPLE) family of algorithms [71] to two-phase flows. This typically involves a procedure in which the set of momentum equations are solved, subsequently a pressure correction equation is solved, and finally the transport equations for the volume fractions are solved. This constitutes one so-called "outer" iteration. Due to this segregated approach, strong inter-phase couplings are not taken into account implicitly, and the algorithm may result in so-called "frozen" solutions when the coupling terms dominate the equations, requiring a large number of outer iterations of the discretised equation system to reduce the effect of inter-equation couplings [60, 84]. A further difficulty, in common with the SIMPLE family of algorithms, is the requirement to specify under-relaxation factors to reach convergence of the algorithm [71, 97], in addition to poor scaling to large domains [97]. The need to apply under-relaxation factors stems from the decoupling of the pressure and velocity in the solution algorithm: a large forcing term results

in a large velocity update, and correspondingly a large pressure correction. This is inherently unstable, hence under-relaxation is used to prevent overly-large solution steps being taken, increasing stability. However, for computational efficiency, it is desirable to use as large a value of under-relaxation factor as possible; unfortunately there is no systematic way to choose this value a-priori.

As available computational resources have increased, coupled algorithms have emerged as an attractive alternative for the robust treatment of pressure-velocity coupling [92]. This has been facilitated by the development of discretisation algorithms, permitting the use of collocated variables on complex meshes, such as MWI, first proposed by Rhie and Chow [76], easing the burden of implementing a coupled solver [80, 90]. By solving a coupled system of equations for the velocity and pressure unknowns, a more robust pressure-velocity coupling may result [90], in addition to which, the poor scaling of segregated algorithms can be avoided [21, 24]. It is this potential for robustness which makes coupled algorithms particularly attractive for multiphase flow solvers, which must be capable of dealing with large (both magnitudes, and gradients of) source terms [31].

In the context of the two-fluid model, a coupled algorithm has the additional advantage of being able to implicitly account for inter-phase couplings, such as the inter-phase momentum exchanges, overcoming the issue of "frozen" solutions which are encountered when using a segregated algorithm [24, 25]. To date, coupled algorithms for the two-fluid model have focused solely on the pressure-velocity coupling [24, 25], solving the transport equations of the volume fractions separately. Therefore, these algorithms are referred to as "semi-coupled". In the semi-coupled approach, there is a lag between the pressure-velocity and volume fraction solutions, and as a result, continuity is only enforced for one phase during the solution procedure until final convergence is reached [22]. Therefore, outer iterations to ensure continuity is satisfied for both phases are still required.

In this work, a semi-coupled algorithm is implemented in the context of the unstructured, coupled pressure-velocity solver developed by Denner and van Wachem [31]. This semi-coupled algorithm is used as a reference algorithm. Additionally, a fully-coupled algorithm, treating the pressure, velocity and volume fractions as a single system of coupled equations is derived, validated, and compared to the semi-coupled algorithm. The fully-coupled algorithm has several theoretical advantages: given a good initial estimate, an (inexact) Newton method converges

rapidly [26, 56], continuity is enforced for all phases at each iteration due to the implicit treatment of phase transport, and new approaches to treat the various non-linear terms, such as linearising source terms against volume fraction become possible, leading to an increase in robustness.

Both the semi-coupled and fully-coupled algorithms are tested against a range of test cases, starting from the academic problem of two identical fluids flowing as a single fluid, progressing to horizontal and vertical two-phase flows and culminating in a fluidised bed case, representative of an industrial application of the algorithms. As identical models are used to close the equation system, the focus is on comparing the relative performance of the semi- and fully-coupled algorithms, with the semi-coupled algorithm serving as a baseline to measure the fully-coupled algorithm against. Where possible the solutions are also compared against analytical data to validate the implementations. Whilst the focus of this work is on dispersed gas-solid flows, the presented algorithms are, in principle, applicable to the simulation of two-phase flows generally using the Eulerian-Eulerian or two-fluid model.

This chapter is organised as follows. Section 3.2 introduces the two-fluid model governing equations and closure models. The discretisation of these equations including the MWI for two phases is described in §3.3 along with linearisation approaches, leading to the semi- and fully-coupled algorithms. The performance of both algorithms is then verified and compared by application to a number of test cases in §3.4, and the findings concluded in §3.5.

3.2 The Two-Fluid Model

Whilst truly direct numerical simulation of multiphase flows is possible in some simple cases, the number of internal boundaries and the range of scales quickly becomes unmanageable when considering most multiphase flows. Therefore, rather than explicitly tracking the material motion of each phase, a statistical approach to predict such flows can be adopted. A statistical approach aims at determining the probability of finding each phase with specific properties at a given point and time. Such an approach describes each phase in terms of a Probability Density Function (PDF) which may then be ensemble averaged to obtain a description of the flow in terms of continuum quantities. If the equations from this framework are appropriately derived [2, 47], averaged equations are obtained, describing each phase as separate interpenetrating continua. The averaged equations are for the individual volume fractions, the velocity fields, and a

combined pressure field. Throughout this chapter, the presentation will be given for two phases only, however, the extension to more than two phases is straightforward and follows the same procedure.

The derivation of the framework is omitted for brevity, but can be found in, for example [82]. Following the averaging over the PDF for each phase, the two-fluid transport equation for a property ϕ of phase number k, denoted by the variable ϕ^k is given as [2, 47]:

$$\frac{\partial \alpha^k \rho^k \phi^k}{\partial t} + \frac{\partial \alpha^k \rho^k \phi^k u_i^k}{\partial x_i} = \frac{\partial \alpha^k J_i^{\phi^k}}{\partial x_i} + \alpha^k S^{\phi^k} + I^{\phi^{kl}} \tag{3.1}$$

where α^k is the volume fraction, ρ^k the density, $\boldsymbol{J}^{\phi^k}$ the diffusive flux, S^{ϕ^k} the source term, t is time, $\boldsymbol{u}^k$ the velocity field of phase k, $\boldsymbol{x}$ the Cartesian coordinate and $I^{\phi^{kl}}$ is the exchange term accounting for the transfer of property ϕ between the phases k and l. Throughout this chapter, unless otherwise stated, subscript Latin characters are used as tensor indices, where Einstein summation is implied, and superscript Latin characters as phase counters.

The symbol ϕ^k can be set to be any of the fluid phase properties, and setting ϕ^k and making appropriate choices for the terms $\boldsymbol{J}^{\phi^k}$, S^{ϕ^k} and $I^{\phi^{kl}}$, the two-fluid governing equations are obtained.

When ϕ^k is set to be unity, the phase continuity equation of phase k is obtained. Assuming that there is no exchange of mass between the phases, it is given by

$$\frac{\partial \alpha^k \rho^k}{\partial t} + \frac{\partial \alpha^k \rho^k u_i^k}{\partial x_i} = 0 \tag{3.2}$$

which for a constant density for each phase further simplifies to

$$\frac{\partial \alpha^k}{\partial t} + \frac{\partial \alpha^k u_i^k}{\partial x_i} = 0 \tag{3.3}$$

which is a transport equation for volume fraction. The volume fraction, defined as the mass average of the PDF, describes the probability of encountering a phase at a specific location and

time. The volume fraction is, by definition, subject to the following constraints

$$0 \leq \alpha^k \leq 1 \tag{3.4}$$

$$\sum_k \alpha^k = 1 \tag{3.5}$$

When the transport equations for the volume fractions, Eq. (3.3), of all the phases are summed together, a statement of conservation of the total local volume is obtained. This is referred to as the global continuity equation. Because of the constraints on volume fractions expressed above, the sum of all the transient derivatives in the summed transport equations for volume fractions is zero. The global continuity equation, therefore, is

$$\sum_k \frac{\partial \alpha^k u_i^k}{\partial x_i} = 0 \tag{3.6}$$

This is the two-fluid model equivalent of the continuity equation for a single phase flow, assuming a constant density.

The momentum equations of the two-fluid model are obtained by setting the unknown property of each of the phases to the velocity field, $\phi^k = u_j^k$. Assuming no mass transfer between the phases and a constant density for each of the phases the momentum equations are:

$$\rho^k \frac{\partial \alpha^k u_j^k}{\partial t} + \rho^k \frac{\partial \alpha^k u_j^k u_i^k}{\partial x_i} = -\alpha^k \frac{\partial p}{\partial x_j} + \frac{\partial \alpha^k \tau_{ij}^k}{\partial x_i} + \alpha^k S_j^k - \frac{\partial p^k}{\partial x_j} + \beta^u \left(u_j^{l \neq k} - u_j^k. \right) \tag{3.7}$$

where $\boldsymbol{\tau}^k$ the shear stress tensor, $\boldsymbol{S}^k$ the momentum source term, and the last term is a generalised drag term [47], which comprises of a momentum exchange coefficient, β^u, multiplied by the relative velocity between the phases. The superscript $l \neq k$ denotes a phase l which is not phase k. The common pressure is denoted by p and p^k is the additional phase-specific pressure. Both pressures are taken out of the general stress term. Unlike the transport equations for the volume fractions, the momentum equations contain numerous un-closed terms: the phase pressures, shear stress tensors and the momentum exchange term.

To exemplify the applications of the two-fluid model, the current work will take gas-solid flow as a working example. The superscript g will denote the continuous, or gas phase. The superscript s will denote the solids, or dispersed phase. However, the algorithms developed

are also applicable to any other application of the two-fluid model. As gas-solid flow is taken as an example, some common closure relations are used for the un-closed terms mentioned above. Examples of the closure models for the un-closed terms for gas-solid flow applications are summarised in table 3.1 and are briefly explained below. It is noted that other closure relations can also be adopted in the derived framework.

Table 3.1: Closure models for the two-fluid momentum equations for gas-solid flow, used in this work.

Quantity	Expression	Model Description	Reference
p^g	0	gas-phase pressure	-
p^s	$p^{s,KT} + p^{s,Fr}$	solids pressure	[89]
τ_{ij}^k	$\mu^k \left(\frac{\partial u_j^k}{\partial x_i} + \frac{\partial u_i^k}{\partial x_j} \right) + \left(\lambda^k - \frac{2}{3}\mu^k \right) \frac{\partial u_k^k}{\partial x_k} \delta_{ij}$	Newtonian stress tensor	-
β^u	$\alpha^s \left(1-\alpha^s\right) \frac{3}{4} \frac{\rho^g \left\|\boldsymbol{u}^g - \boldsymbol{u}^s\right\|}{d^p} C^D (1-\alpha^s)^{-2.65}$	inter-phase momentum transfer	[95]

3.2.1 Inter-phase Momentum Transfer

The inter-phase momentum transfer arises from the drag force between the continuous fluid and each of the dispersed particles. For the examples presented in this work, the model of Wen and Yu [95] is applied, as this model is applicable to predict the drag force over a wide range of solid volume fractions and particle Reynolds numbers [89]. The drag coefficient, C^D, required to close the expression for β^u is given by a modified form of that proposed by Schiller and Nauman [16] up to particle Reynolds numbers of 1000, and approximated by a constant value at higher particle Reynolds numbers

$$C^D = \begin{cases} \frac{24}{(1-\alpha^s)Re^p} \left(1 + 0.15((1-\alpha^s)\,Re^p)^{0.687}\right) & \text{if } (1-\alpha^s)\,Re^p < 1000 \\ 0.44 & \text{otherwise} \end{cases} \tag{3.8}$$

where Re^p is the particle Reynolds number, given as

$$Re^p = \frac{\rho^g \left|\boldsymbol{u}^g - \boldsymbol{u}^s\right| d^p}{\mu^g} \tag{3.9}$$

and in the above equations d^p is the particle diameter and μ^g the dynamic viscosity of the continuous phase, which will be taken as a gas.

3.2.2 Stress Tensor Closure

In the two-fluid model there are two pressure contributions: a shared, or hydrodynamic pressure, p, and a possible, phase-specific additional pressure, p^k. The phase specific pressure for the continuous phase is zero, as only the hydrodynamic pressure p acts on this phase. However, the solids phase has an additional phase specific pressure contribution, the so-called solids pressure, arising from inter-particle interactions.

The shear stresses of each phase follow a Newton stress model as given in table 3.1, where μ^k is the dynamic viscosity of the phase and λ^k the bulk viscosity.

To close the solid phase stress tensor (pressure and shear stress contributions), constitutive relationships are required for the solid phase pressure, dynamic, and bulk, viscosities. At low to moderate volume fractions, the Kinetic Theory of Granular Flows (KTGF) [61] predicts the behaviour of the dispersed phase by analogy with the kinetic theory of dense gases. When the concentration of particles becomes high, the assumption of instantaneous particle-particle interactions made by KTGF is no longer valid, and frictional interactions begin to dominate, requiring a frictional rheological model to predict the behaviour of the solids phase.

3.2.2.1 Kinetic Theory of Granular Flows

As a result of the averaging procedure in deriving the two-fluid model, information about the behaviour of the individual particles is lost, analogous to the loss of the behaviour of the individual molecules in the continuum description of a fluid. However, a transport equation for any averaged property can be constructed. For example, the behaviour of the so-called "granular temperature", Θ^s, can be predicted by the transport equation [61]

$$\frac{3}{2}\rho^s\left(\frac{\partial\alpha^s\Theta^s}{\partial t}+\frac{\partial\alpha^s\Theta^s u_i^s}{\partial x_i}\right)=\frac{\partial}{\partial x_i}\left(\alpha^s\kappa^s\frac{\partial\Theta^s}{\partial x_i}\right)-\left(p^s\delta_{ij}-\alpha^s\tau_{ij}^s\right)\frac{\partial u_i^s}{\partial x_j}+\mathcal{J}^s-\gamma^s \tag{3.10}$$

where the granular temperature is given by

$$\Theta^s=\frac{1}{3}\left\langle \boldsymbol{c}^{p\prime 2}\right\rangle \tag{3.11}$$

where $\boldsymbol{c}^{p\prime}$ represents the fluctuating velocity of the particles [61].

The terms on the right hand side of the transport equation for granular temperature, Eq. (3.10),

are interpreted as follows: (i) the diffusion of granular temperature due to conduction through the solid phase continuum, (ii) production due to velocity gradients, (iii) production or dissipation due to fluctuating drag forces, and (iv) dissipation of granular temperature due to the inelastic nature of particle-particle collisions.

Based on kinetic theory, the constitutive models for the solids phase stress tensor are expressed in terms of the granular temperature. The expressions are shown in table 3.2, together with the closures for the transport equation for granular temperature. The symbol e^s represents the particle coefficient of restitution, g_0 the radial distribution function and l^s is the mean free path associated with the particles. The symbol $\alpha^{s,MAX}$ is the maximum solids volume fraction, the maximum packing limit, and is approximately 0.65.

Table 3.2: Expressions for the solids phase closure terms arising from kinetic theory.

Symbol	Model [42, 61]	Description
$p^{s,KT}$	$\alpha^s \rho^s \Theta^s \Big(1 + 2\alpha^s \left(1 + e^s\right) g_0\Big)$	granular pressure
$\mu^{s,KT}$	$\rho^s l^s \sqrt{\Theta^s}$	granular shear viscosity
λ^s	$\rho^s \frac{4}{3\sqrt{\pi}} d^p \left(1 + e^s\right) g_0 \sqrt{\Theta^s}$	granular bulk viscosity
κ^s	$2\alpha^s \rho^s d^p g_0 \left(1 + e^s\right) \sqrt{\frac{\Theta^s}{\pi}} + \frac{75}{192} \frac{\rho^s d^p \sqrt{\Theta^s \pi}}{(1+e^s)\alpha^s g_0} \left(1 + \frac{6}{5}\left(1 + e^s\right)\alpha^s g_0\right)^2$	granular energy diffusivity
γ^s	$3\left(1 - e^{s2}\right)\alpha^{s2} \rho^s g_0 \Theta^s \left(\frac{4}{d^p}\sqrt{\frac{\Theta^s}{\pi}} - \frac{\partial u_i^s}{\partial x_i}\right)$	dissipation of granular energy
$\mathcal{J}^s$	$\beta^u \left(\frac{\beta^u d^p (\boldsymbol{u}^g - \boldsymbol{u}^s)^2}{4\alpha^s \rho^s g_0 \sqrt{\pi \Theta^s}} - 3\Theta^s\right)$	granular energy production
g_0	$\frac{1}{1 - \left(\frac{\alpha^s}{\alpha^{s,MAX}}\right)^{1/3}}$	radial distribution function
l^s	$\frac{4}{5}\alpha^s d^p \left(1 + e^s\right) \frac{g_0}{\sqrt{\pi}} + \frac{10}{96} \frac{d^p \sqrt{\pi}}{(1+e^s)\alpha^s g_0} \left(1 + \frac{4}{5}\left(1 + e^s\right)\alpha^s g_0\right)^2$	particle mean free path

3.2.2.2 Frictional Stress Model

The models based on kinetic theory of granular flow (KTGF) are only valid when particle collisions are binary and instantaneous. Although this assumption may be reasonable at dilute particle concentrations, at higher concentrations these assumptions are violated and particle interactions are governed by many, non-instantaneous interactions, which involve friction. To describe the stresses arising at high particle volume fraction, a semi-empirical frictional stress

model is adopted [51, 52]. The expression for the solids frictional pressure and viscosity are

$$p^{s,Fr} = \begin{cases} Fr\frac{\left(\alpha^s - \alpha^{s,MIN}\right)^n}{\left(\alpha^{s,MAX} - \alpha^s\right)^p} & \alpha^s > \alpha^{s,MIN} \\ 0 & \text{otherwise} \end{cases} \tag{3.12}$$

$$\mu^{s,Fr} = p^{s,Fr} \sin\theta_s \tag{3.13}$$

where $\alpha^{s,MIN} = 0.5$ is the "kick-in" solids volume fraction, at which the frictional stress model starts to contribute to the solids stress, θ_s is the internal angle of friction, and Fr, p and n are empirical constants [51]. Generally, the frictional and kinetic contributions to the stress tensor are added together to give the total solid phase pressure and dynamic viscosity [8]

$$p^s = p^{s,KT} + p^{s,Fr} \tag{3.14}$$

$$\mu^s = \mu^{s,KT} + \mu^{s,Fr} \tag{3.15}$$

The above closure relations are taken as an example to close the two-fluid model for gas-solid flow. Other closures can be used for different multiphase flow types, such as bubbly flows. However, the algorithms for solving the two-fluid model as presented in this work are generally applicable.

3.3 Numerical Method

In this section the newly proposed framework to solve the two-fluid model is derived. The framework builds upon the coupled pressure-velocity framework to solve single phase flows on collocated, unstructured meshes as presented by Denner and van Wachem [31]. The single phase framework treats the momentum and continuity equations as a single, implicitly coupled system of linearised algebraic equations, which is solved to obtain the velocity and pressure fields. In the case of single phase flow, the momentum equations and the continuity equation are solved together in the form of

$$\begin{bmatrix} \mathcal{A} & \mathcal{B} \\ \mathcal{H} & \mathbf{0} \end{bmatrix} \cdot \begin{pmatrix} \mathbf{u} \\ p \end{pmatrix} = \begin{pmatrix} \mathbf{S} \\ 0 \end{pmatrix} \tag{3.16}$$

where $\mathcal{A}$ represents the operator combining the transient and convection terms from the momentum equation, $\mathcal{B}$ represents the operator for the pressure gradient arising in the momentum

equations, and $\mathcal{H}$ is the divergence operator arising from the continuity equation. The zero on the diagonal indicates that the pressure does not appear in the continuity equation for the fluid. However, in practice a dependency on the pressure is introduced, to facilitate solving the above system of equations. This will be discussed in detail in the next section.

An equivalent system of equations for the two-fluid model in a similar form can be constructed, by using the 9 governing equations of the two-fluid model. These governing equations are: 3 momentum equations for the first phase, 3 momentum equations for the second phase, 2 transport equations for the volume fractions, and one global continuity equation, enforcing the summation of volume fractions to unity. The coupled system to solve the governing equations of the two-fluid model can then be expressed as

$$\begin{bmatrix} \mathcal{A}^g + \mathcal{D} & -\mathcal{D} & \alpha^g \mathcal{B} & \mathbf{0} & \mathbf{0} \\ -\mathcal{D} & \mathcal{A}^s + \mathcal{D} & \alpha^s \mathcal{B} & \mathbf{0} & \mathbf{0} \\ \mathcal{H}^g & \mathcal{H}^s & \mathbf{0} & \mathbf{0} & \mathbf{0} \\ \mathbf{0} & \mathbf{0} & \mathbf{0} & \mathcal{E}^g & \mathbf{0} \\ \mathbf{0} & \mathbf{0} & \mathbf{0} & \mathbf{0} & \mathcal{E}^s \end{bmatrix} \cdot \begin{pmatrix} u_j^g \\ u_j^s \\ p \\ \alpha^g \\ \alpha^s \end{pmatrix} = \begin{pmatrix} \alpha^g S_j^g + \dfrac{\partial}{\partial x_i}\left(\alpha^g \left(\lambda^g - \dfrac{2}{3}\mu^g\right)\dfrac{\partial u_k^g}{\partial x_k}\delta_{ij}\right) \\ \alpha^s S_j^s - \dfrac{\partial p^s}{\partial x_j} + \dfrac{\partial}{\partial x_i}\left(\alpha^s \left(\lambda^s - \dfrac{2}{3}\mu^s\right)\dfrac{\partial u_k^s}{\partial x_k}\delta_{ij}\right) \\ 0 \\ 0 \\ 0 \end{pmatrix} \tag{3.17}$$

where the top line is constructed from the momentum equations of the continuous fluid, the second line is constructed from the momentum equations of the dispersed phase, the third line is constructed from the global continuity equation, and the last two lines are given by the individual transport equations for volume fractions of the continuous phase and the dispersed

phase. The operators in the above system of equations can be expressed algebraically as

$$\begin{aligned}\mathcal{A}^k =& \rho^k \frac{\partial \alpha^k \left(\cdot\right)}{\partial t} + \rho^k \frac{\partial \alpha^k \left(\cdot\right) u_i^k}{\partial x_i} \\ & - \frac{\partial}{\partial x_i}\left[\alpha^k \mu^k \left(\frac{\partial \left(\cdot\right)}{\partial x_i} + \left(\frac{\partial \left(\cdot\right)}{\partial x_i}\right)^T\right)\right]\end{aligned} \tag{3.18}$$

$$\mathcal{D} = \beta\left(\cdot\right) \tag{3.19}$$

$$\mathcal{B} = \frac{\partial \left(\cdot\right)}{\partial x_j} \tag{3.20}$$

$$\mathcal{H}^k = \frac{\partial \alpha^k \left(\cdot\right)}{\partial x_j} \tag{3.21}$$

$$\mathcal{E}^k = \frac{\partial \left(\cdot\right)}{\partial t} + \frac{\partial \left(\cdot\right) u_j^k}{\partial x_j} \tag{3.22}$$

where the superscript k can either indicate the continuous phase (g) or the dispersed phase (s).

The global continuity equation and the continuity equation for each of the phases (the final three lines in the coupled system, Eq. (3.17)) are not linearly independent, therefore one equation must be eliminated from the equation system. For instance, the continuity equation for the continuous phase is replaced by the constraint that the volume fractions sum to one. This constraint is implicitly satisfied by the substitution $\alpha^g = 1 - \alpha^s$, the continuity equation of one phase can then be eliminated from Eq. (3.17). The coupled set is then reduced from 9 to 8 equations. Although this choice is somewhat arbitrary, and other choices can be made, from a numerical perspective this choice has the advantage that a positive solution for both the volume fractions can be enforced by the appropriate discretisation, see for instance Patankar [71]. This will be further discussed in §3.3.2.3. Following this strategy, the set of coupled equations approximating the two-fluid model becomes

$$\begin{bmatrix} \mathbf{A}^g + \mathbf{D} & -\mathbf{D} & \alpha^g \mathbf{B} & \mathbf{0} \\ -\mathbf{D} & \mathbf{A}^s + \mathbf{D} & \alpha^s \mathbf{B} & \mathbf{0} \\ \mathbf{H}^{gg} + \mathbf{H}^{sg} & \mathbf{H}^{ss} + \mathbf{H}^{gs} & \mathbf{G}^g + \mathbf{G}^s & \mathbf{0} \\ \mathbf{0} & \mathbf{0} & \mathbf{0} & \mathbf{E}^s \end{bmatrix} \cdot \begin{pmatrix} u_j^g \\ u_j^s \\ p \\ \alpha^s \end{pmatrix} = \begin{pmatrix} b_j^{u^g} \\ b_j^{u^s} \\ b^p \\ b^{\alpha^s} \end{pmatrix} \tag{3.23}$$

where the sub-matrices represent the discretisation of the operators expressed in Eq. (3.17), except for introducing an operator on the diagonal of the global continuity equation. Hence, the global continuity equation will be, at least in discretised form, a function of pressure. The

derivation and exact form of these operators will follow from the appropriate discretisation of the two-fluid model and will be presented in §3.3.1. As the framework presented in this work aims at applying the two-fluid model in complex geometries, a collocated variable arrangement for the discretisation is chosen. To prevent pressure-velocity decoupling with a collocated variable arrangement, the so-called MWI is introduced in determining the fluxes at the cell faces [31, 76]. MWI introduces non-zero diagonals into the sub-matrices $\mathbf{G}^g$ and $\mathbf{G}^s$. This means that the discretised form of the global continuity equation and the transport equations for volume fraction will contain a dependency on the pressure. Although the derivation of the MWI for the two-fluid model has many similarities to its derivation for single phase flows, there are a number of differences. The most important difference is that each of the phases contributes to the discretisation of the fluxes of both phases at the cell face, leading to the sub-matrices $\mathbf{H}^{gg}$ and $\mathbf{H}^{sg}$, representing the contribution of the continuous phase to the MWI for continuous and dispersed phases, respectively. This also holds for the contribution of the dispersed phase on both of the phases, leading to the sub-matrices $\mathbf{H}^{ss}$ and $\mathbf{H}^{gs}$.

Although the discretised equation system, Eq. (3.23), appears as a linear system of equations, the system is non-linear because the coefficients in the matrix are not constants, but depend on the unknowns. Therefore, a strategy to linearise the system is required to develop an efficient approach to solve Eq. (3.23). This strategy is presented and discussed in §3.3.2. Two different strategies for the linearisation will be explored, leading to the semi-coupled and the fully-coupled approaches, which will be derived in the following sections.

3.3.1 Discretisation of the Two-Fluid Model

Using FVM, the discrete form of the multiphase transport equation for a variable of phase k, ϕ^k, Eq. (3.1), for cell P, as shown in *fig.* 3.1, is given as

$$\begin{aligned}\left(a^{\phi,k,P}+\alpha^{k,P}\frac{\rho^k}{\Delta t}V^P+\beta^{\phi,P}V^P\right)\phi^{k,P}+\sum_{f(P)}a^{\phi,k,F}\phi^{k,F}-\beta^{\phi,P}V^P\phi^{l\neq k,P}\\ =\alpha^{O,k,P}\frac{\rho^k}{\Delta t}\phi^{O,k,P}V^P+\alpha^{k,P}S^{\phi_k,P}V^P\end{aligned} \tag{3.24}$$

where $a^{\phi,k}$ are the coefficients arising from discretisation of the convection operator, Δt is the time-step and V^P is the cell volume. The superscripts P and F represent variables evaluated at

the central cell and the neighbour cell adjacent to face f, respectively, as depicted in *fig.* 3.1. The superscript O represents the value of a variable at the previous time-step and $\sum_{f(P)}$ implies the sum over all of the faces of cell P. The framework is described with a first-order backward discretisation in time, as is done in the above equation. This is done for clarity only, and the extension to higher order accurate discretisations in time is straightforward.

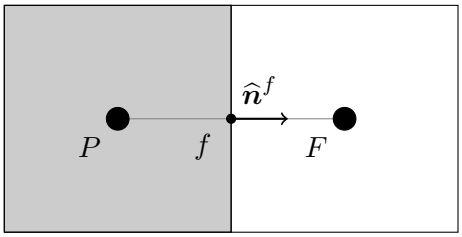

Figure 3.1: Control volume layout around a cell centred at point P and neighbouring cell F, showing the unit face normal vector $\widehat{\boldsymbol{n}}^f$ and the face centre f.

The coefficients following the discretisation of the convection term for phase k, $a^{\phi,k}$ are derived using a standard discretisation scheme [71] and are summarised as

$$a^{\phi,k,P} = \rho^k \sum_{f(P)} \alpha^{k,f} \psi^{\phi,k,f} \vartheta^{k,f} A^f + \sum_{f(P)} \frac{\Gamma^{*,\phi^k,f}}{|\mathbf{s}^f|} A^f \tag{3.25}$$

and

$$a^{\phi,k,F} = \rho^k \alpha^{k,f} \left(1 - \psi^{\phi,k,f}\right) \vartheta^{k,f} A^f - \frac{\Gamma^{*,\phi^k,f}}{|\mathbf{s}^f|} A^f \ . \tag{3.26}$$

In the above equations A^f represents the area of the cell face between cells P and F, $\widehat{\boldsymbol{n}}^f$ and $\boldsymbol{s}^f$ are the face normal vector and the vector on the line $P - F$, respectively, $\psi^{\phi,k,f}$ is a weighting coefficient determined by the chosen discretisation scheme applied to the advection terms, and $\Gamma^{*,\phi^k} = \alpha^k \Gamma^{\phi^k}$ is the effective diffusion coefficient. Although with Cartesian cells, as shown in *fig.* 3.1, the vectors $\widehat{\boldsymbol{n}}^f$ and $\widehat{\boldsymbol{s}}^f$ coincide, this will usually not be the case for non-Cartesian cells. The *advecting velocity* of phase k is defined as the product of the fluid velocity at the cell face with the cell face normal vector,

$$\vartheta^{k,f} = u_i^{k,f} \widehat{n}_i^f \tag{3.27}$$

For most of the variables which need to be evaluated at the face between two cells, f, an

appropriate linear combination of the cell centred variables is used

$$\phi^{k,f} = \psi^{\phi,k,f}\phi^{k,P} + \left(1 - \psi^{\phi,k,f}\right)\phi^{k,F} \tag{3.28}$$

One exception to this is the advecting velocity, required for the convective part of the transport equation. The advecting velocity requires a different type of interpolation. If a linear interpolation would be used, the solution would become unstable due to pressure-velocity decoupling [76]. As previously mentioned in §3.3, the MWI is employed to prevent pressure-velocity decoupling which may occur on collocated grids. In general terms, the interpolation is then expressed as

$$\vartheta^{k,f} = \overline{u}_i^{k,f}\widehat{n}_i^f + f\left(p, \alpha^k, \ldots\right) \tag{3.29}$$

where the overbar on the velocity terms indicates a linear interpolation from cell centres to the intervening face, as expressed by Eq. (3.28). The last term on the right hand side is a function of at least pressure and the volume fraction. The derivation leading to the exact form of this function will be presented in §3.3.1.4.

3.3.1.1 Momentum Equations

Following the procedure for the transport of a general transported variable ϕ^k, as outlined above, the momentum equations of the two-fluid model, Eq. (3.7) are discretised for the Cartesian direction j as follows

$$\begin{aligned}\left(a^{u_j,k,P} + \alpha^{k,P}\frac{\rho^k}{\Delta t}V^P + \beta^P V^P\right)u_j^{k,P} + \sum_{f(P)} a^{u_j,k,F}u_j^{k,F} - \beta^P u_j^{l\neq k,P}V^P + \alpha^{k,P}b_j^{k,P}p^P \\ +\alpha^{k,P}\sum_{f(P)} b_j^{k,F}p^F = \alpha^{k,P}S_j^{k,P}V^P - \left.\frac{\partial p^k}{\partial x_j}\right|^P V^P + \alpha^{O,k,P}\frac{\rho^{k,P}}{\Delta t}u_j^{O,k,P}V^P \\ + \sum_{f(P)}\mu^{*,k,f}\left.\frac{\partial u_i^k}{\partial x_j}\right|^f \widehat{n}_i^f A^f + \sum_{f(P)}\left(\lambda^{*,k,f} - \frac{2}{3}\mu^{*,k,f}\right)\left.\frac{\partial u_i^k}{\partial x_i}\right|^f \widehat{n}_j^f A^f\end{aligned} \tag{3.30}$$

where the coefficients $a^{u_j,k}$ are as given analogously as Eq. (3.25) and Eq. (3.26). The superscript F denotes the cell center variable adjacent to cell face f. The pressure coefficients, b^k, are obtained by applying Gauss' theorem to the pressure gradient and approximating the surface

integrals using the midpoint rule. The pressure gradients are approximated as

$$\int_{V_P} \frac{\partial p}{\partial x_j} dV \approx \sum_{f(P)} p^f \widehat{n}_i^f A^f \tag{3.31}$$

yielding

$$b_j^P = \sum_{f(P)} \psi^{p,f} \widehat{n}_j^f A^f \tag{3.32}$$

and

$$b_j^F = \left(1 - \psi^{p,f}\right) \widehat{n}_j^f A^f \ . \tag{3.33}$$

where $\psi^{p,f}$ is the factor to interpolate the pressure to the cell face, determined by inverse distance weighting. The implicit treatment of the pressure gradient obviates the need to under-relax the momentum equations as in segregated algorithms [71, 92], as the solution responds directly to large or rapidly changing pressure gradients. The implicit treatment of the inter-phase coupling terms is similarly robust, simplifying the implementation relative to segregated algorithms, which must employ techniques such as PEA [84] to obtain converged solutions when the coupling is strong [93].

The sub-matrices $\mathbf{A}^k$, $\mathbf{B}$ and $\mathbf{D}$ as shown in Eq. (3.23) are formed by collecting the convective and transient coefficients, the pressure coefficients and coefficients associated with the inter-phase coupling terms, whilst the terms on the right hand side of Eq. (3.30) are collected in the right hand side term $b^{u_j^k}$.

3.3.1.2 Transport Equations for Volume Fractions

The discretisation of the transport equations for the volume fractions for each of the phases follows a similar procedure as given by Eq. (3.24). The resulting discretised version of the transport equations for volume fraction is

$$\left(e^{k,P} + \frac{V^P}{\Delta t}\right) \alpha^{k,P} + \sum_{f(P)} e^{k,F} \alpha^{k,F} = \alpha^{O,k,P} \frac{V^P}{\Delta t} \tag{3.34}$$

Because the volume fraction is the transported variable, the coefficients e^k differ somewhat from the general convection coefficients $a^{\phi,k}$ and are given as

$$e^{k,P} = \sum_{f(P)} \psi^{\alpha,k,f} \vartheta^{k,f} A^f \tag{3.35}$$

and

$$e^{k,F} = \left(1 - \psi^{\alpha,k,f}\right) \vartheta^{k,f} A^f \tag{3.36}$$

and used with the transient coefficient to construct the matrix $\mathbf{E}^k$. As a bounded scalar, see Eq. (3.4), maintaining the bounds of volume fraction during the solution process is paramount, a bounded and conservative discretisation scheme, such as upwind differences, must be used to determine the interpolation coefficients, $\psi^{\alpha,k,f}$, when computing $e^{k,P}$ and $e^{k,F}$.

3.3.1.3 Global Continuity Equation

The global continuity equation, Eq. (3.6), provides a constraint on the combined motion of the two-fluid system. It is the two-fluid analogue of the continuity equation for single phase incompressible flows and, following a similar approach, is used to develop an equation for pressure [60]. Applying the FVM, the global continuity equation can be approximated in terms of unknowns at the faces of cell P,

$$\sum_k \sum_{f(P)} \alpha^{k,f} \vartheta^{k,f} A^f = 0 \tag{3.37}$$

where $\vartheta^{f,k}$ is the advecting velocity of phase k at cell face f, as introduced by Eq. (3.29). A suitable procedure for computing the advecting velocity is given in the next section.

3.3.1.4 Advecting Velocity

The expression for the advecting velocity is obtained by MWI, which has been introduced for single phase flows in, for instance, Denner and van Wachem [31]. Its derivation builds on averaging the discretised momentum equations to the cell face. Assuming the existence of a fictitious control volume located around the face centre, the momentum equations for that

control volume can be expressed in an *analogous* form of Eq. (3.30):

$$\left(1+\alpha^{k,f}c^k d^{k,f}+\beta^f d^{k,f}\right)u_i^{k,f} = \widetilde{u}_i^{k,f} - \alpha^{k,f}d^{k,f}\left.\frac{\partial p}{\partial x_i}\right|^f + \alpha^{O,k,f}c^k d^{k,f}u_i^{O,k,f} + \alpha^{k,f}d^{k,f}S_i^{k,f} + \beta^f d^{k,f}u_{l\neq k,f}^i \tag{3.38}$$

where the variables c^k, d^k and $\widetilde{\boldsymbol{u}}^k$ are introduced to simplify the notation and are defined as

$$c^k = \frac{\rho^k}{\Delta t} \tag{3.39}$$

$$d^{k,f} = \frac{V^f}{a^{k,f}} \tag{3.40}$$

$$\widetilde{u}_i^{k,f} = -\frac{1}{a^{k,f}}\sum_{q(f)}\left(a^{k,Q}u_i^{k,Q} - \mu^{*,k,q}\left.\frac{\partial u_j^k}{\partial x_i}\right|^q \widehat{n}_j^q A^q - \left(\lambda^{*,k,q}-\frac{2}{3}\mu^{*,k,q}\right)\left.\frac{\partial u_j^k}{\partial x_j}\right|^q \widehat{n}_i^q A^q\right) . \tag{3.41}$$

with a volume of V^f, the summation over q implies a summation over the faces of the fictitious control volume and Q is the adjacent cell centre to face q. The coefficients of Eq. (3.38) are approximated by linear interpolation, given by

$$\widetilde{u}_i^{k,f} = \overline{\widetilde{u}_i^k}^f = \frac{1}{2}\left(\widetilde{u}_i^{k,P}+\widetilde{u}_i^{k,F}\right) \tag{3.42}$$

with the corresponding cell-centred coefficients obtained from the cell-centred momentum equations. Substituting the expression for $\widetilde{u}_i^{k,f}$ given by Eq. (3.42) into Eq. (3.38) and dividing by the bracketed term on the left hand side, the following equation for the velocity at the cell face is obtained

$$\begin{aligned} u_i^{k,f} = {} & \overline{u}_i^{k,f} - \alpha^{k,f}\widehat{d}^{k,f}\left(\left.\frac{\partial p}{\partial x_i}\right|^f - \overline{\frac{\partial p}{\partial x_i}}^f\right) + \alpha^{O,k,f}c^k\widehat{d}^{k,f}\left(u_i^{O,k,f}-\overline{u}_i^{O,k,f}\right) \\ & + \alpha^{k,f}\widehat{d}^{k,f}\left(S_i^{k,f}-\overline{S}_i^{k,f}\right) + \beta^f\widehat{d}^{k,f}\left(u_i^{l\neq k,f}-\overline{u}_i^{l\neq k,f}\right) \\ & + \widehat{d}^{k,f}\left(\overline{\beta\left(u_i^k-u_i^{l\neq k}\right)}^f - \beta^f\left(\overline{u}_i^{k,f}-\overline{u}_i^{l\neq k,f}\right)\right) \end{aligned} \tag{3.43}$$

where

$$\widehat{d}^{k,f} = \frac{d^{k,f}}{1+\alpha^{k,f}c^k d^{k,f}+\beta^f d^{k,f}} . \tag{3.44}$$

In deriving Eq. (3.43), the approximation

$$d_{k,P} \approx d_{k,F} \approx d_{k,f} \tag{3.45}$$

is made so that the resulting pressure term acts as a low-pass filter operating on third-order and higher derivatives of pressure, suppressing unphysical pressure fields [31, 59, 86].

Due to the inter-phase coupling of the momentum equations, Eq. (3.43), is directly dependent on the face velocity of the other phase, $u_i^{l\neq k,f}$. This term can be evaluated by writing out the equivalent equation for the face velocity of the other phase, and substituting this expression back into Eq. (3.43). The resulting expression for the velocity at the face for phase k, $u_i^{k,f}$, then becomes

$$\begin{aligned} u_i^{k,f} = \overline{u}_i^{k,f} + \frac{\widehat{d}^{k,f}}{1-\beta^f{}^2 \widehat{d}^{k,f}\widehat{d}^{l\neq k,f}} \sum_{m=\text{phases}} \Upsilon^{m,f} \Bigg(-\alpha^{m,f} \left(\left.\frac{\partial p}{\partial x_i}\right|^f - \overline{\frac{\partial p}{\partial x_i}}^f \right) \\ + \alpha^{O,m,f} c^m \left(u_i^{O,m,f} - \overline{u}_i^{O,m,f} \right) + \alpha^{m,f} \left(S_i^{m,f} - \overline{S}_i^{m,f} \right) \\ + \left(\overline{\beta \left(u_i^m - u_i^{l\neq m} \right)}^f - \beta^f \left(\overline{u}_i^{m,f} - \overline{u}_i^{l\neq m,f} \right) \right) \Bigg) \end{aligned} \tag{3.46}$$

where with $\sum_{m=\text{phases}}$ a summation over all phases is indicated, and the definition for $\Upsilon^{m,f}$ is

$$\Upsilon^{m,f} = \begin{cases} 1 & \text{if } m = k \\ \beta^f \widehat{d}^{m,f} & \text{otherwise,} \end{cases} \tag{3.47}$$

accounting for the inter-phase coupling. This equation can be used to determine an expression for the advecting velocity, Eq. (3.27). The gradient of pressure at the face can then be approximated as

$$\left.\frac{\partial p}{\partial x_i}\right|^f \widehat{n}_i^f = \frac{p^F - p^P}{|\boldsymbol{s}^f|} \tag{3.48}$$

and the expression for the advecting velocity for phase k is then expressed as

$$\begin{aligned}\vartheta^{k,f} = u_i^{k,f}\widehat{n}_i^f = \overline{u}_i^{k,f}\widehat{n}_i^f + \frac{\widehat{d}^{k,f}}{1-\beta^f{}^2\widehat{d}^{k,f}\widehat{d}^{l\neq k,f}} \sum_{m=\text{phases}} \Upsilon^{m,f}\Bigg(-\alpha^{m,f}\left(\frac{p^F-p^P}{|\boldsymbol{s}^f|} - \overline{\frac{\partial p}{\partial x_i}}^f \widehat{n}_i^f\right) \\ + \alpha^{O,m,f}c^m\left(u_i^{O,m,f} - \overline{u}_i^{O,m,f}\right)\widehat{n}_i^f + \alpha^{m,f}\left(S_i^{m,f} - \overline{S}_i^{m,f}\right)\widehat{n}_i^f \\ + \left(\overline{\beta\left(u_m^i - u_{l\neq m}^i\right)}^f - \beta^f\left(\overline{u}_i^{m,f} - \overline{u}_i^{l\neq m,f}\right)\right)\widehat{n}_i^f\Bigg)\end{aligned} \quad . \tag{3.49}$$

Eq. (3.49) is the interpolation of the advecting velocity for phase k at the cell face f, previously expressed in general terms in Eq. (3.29). This expression for the advecting velocity of phase k consists of a linear interpolation of the velocity of phase k to the cell face, plus a number of higher order terms. These higher order terms aim to couple the pressure and the velocity and filter out higher order pressure oscillations, preventing so-called chequerboarding, similarly as MWI does for single phase flows [31].

The advecting velocity of phase k at the cell face is used to compute the coefficients describing the advection terms of the transport equations, such as in Eq. (3.25) and Eq. (3.26).

Substituting Eq. (3.49) into Eq. (3.37), and collecting terms, the discretisation of the global continuity equation is given as

$$\sum_{k=\text{ph.}}\sum_{m=\text{ph.}} h_i^{km,P}u_i^{m,P} + \sum_{k=\text{ph.}}\sum_{m=\text{ph.}}\sum_{f(P)} h_i^{km,F}u_i^{m,F} + \sum_{k=\text{ph.}} g^{k,P}p^P + \sum_{k=\text{ph.}}\sum_{f(P)} g^{k,F}p^F = \sum_{k=\text{ph.}} K^{k,P} \tag{3.50}$$

where the coefficients h_i^{km} and g^k form the sub-matrices $\mathbf{H}^{km}$ and $\mathbf{G}^k$ of Eq. (3.23) and $K^{k,P}$ collects all remaining terms of Eq. (3.49), forming the right hand side of the discretised equation of the global continuity. As shown in the derivation, the velocity of each phase contributes to the advecting velocity of the other phase due to the momentum coupling between the phases. The first contribution in the expression of the advecting velocity of phase k, Eq. (3.49) is the linear interpolation of velocities of that phase. Therefore, the coefficients

$$h_i^{kk,P} = \sum_{f(P)} \frac{1}{2}\alpha^{k,f}\widehat{n}_i^f A^f \tag{3.51}$$

and

$$h_i^{kk,F} = \frac{1}{2}\alpha^{k,f}\widehat{n}_i^f A^f \ . \tag{3.52}$$

for each of the neighbouring cells, F. The additional velocity contributions to the advecting velocity for phase k, arise from the inter-phase momentum exchange terms and are expressed for each of the phases as

$$h_i^{km,P} = \begin{cases} \sum_{f(P)} \frac{1}{2}\alpha^{k,f} \dfrac{\widehat{d}^{k,f}}{1-\beta^f{}^2 \widehat{d}^{k,f}\widehat{d}^{l\neq k,f}} \Upsilon^{m,f}\left(\beta^P - \beta^f\right)\widehat{n}_i^f A^f & m = k \\ -\sum_{f(P)} \frac{1}{2}\alpha^{k,f} \dfrac{\widehat{d}^{k,f}}{1-\beta^f{}^2 \widehat{d}^{k,f}\widehat{d}^{l\neq k,f}} \Upsilon^{m,f}\left(\beta^P - \beta^f\right)\widehat{n}_i^f A^f & m \neq k \end{cases} \tag{3.53}$$

and for the dependency on the neighbouring cell F

$$h_i^{km,F} = \begin{cases} \frac{1}{2}\alpha^{k,f} \dfrac{\widehat{d}^{k,f}}{1-\beta^f{}^2 \widehat{d}^{k,f}\widehat{d}^{l\neq k,f}} \Upsilon^{m,f}\left(\beta^F - \beta^f\right)\widehat{n}_i^f A^f & m = k \\ -\frac{1}{2}\alpha^{k,f} \dfrac{\widehat{d}^{k,f}}{1-\beta^f{}^2 \widehat{d}^{k,f}\widehat{d}^{l\neq k,f}} \Upsilon^{m,f}\left(\beta^F - \beta^f\right)\widehat{n}_i^f A^f & m \neq k \end{cases} . \tag{3.54}$$

The coefficients which determine the dependency on the pressure for phase k are given as

$$g^{k,P} = \sum_{f(P)} \alpha^{k,f} \frac{\widehat{d}^{k,f}}{1-\beta^f{}^2 \widehat{d}^{kf}\widehat{d}^{l\neq k,f}} \sum_m \Upsilon^{m,f} \frac{1}{|\boldsymbol{s}^f|}\widehat{n}_i^f A^f \tag{3.55}$$

and the dependency on the neighbouring cell F is given as

$$g^{k,F} = -\alpha^{k,f} \frac{\widehat{d}^{k,f}}{1-\beta^f{}^2 \widehat{d}^{k,f}\widehat{d}^{l\neq k,f}} \sum_m \Upsilon^{m,f} \frac{1}{|\boldsymbol{s}^f|}\widehat{n}_i^f A^f \tag{3.56}$$

and the terms which remain on the right hand side are given as

$$\begin{aligned} K^{k,P} = \sum_{f(P)} \alpha^{k,f} \frac{\widehat{d}^{k,f}}{1-\beta^f{}^2 \widehat{d}^{k,f}\widehat{d}^{l\neq k,f}} \sum_m \Upsilon^{m,f} \Bigg(& \overline{\frac{\partial p}{\partial x^i}}^f \widehat{n}_i^f + \alpha^{O,m,f} c^m \left(\vartheta^{O,m,f} - \overline{u}_i^{O,m,f}\widehat{n}_i^f\right) \\ & + \alpha^{m,f}\left(S_i^{m,f} - \overline{S}_i^m\right)\widehat{n}_i^f \Bigg) A^f \ . \end{aligned} \tag{3.57}$$

In the above equations, the cell-centred pressure gradients are treated explicitly for clarity of presentation, however an implicit treatment, replacing the explicitly computed pressure gradients

in $K^{k,P}$ with the coefficients used to evaluate the pressure gradient in the momentum equations, may yield better convergence at the cost of a larger stencil.

The coefficients required in the discretised forms of Eq. (3.30), Eq. (3.34) and Eq. (3.50) are not constant in time, as they depend on the unknowns. Therefore, a strategy to treat the non-linearity of the coupled set of equations must be developed. This is presented in the next section.

3.3.2 Linearisation of the Coupled System

To solve the non-linear discrete system presented by Eq. (3.23), two approaches are immediately apparent: Picard linearisation and Newton linearisation [97]. Both of these approaches are pursued below. To clarify the discussion, Eq. (3.23) can be expressed in simplified form as

$$\mathbf{M} \cdot \boldsymbol{\phi} = \mathbf{b} \tag{3.58}$$

where $\mathbf{M}$ is the coefficient matrix, $\boldsymbol{\phi}$ the vector of unknowns and $\mathbf{b}$ the right hand side vector. Because the coefficient matrix and the right hand side vector are functions of the unknowns, they must be linearised prior to the application of a linear solver to determine the unknowns.

The simplest approach, widely used in CFD, is Picard linearisation [97]. In Picard linearisation, the coefficients and source terms are evaluated based on currently known values. This is also commonly referred to as "lagged values" being used to determine the coefficients. The application of Picard linearisation leads to the following linearised system:

$$\mathbf{M}^n \cdot \boldsymbol{\phi}^{n+1} = \mathbf{b}^n \tag{3.59}$$

where the superscript n indicates the iteration counter. Solution of Eq. (3.59) gives an updated unknown vector, which can be used to re-evaluate the coefficient matrix and source terms for the next iteration. Repeating this process, the vector of unknowns iteratively approaches the solution to Eq. (3.58), although convergence is not necessarily achieved.

An alternative to the application of Picard linearisation is Newton linearisation [97]. Newton linearisation is based on Newton's method for root finding, and may be applied to the solution of Eq. (3.58). For example, the non-linear term $\alpha^k u_i^k$ is approximated with Newton linearisation

as

$$\begin{aligned}\alpha^{k,n+1}u_i^{k,n+1} &\approx \alpha^{k,n}u_i^{k,n} + \left(\alpha^{k,n+1} - \alpha^{k,n}\right)\left.\frac{\partial \alpha^k u_i^k}{\partial \alpha^k}\right|^n + \left(u_i^{k,n+1} - u_i^{k,n}\right)\left.\frac{\partial \alpha^k u_i^k}{\partial u_i^k}\right|^n \\ &= \alpha^{n,k}u_i^{k,n+1} + \alpha^{k,n+1}u_i^{k,n} - \alpha^{k,n}u_i^{k,n}\end{aligned} \tag{3.60}$$

and is equivalent to solving the linearised system

$$\mathbf{J}^n \cdot \left(\boldsymbol{\phi}^{n+1} - \boldsymbol{\phi}^n\right) = -\mathbf{F}^n \tag{3.61}$$

where the Jacobian is given by

$$\mathbf{J}^n = \frac{\partial \mathbf{F}^n}{\partial \boldsymbol{\phi}} \tag{3.62}$$

and $\mathbf{F}^n = \mathbf{M}^n \cdot \boldsymbol{\phi}^n - \mathbf{b}^n = \mathbf{0}$ is the non-linear function for which a solution is sought, evaluated at the current time-step. As with Picard linearisation, this results in an iterative solution procedure in which the updated solution is used to reevaluate the non-linear function and Jacobian until a converged solution is obtained. However, the convergence behaviour of a system linearised with Newton is usually superior compared to applying Picard linearisation. The application of Picard and Newton linearisation to the two-fluid model equation system yields the semi- and fully-coupled algorithms respectively, discussed in the subsequent subsections.

3.3.2.1 Semi-Coupled Algorithm

Applying a Picard linearisation to the coupled set of equations, Eq. (3.23), results in the segregation of the upper-left and lower-right blocks, permitting the splitting into two smaller equation systems: a coupled pressure-velocity system, and a separate equation for solving the transport equation for the volume fraction. This semi-coupled algorithm derived in this work, is very similar to that proposed by Darwish *et al.* [25]. In the coupled pressure-velocity system, the volume fractions are kept lagged, and the pressure-velocity system is expressed as

$$\begin{bmatrix} \mathbf{A}^g + \mathbf{D} & -\mathbf{D} & \alpha^{g,n}\mathbf{B} \\ -\mathbf{D} & \mathbf{A}^s + \mathbf{D} & \alpha^{s,n}\mathbf{B} \\ \mathbf{H}^{gg} + \mathbf{H}^{sg} & \mathbf{H}^{ss} + \mathbf{H}^{gs} & \mathbf{G}^g + \mathbf{G}^s \end{bmatrix} \cdot \begin{pmatrix} u_j^g \\ u_j^s \\ p \end{pmatrix} = \begin{pmatrix} b_j^{u^g} \\ b_j^{u^s} \\ b_p \end{pmatrix} \tag{3.63}$$

and a separate equation to solve the volume fraction reads

$$\mathbf{E}^s \cdot \alpha^s = \mathbf{b}^{\alpha^s} \ . \tag{3.64}$$

The solution of Eq. (3.63) provides updated values for the pressure field and the velocity fields of both phases. Using these fields, the coefficients of Eq. (3.64) can be computed, which provides updated values for the volume fraction field. This semi-coupled algorithm is summarised in algorithm 1.

while $t < t^{end}$ **do**
  Initialise time-step;
  while *Not converged* **do**
    Solve coupled pressure-velocity system Eq. (3.63);
    Update advecting velocities;
    Solve volume fraction transport equation Eq. (3.64);
    Obtain fluid volume fraction as $\alpha^g = 1 - \alpha^s$;
    Check convergence;
    $n+ = 1$;
  end
  $t+ = \Delta t$.
end

Algorithm 1: Pseudo code describing the semi-coupled algorithm.

As Picard linearisation is used to approximate the non-linear advection term in the momentum equations, it may be required to solve Eq. (3.63) accurately, implying multiple inner iterations, before proceeding to solve Eq. (3.64). However, in practice, it is found that a single iteration of Eq. (3.63), followed by a single iteration of Eq. (3.64) within each outer iteration is sufficient to maintain stability whilst being significantly more computationally efficient.

Convergence is determined by a simple test, examining the change in volume fraction

$$\max_P \left(\left| \alpha^{k,P,n+1} - \alpha^{k,P,n} \right| \right) \leq \varepsilon^\alpha \tag{3.65}$$

where ε^α is a chosen tolerance in volume fraction. When this tolerance is achieved, the coupled pressure-velocity system must also have reached a converged solution.

By treating the inter-phase momentum exchange terms implicitly, the semi-coupled algorithm avoids lagging these source terms. This accelerates convergence and prevents the need for the application of under-relaxation factors. The convergence rate may, however, still be poor as the

volume fraction is segregated from the pressure-velocity equations.

3.3.2.2 The Fully-Coupled Algorithm

Applying Newton linearisation to Eq. (3.23), the Jacobian required for the algorithm is expressed as

$$\mathbf{J}\left(\boldsymbol{\phi}^{n}\right)=\left[\begin{array}{ccc|c} \mathbf{A}^{g}+\mathbf{D} & -\mathbf{D} & \alpha^{g,n}\mathbf{B} & \underline{-\mathbf{R}^{g}-\mathbf{B}p^{n}-\mathbf{T}^{g}} \\ -\mathbf{D} & \mathbf{A}^{s}+\mathbf{D} & \alpha^{s,n}\mathbf{B} & \underline{\mathbf{R}^{s}+\mathbf{B}p^{n}+\mathbf{T}^{s}} \\ \mathbf{H}^{gg}+\mathbf{H}^{sg} & \mathbf{H}^{ss}+\mathbf{H}^{gs} & \mathbf{G}^{g}+\mathbf{G}^{s} & \underline{-\mathbf{E}^{g}+\mathbf{E}^{s}} \\ \hline \underline{\mathbf{H}^{sg}} & \underline{\mathbf{H}^{ss}} & \underline{\mathbf{G}^{s}} & \mathbf{E}^{s} \end{array}\right] \tag{3.66}$$

The coefficients acting on the unknown α^g are negatives due to the substitution $\alpha^g = 1 - \alpha^s$. Compared to the previously discussed semi-coupled algorithm, there are a number of additional terms. These additional terms are underlined in the above equation, and arise due to the linearised coupling between the velocity-pressure system and the transport equations for the volume fractions. In contrast to the semi-coupled algorithm, this system can not be solved in a segregated fashion, and all equations are solved coupled, hence the current approach is referred to as the fully-coupled algorithm.

In developing the Newton linearisation of the two-fluid equation system, two simplifying assumptions are introduced by applying Picard linearisations to the advection and momentum exchange terms in the momentum equations, that is

$$\left(\alpha^{k,f}u_{j}^{k,f}u_{i}^{k,f}\right)^{n+1}\approx\left(\alpha^{k,f}u_{j}^{k,f}\right)^{n+1}u_{i}^{k,f,n} \tag{3.67}$$

and

$$\left[\beta^{P}\left(u_{j}^{k,P}-u_{j}^{l,P}\right)\right]^{n+1}\approx\beta^{P,n}\left(u_{j}^{k,P}-u_{j}^{l,P}\right)^{n+1} \tag{3.68}$$

as a result of which, the Jacobian retains similar coefficients compared to the Jacobian applied in the semi-coupled algorithm. This facilitates the simultaneous development of the semi- and fully-coupled algorithms, and does not affect the converged solution.

The coefficients in the sub-matrix $\mathbf{R}_k$ originate from discretising the transient and advection

terms in the momentum equations and the resulting coefficients are

$$r_j^{k,P} = u_j^{k,P,n} \frac{\rho^k}{\Delta t} V^P + \sum_{f(P)} \psi^{\alpha,k,f} u_j^{k,f,n} \vartheta^{k,f} A^f \tag{3.69}$$

and

$$r_j^{k,F} = \left(1 - \psi^{\alpha,k,f}\right) u_j^{k,f,n} \vartheta^{k,f} A^f \tag{3.70}$$

The sub-matrix $\mathbf{T}_k$ contains the coefficients from the linearisation of source terms in the momentum equations, with coefficients given as

$$t_j^{k,P} = \left(S_j^{k,P} + \alpha^{k,P,n} \frac{\partial S_j^{k,P}}{\partial \alpha^k} \right) - \sum_{f(P)} \psi^{\alpha,f} \left. \frac{\partial p^k}{\partial \alpha^k} \right|^P \widehat{n}_j^f A^f \tag{3.71}$$

and

$$t_j^{k,F} = - \left(1 - \psi^{\alpha,f}\right) \left. \frac{\partial p^k}{\partial \alpha^k} \right|^F \widehat{n}_j^f A^f \ . \tag{3.72}$$

In many closure models for multiphase flows the source terms are large and/or rapidly varying in time and space. In that case, the implicit treatment of these source terms increases the robustness of the algorithm [31]. In the above case, the source term containing the gradient of the solids pressure is treated implicitly with respect to the volume fractions. The exact form of the sub-matrix $\mathbf{T}_k$ depends on the source terms which are applied in the two-phase model. The coefficients as written down above, Eq. (3.71) and Eq. (3.72), are typical for the prediction of gas-solid flow. In particular, with reference to the solid phase $k = s$, Eq. (3.71) and Eq. (3.72) show how the fully-coupled discretisation enables the implicit treatment of the solids pressure gradient. Following the same discretisation practice as for the shared pressure p (Eq. (3.31), Eq. (3.32) and Eq. (3.33)), the discrete approximation of the solids pressure gradient is given as

$$\int_{CV_P} \frac{\partial p^s}{\partial x_j} dV = \sum_{f(P)} p_f^s \widehat{n}_j^f A^f = \sum_{f(P)} \left(\psi^{\alpha,f} p_P^s + \left(1 - \psi^{\alpha,f}\right) p_F^s \right) \widehat{n}_j^f A^f \tag{3.73}$$

however, unlike the shared pressure p, the solids pressure p^s is not a solution variable and must be expressed in terms of the solution variables if it is to be treated implicitly. Taking the definition of solids pressure given by Eq. (3.14) as an example, the solids pressure is linearised with respect to the solids phase volume fraction yielding

$$\begin{aligned} p^{s,n+1} &\approx p^{s,n} + \left(\alpha^{s,n+1} - \alpha^{s,n}\right) \frac{\partial p^{s,n}}{\partial \alpha^s} \\ &= p^{s,n} + \left(\alpha^{s,n+1} - \alpha^{s,n}\right) \left(\alpha^{s,n} \rho^s \Theta^{s,n} 2\left(1 + e^s\right) \left(2 g_0^n + \alpha^{s,n} \frac{\partial g_0}{\partial \alpha^s}\right)\right) \end{aligned} \tag{3.74}$$

the terms linear in $\alpha^{s,n+1}$ are then used to compute the contributions to the coefficients $t_j^{s,P}$ and $t_j^{s,F}$ in Eq. (3.71) and Eq. (3.72) respectively.

Newton linearisation is also applied to the transport equations for the volume fractions. The linearised solid phase continuity equation is given as

$$\left.\frac{\partial \alpha^{s,n+1}}{\partial t}\right|^P V^P + \sum_{f(P)} \left(\alpha^{s,f,n+1} \vartheta^{s,f,n} + \alpha^{s,f,n} \vartheta^{s,f,n+1} - \alpha^{s,f,n} \vartheta^{s,f,n}\right) A^f = 0 \ . \tag{3.75}$$

which when discretised yields the following algebraic equation

$$\begin{aligned} \left(e^{s,P} + \frac{V^P}{\Delta t}\right) \alpha^{s,P,n+1} + \sum_{f(P)} e^{s,F} \alpha^{s,F,n+1} + \sum_{m=\text{phs.}} h_i^{sm,P} u_i^{m,P,n+1} + \sum_{m=phs.} \sum_{f(P)} h_i^{sm,F} u_i^{m,F,n+1} \\ + g^{s,P} p^{P,n+1} + \sum_{f(P)} g^{s,F} p^{F,n+1} = \alpha^{O,s,P} \frac{V^P}{\Delta t} + K^{s,P} + \sum_{f(P)} \alpha^{n,s,f} \vartheta^{s,f,n} A^f \end{aligned} \tag{3.76}$$

where the coefficients are as defined previously. In the above equation, the coefficients h^{kl} and g^k appear to implicitly reconstruct the advective velocity at the cell faces at the new time-level, as it appears in Eq. (3.75).

The Newton linearisation of the transport equation for the volume fraction of the continuous (gas) phase yields a similar result as the above equation. The discretised and linearised transport equations for the two phases are added to form the discretised equation for global continuity. This forms the third line in Eq. (3.66), where, as in the momentum equations, the terms acting on the continuous phase volume fraction are negative due to the substitution $\alpha^g = 1 - \alpha^s$.

In almost all implicit computational fluid dynamic algorithms, the solution to the linear system is approximated using iterative linear solvers. The use of an iterative linear solver

implies that the linearised system, Eq. (3.61), is not satisfied exactly, instead an inexact Newton method [26] satisfies the equation

$$\left|\left|\mathbf{F}^n + \mathbf{J}^n \Delta\boldsymbol{\phi}^{n+1}\right|\right| \leq \eta^n \left|\left|\mathbf{F}^n\right|\right| \tag{3.77}$$

where $0 \leq \eta^n < 1$ is known as the forcing term [26] and $\eta^n = 0$ corresponds to the exact Newton method. The value of the forcing term may be varied as the solution proceeds to enhance stability and convergence rates [35], however, for time dependent problems, a constant value of forcing term is more appropriate [38], and is used in this work. Convergence of the linearised system is satisfied when

$$\frac{\left|\left|\mathbf{F}^n\right|\right|}{\left|\left|\mathbf{F}^0\right|\right|} \leq \varepsilon^{FC} \tag{3.78}$$

where $\mathbf{F}^0$ is the residual evaluated at the first iteration of the current time-step. The fully-coupled algorithm is then summarised in pseudo code in algorithm 2.

while $t < t^{end}$ **do**
    Initialise time-step;
    while *Not converged* **do**
        Set $0 \leq \eta^n < 1$;
        Solve fully-coupled system;
        Update solution using variables; Obtain second volume fraction from $\alpha^2 = 1 - \alpha^1$;
        Update advecting velocities;
        Check convergence using Eq. (3.78);
        $n+ = 1$;
    end
    $t+ = \Delta t$.
end

Algorithm 2: Pseudo code describing the fully-coupled algorithm.

The fully-coupled algorithm as laid out above does not require under-relaxation due to the implicit coupling of pressure and velocity and by treating the inter-phase momentum exchange implicitly. Furthermore, by solving both the global and phase continuity equations in a single system, discrete continuity for both phases is always satisfied. Additionally, as shown, the source term linear in volume fraction allows a further coupling of the two-fluid model equations, making

the solution procedure much more robust than a segregated one. This is especially important in cases where the inter-phase coupling is strong, such as in predictions of dense gas-solid flows or bubbly flows.

3.3.2.3 Boundedness of the Volume Fractions

In common with many transported scalar variables, *e.g.* temperature, physical considerations require that the volume fractions should remain bounded, and cannot become negative ($\alpha^k \geq 0$) or greater than one. This property can be enforced in the discretisation by using, for example, an upwind advection scheme [11, 71] as can be demonstrated by considering the application of the upwind scheme to Eq. (3.34). However, this result relies on the right hand side of the discretised equation being exclusively positive and is guaranteed in Eq. (3.34), assuming $\alpha^{k,O} \geq 0$.

However, this cannot be guaranteed when Newton linearisation is applied to the transport equations for the volume fractions. By rearranging Eq. (3.75), an equation can be obtained which resembles the same form as when the equation is linearised with Picard linearisation, plus an additional correction term on the right hand side:

$$\left(e^{k,P} + \frac{V^P}{\Delta t}\right)\alpha^{k,P,n+1} + \sum_{f(P)} e^{k,F}\alpha^{k,F,n+1} = \alpha^{O,k,P}\frac{V^P}{\Delta t} + \sum_{f(P)} \alpha^{k,f,n}\left(\vartheta^{k,f,n} - \vartheta^{k,f,n+1}\right)A^f \tag{3.79}$$

where the additional correction terms arising from the application of Newton linearisation is the last term on the right hand side. As the solution converges, this term approaches zero, hence the converged solution has the same guarantees for positive volume fractions as does the Picard linearised phase continuity equation. However, during the iterative solution process, the term $\left(\vartheta^{k,f,n} - \vartheta^{k,f,n+1}\right)$ can both be positive as well as negative.

Whilst the sign of ths term is unknown *a-priori*, the component consisting only of current values, that is $\alpha^{k,f,n}\vartheta^{k,f,n}$, is known and can be treated as a source term. These terms can be split, as outlined by Patankar [71], so the linearised contribution always remains positive. For illustration, consider the source term S_ϕ, which can be split as

$$S_\phi = S_\phi^u + S_\phi^p \phi^{n+1} \tag{3.80}$$

where

$$S_\phi^u = \max\left(S_\phi, 0\right) \tag{3.81}$$

$$S_\phi^p = \min\left(\frac{S_\phi}{\phi^n}, 0\right) \ . \tag{3.82}$$

In this way, the linearised source terms are guaranteed to be positive. An additional benefit is that the diagonal dominance of the system is possibly increased.

By applying this idea to the term $\sum_{f(P)} \alpha^{k,f,n}\vartheta^{k,f,n}A^f$, Eq. (3.79) is rewritten into

$$\begin{aligned}\left(e^{k,P} + \frac{\rho^{k,P}V^P}{\Delta t} - \frac{1}{\alpha^{k,P,n}}\sum_{f(P)}^{-}\alpha^{k,f,n}\vartheta^{k,f,n}A^f\right)\alpha^{k,P,n+1} =& \alpha^{k,P,O}\frac{\rho^{k,P}V^P}{\Delta t} - \sum_{f(P)} e^{k,F}\alpha^{k,F,n+1} \\ &+ \sum_{f(P)}^{+}\alpha^{k,f,n}\vartheta^{k,f,n}A_f - \sum_{f(P)}\alpha^{k,f,n}\vartheta^{k,f,n+1}A^f,\end{aligned} \tag{3.83}$$

where

$$\sum_{f(P)}^{-}\alpha^{k,f,n}\vartheta^{k,f,n}A^f = \min\left(\sum_{f(P)}\alpha^{k,f,n}\vartheta^{k,f,n}A^f, 0\right) \tag{3.84}$$

and

$$\sum_{f(P)}^{+}\alpha^{k,f,n}\vartheta^{k,f,n}A^f = \max\left(\sum_{f(P)}\alpha^{k,f,n}\vartheta^{k,f,n}A^f, 0\right) \tag{3.85}$$

Whilst this approach does not strictly guarantee a positive solution, due to this treatment it has been found to be very effective, which will be discussed during the presentation of the results. Respecting the boundedness of the volume fractions by the design of the discretisation scheme is vital for the fully-coupled algorithm. As soon as one of the volume fractions becomes negative, and therefore the other one exceeds unity, divergence will occur.

3.3.2.4 Diagonal Dominance

When numerically solving a linear system of equations using an iterative solver, diagonal dominance of the coefficient matrix is a desirable property as it is both a sufficient condition for

convergence of the linear solver, and contributes to maintaining bounded solutions [97]. Diagonal dominance may not always be achieved when Newton linearisation is applied in the fully-coupled framework. This can be examined by considering the coefficients resulting from the discretisation of the momentum equations. The coefficient on the diagonal arising from the transient term of the momentum equations of one of the phases is proportional to

$$\alpha^{k,P,n}\frac{\rho^k}{\Delta t}V^P \tag{3.86}$$

However, when Newton linearisation is applied, there is also an implicit term with respect to the volume fraction which is on the same line in the coefficient matrix. This coefficient is off-diagonal as it multiplies with the volume fraction. This off-diagonal coefficient is proportional to

$$u_j^{k,P,n}\frac{\rho^k}{\Delta t}V^P \tag{3.87}$$

When the volume fraction is small, as may be expected for the solid phase in dilute conditions, it is likely that $\left|u_j^{k,P,n}\right| \gg \alpha^{k,P,n}$ and the off-diagonal coefficient acting on the volume fraction is therefore larger than the coefficient acting on the velocity. This contravenes the diagonal dominance of the matrix which is to be solved. This issue does not appear for the transport equations for volume fraction or the global continuity equation, even when these are discretised with Newton linearisaton.

To ensure that the matrix containing the coefficients resulting from discretising the momentum equations remains diagonally dominant, a different discretisation strategy is proposed. So far, the conservative form of the two-fluid equations has been used to develop the discretisation strategy. The non-conservative and conservative form of the transport equation for an unknown ϕ^k are related by

$$\begin{aligned}\alpha^k\left(\frac{\partial\phi^k}{\partial t}+u_i^k\frac{\partial\phi^k}{\partial x_i}\right) &= \left(\frac{\partial\alpha^k\phi^k}{\partial t}+\frac{\partial\alpha^k\phi^k u_i^k}{\partial x_i}\right)-\phi^k\left(\frac{\partial\alpha^k}{\partial t}+\frac{\partial\alpha^k u_i^k}{\partial x_i}\right)\\ &= \frac{\partial\alpha^k\phi^k}{\partial t}+\frac{\partial\alpha^k\phi_k u_i^k}{\partial x_i}\end{aligned} \tag{3.88}$$

where the second bracketed term on the right hand side of the first line is identified as the continuity equation and is thus zero from an algebraic perspective. However, from a numerical point of view it is beneficial to keep the this second bracketed term in the discretisation, as it

ensures the conservative solution is reached when convergence is obtained [71]. The discretisation of this equation becomes

$$\alpha^{k,P,O}\frac{\phi^{k,P}-\phi^{k,P,O}}{\Delta t}+\sum_{f(P)}\alpha^{k,f}\vartheta^{k,f}\phi^{k,f}A^f-\phi^{k,P}\sum_{f(P)}\alpha^{k,f}\vartheta^{k,f}A^f=$$
$$\alpha^{k,P,O}\frac{\phi^{k,P}-\phi^{k,P,O}}{\Delta t}+\sum_{f(P)}\alpha^{k,f}\vartheta^{k,f}\left(\phi^{k,f}-\phi^{k,P}\right)A^f=RHS \tag{3.89}$$

where RHS contains all source, diffusion and inter-phase exchange terms. In the context of discretising the momentum equations in the fully-coupled algorithm, the transient term no longer depends on the volume fraction of the current time-step. Therefore, the potential large off-diagonal contribution, as shown by Eq. (3.87) has been averted.

The coefficients in the sub-matrix $\mathbf{R}_k$, which arise from discretising the transient and advection terms in the momentum equations, previously introduced in Eq. (3.69), now become

$$r_j^{k,P}=\sum_{f(P)}\psi^{\alpha,k,f}\left(u_j^{k,f,b}-u_j^{k,P,n}\right)\vartheta^{k,f}A^f \tag{3.90}$$

and

$$r_j^{k,F}=\left(1-\psi^{\alpha,k,f}\right)\left(u_j^{k,f,n}-u_j^{k,P,n}\right)\vartheta^{k,f}A^f \tag{3.91}$$

This way, the matrix with the coefficients of the discretised equations remains diagonally dominant, and the system is solvable with an iterative solver.

3.4 Simulations

Four test cases are used to evaluate and compare the semi- and fully-coupled algorithms. The first case simulates the flow of two identical fluids at the same velocity with an initially prescribed, non-constant volume fraction profile. Although this seems a trivial test case, it is used to validate the framework. The second test case concerns horizontal gas-solid flow, and the third test case concerns vertical gas-solid flow. Finally, the fourth test case will present a case of a gas-solid fluidised bed.

For comparison purposes, the same convergence criteria are applied for both the semi- and

fully-coupled algorithms. The criterion used is the norm of the global continuity error, *i.e.*

$$\left|\left|\sum_{k}\sum_{f(P)}\alpha^{k,f,n+1}\vartheta^{k,f,n}A^{f}\right|\right| \leq \varepsilon \tag{3.92}$$

This ensures that, regardless of the algorithm, global continuity is satisfied to a given tolerance.

3.4.1 Two Identical Fluids

To validate the implementations, a two-fluid flow of two identical, inviscid fluids with equal velocities is simulated with an initially prescribed, varying volume fraction profile. Under these conditions, the two-fluid flow behaves as a single phase, and the volume fraction profile should be transported like a passive scalar. Both fluids are initialised with the same velocity, equal to the inlet velocity $u^0(x) = u^{in} = 1$ m s^{-1}. The volume fraction of the first phase is initialised as a step profile

$$\alpha^1(t=0) = \begin{cases} 0.9 & 0.25 \leq x \leq 0.5 \\ 0.1 & \text{otherwise} \end{cases} \tag{3.93}$$

and the volume fraction of the second phase is given by the constraint that both volume fractions add up to unity. Theoretically, the volume fraction is advected as a passive scalar, as

$$\frac{\partial \alpha^1}{\partial t} + u\frac{\partial \alpha^1}{\partial x} = 0 \tag{3.94}$$

This flow configuration is simulated using the semi- and fully-coupled algorithms, and compared against an analogous single phase simulation of passive scalar transport. The volume fraction and passive scalar profiles resulting from the simulations are compared with the theoretical results and are shown in *fig.* 3.2.

As can be seen, all numerical solutions show excellent agreement with each other. A Total Variation Diminishing (TVD) advection scheme is used to approximate the advection of the volume fractions and the passive scalar. Hence, the numerical diffusion in the simulated cases compared to the exact solution is to be expected.

In this case the simulation is reduced to a simple scalar advection problem, and the momentum and global continuity equations are satisfied by the initial conditions. Therefore, the semi-coupled algorithm is more computationally efficient than the fully-coupled algorithm.

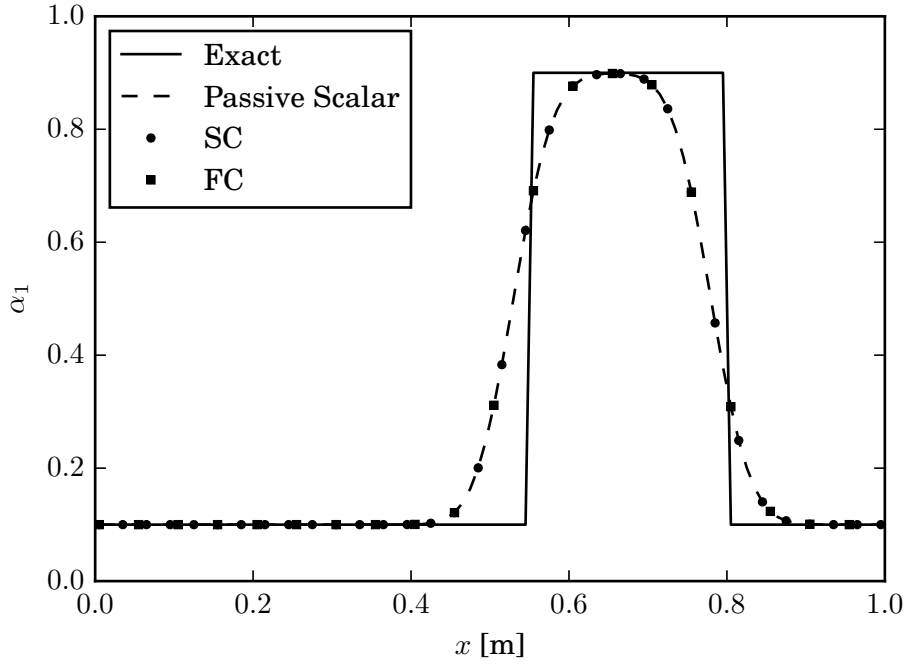

Figure 3.2: Comparison of volume fraction profiles obtained with the semi-coupled (circles) and fully-coupled (squares) algorithms with the analogous passive scalar solution (dashed line) for two identical fluids with equal velocity. The exact solution is shown by solid line.

It is found that for the semi-coupled algorithm to succeed, the solution of the volume fraction equations should precede the solution of the system of the pressure-velocity equations. When the solutions of the volume fractions are determined first, the momentum equation reduces to

$$\rho^k \alpha^{k,n+1} \left(\frac{\partial u^{k,n+1}}{\partial t} + u^{k,n} \frac{\partial u^{k,n+1}}{\partial x} \right) = 0 \tag{3.95}$$

Because α_k^{n+1} already satisfies continuity, the solution for the velocity becomes trivial: $u^{k,n+1} = u^{k,n} = u^O$. If the order of solving the two sets of equations in the semi-coupled algorithm is reversed, the algorithm becomes significantly more expensive.

3.4.2 Horizontal Two-Phase Flow

This test case considers a two-phase, horizontal, one-dimensional flow with a finite slip velocity between the two phases at the inlet. It is seen from the global continuity equation, Eq. (3.6),

that for a one-dimensional flow

$$u^m = \sum_k \alpha^k u^k = const = \sum_k \alpha^{k,in} u^{k,in} \tag{3.96}$$

where the mixture velocity, u^m, is determined by the conditions specified at the inlet. In the absence of external forces, the inter-phase momentum exchange between the two phases acts to reduce the relative velocity of the phases. As a result, both velocities eventually reach the same equilibrium velocity, $u^{eq} = u^m$ as given by Eq. (3.96).

Various cases of horizontal two-phase flows are simulated, for each case using both the semi- and fully-coupled algorithms. In the cases, the particle Reynolds number is varied in the range of $1 \leq Re_p \leq 1000$, using the relative velocity at the inlet as the reference slip velocity, and varying the gas phase viscosity to obtain the desired value of Re_p. The constant properties of both phases used in the simulations are given in table 3.3.

Table 3.3: Conditions of the horizontal flow case.

Property	**Continuous Phase**	**Dispersed Phase**
ρ [kg m^{-3}]	1.0	100.0
μ [Pa s]	$5 \times 10^{-5} \leq \mu_g \leq 5 \times 10^{-8}$	–
d [m]	–	10^{-4}
u^{in} [m s^{-1}]	1.0	0.5
α^{in} [-]	0.9	0.1

Using the values of u^{in} and α^{in} given in Table 3.3, the predicted equilibrium velocity is $u_{eq} = 0.95$ m s^{-1}. Prior to comparing the computational cost between the semi- and fully-coupled algorithms, the flow is simulated at each particle Reynolds number to determine the required domain size and required physical time to achieve a steady-state solution. These values are presented in table 3.4.

Table 3.4: Domain lengths and simulated times for horizontal flow case.

Re_p	L [m]	t_{sim} [s]
1	6.0×10^{-2}	1.5×10^{-2}
10	6.0×10^{-1}	1.5×10^{-1}
100	6.0	1.5
1000	60.0	15.0

The simulated velocity profiles for the two phases using the semi- and fully-coupled algorithms

for a particle Reynolds number of 100 are shown in *fig.* 3.3. As can be seen from the figure, both the semi- and fully-coupled algorithms show excellent agreement with each other and reach the correct equilibrium velocity. All simulations carried out for the various particle Reynolds numbers show an equally good comparison between the two algorithms and correctly predict the correct equilibrium velocity.

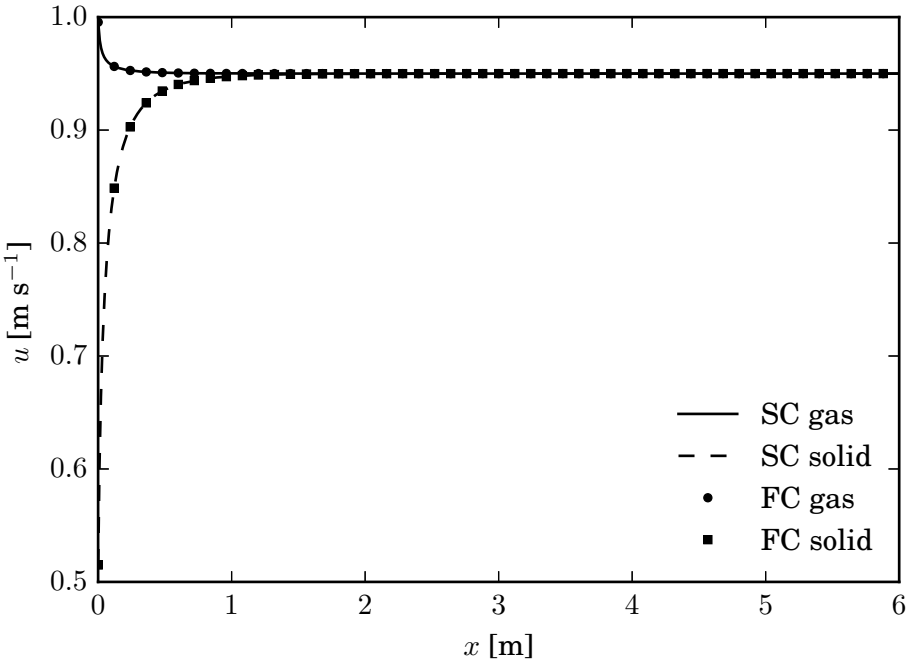

Figure 3.3: The velocity profiles for the gas and solid phases obtained with semi- and fully-coupled algorithms for $Re^p = 100$. *SC* shows the results obtained from the semi-coupled algorithm, and *FC* from the fully-coupled algorithm.

Both algorithms also show to be stable up to very high time-steps, for CFL numbers well over 1,000, demonstrating the robustness of the implicit treatment of the pressure gradient and inter-phase momentum exchange. To quantify the relative computational performance of the semi- and fully-coupled algorithms, time-accurate solutions are sought for the horizontal flow problem using a time-step determined by $CFL = 0.5$ based on the inlet velocity of the gas phase. The test case presented in the previous section, §3.4.1, shows that the order of solving the set of pressure-velocity equations and the transport of volume fractions can have a significant impact on the efficiency of the semi-coupled algorithm.

To investigate the impact of the sequence for the semi-coupled algorithm, the results of two computations using the semi-coupled algorithm are presented: one with the solution of

the transport equation of the volume fraction preceding the solution of the pressure-velocity equation system, and one with the reversed order, as originally proposed in this chapter, see algorithm 1.

Similarly, two computations using the fully-coupled algorithm are presented. The first one applies the conservative formulation of the momentum equations. The second computation applies the modified discretisation to increase the diagonal dominance of the linearisation matrix, as discussed in §3.3.2.4. The normalised computational time reported to simulate the horizontal two-phase flow, using a grid consisting of 5000 cells and 4 CPUs are plotted in *fig.* 3.4 for the various particle Reynolds numbers. The normalisation is done by the initial semi-coupled algorithm.

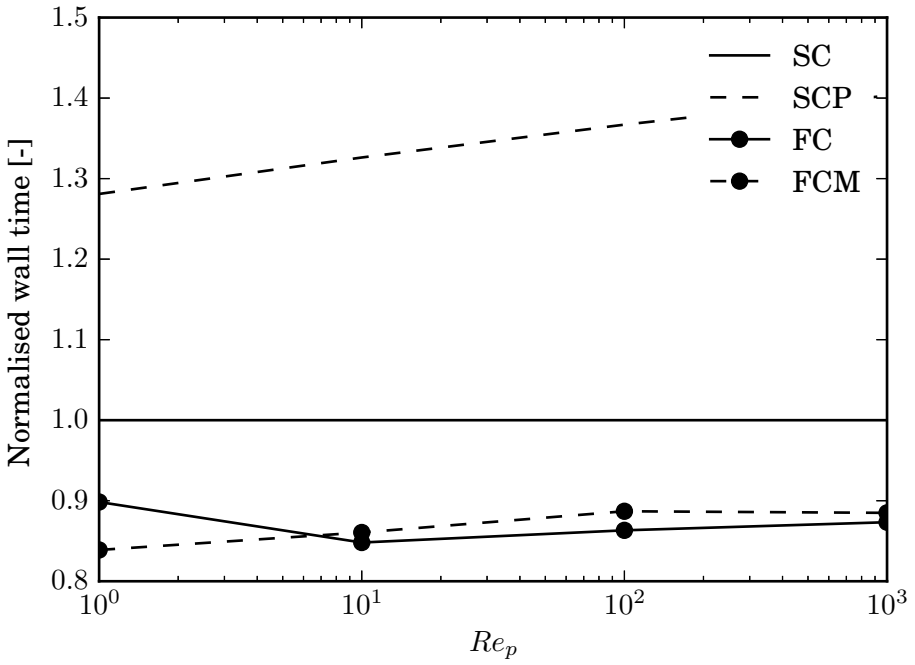

Figure 3.4: Normalised computational time to simulate the horizontal two-phase flow as a function of particle Reynolds numbers,Re^p, using the two variations of the semi-coupled and two variations of the fully-coupled algorithms, normalised by the wall time for the semi-coupled algorithm. semi-coupled timings are indicated by lines without markers and the fully-coupled algorithm timings by the lines with circular markers. SC denotes the semi-coupled algorithm, SCP denotes the semi-coupled algorithm with the volume fraction solution preceding the pressure-velocity solution, FC denotes the fully-coupled algorithms and FCM denotes the fully-coupled algorithm with the modification to improve diagonal dominance of the matrix (§3.3.2.4).

It can be clearly seen that both variations of the fully-coupled algorithm are more efficient

than the semi-coupled algorithm. The two variants of the fully-coupled algorithm presented do not show significant performance benefits over each other, due to the simplicity of the case, as no area of very low or high volume fraction occurs.

Figure 3.4 shows that the variation of the semi-coupled algorithm solving the phase continuity equation prior to the pressure-velocity problem incurs a significant time penalty due to the need to solve the volume fraction equation at least twice. In more complex flows, where multiple non-linear iterations are required to reach convergence, this expense should become less significant. Therefore it is recommended that the suggested modification to the semi-coupled algorithm be retained.

3.4.3 Vertical Two-Phase Flow

Many gas-solid flows of interest involve the flow of gas acting against the weight of particles. A vertical, two-phase gas-solid flow case is considered in which the gravity acts opposite to the direction of flow. In a one-dimensional case, when steady-state is reached, a constant slip velocity is observed between the two phases, given by the simplified momentum equation

$$0 = -\alpha^k \frac{\partial p}{\partial x_j} + \alpha^k \rho^k g_j + \beta \left(u_j^{l \neq k} - u_j^k \right) \tag{3.97}$$

From this equation, the slip velocity can be determined. The above equation is multiplied by $\alpha^{l \neq k}$ and subtracted from the equivalent equation for the other phase, phase $l \neq k$. The slip velocity is then given by

$$u_j^{l \neq k} - u_j^k = \frac{\alpha^k \alpha^{l \neq k}}{\beta} \left(\rho^{l \neq k} - \rho^k \right) g_j \tag{3.98}$$

To simplify this expression, the inter-phase momentum exchange coefficient is rewritten as

$$\beta = \alpha^k \alpha^{l \neq k} B^{kl} \tag{3.99}$$

so that the slip velocity can be expressed as

$$u_j^{l \neq k} - u_j^k = \frac{1}{B^{kl}} \left(\rho^{l \neq k} - \rho^k \right) g_j \tag{3.100}$$

In order to make an algebraic prediction of the terminal velocity, a simplification for the

inter-phase momentum exchange coefficient is made, and it is simplified to

$$\beta = \alpha^s(1-\alpha^s)\rho_f \frac{3}{4}\frac{|u^s - u^g|\, C^D}{d^p} \tag{3.101}$$

and the drag coefficient is fixed to $C^D = 0.44$. These assumptions make it possible to express the terminal slip velocity between the two phases as

$$u^t = u^{l\neq k} - u^k = -\sqrt{\frac{4}{3}\frac{d^p}{0.44\rho^g}\left(\rho^k - \rho^{l\neq k}\right) g} \tag{3.102}$$

where $\rho^{l\neq k} \geq \rho^k$, and gravity acts in the opposite direction to the flow. Applying the fluid properties given in Table 3.3, predicts a terminal slip velocity of $u^t = 0.542$ m s^{-1}, corresponding to a particle Reynolds number of $Re^p = 5.42$. The domain size and simulated time required to reach a steady-state are determined by an initial simulation to be 0.15 m and 0.5 s, respectively. *fig.* 3.5 shows the results of the slip velocity predicted by the semi- and fully-coupled algorithms. Also, the terminal velocity predicted by Eq. (3.102) is shown in the figure.

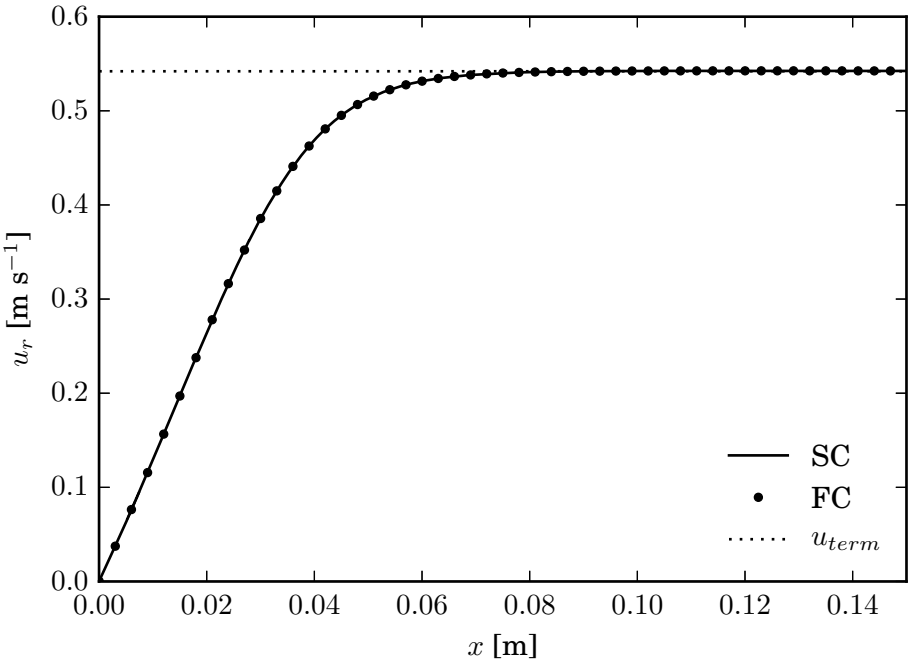

Figure 3.5: The slip velocity profiles for the vertical two-phase flow case. The semi- and fully-coupled solutions are indicated by the solid line and circular markers, respectively, and the dotted line indicates the theoretical terminal velocity.

As *fig.* 3.5 shows, both algorithms correctly predict the terminal slip velocity for this case,

and correctly reach the theoretical value. Moreover, both the semi- and fully-coupled algorithms are in very good agreement. The total computational time to reach steady state for the semi- and fully-coupled algorithms for a computational grid of 5000 cells on 4 CPUs are 7494.2 s and 8166.1 s, respectively. The time presented for the semi-coupled algorithm is based on the more efficient variant of solving the transport equation for the volume fraction after the pressure-velocity equation set, as discussed previously.

3.4.4 Fluidised Bed

A fluidised bed is a reactor which is used when a reaction between two different phases is desirable. Due to the optimal mixing and large contact area between the two phases, high rates of heat and mass transfer [58] can be achieved. Under bubbling conditions [58], the flow in such a device can be split into two regions: the bed region where most of the particles are located with high volume fractions, leading to long duration frictional contacts; and above the bed, the free-board is nominally free of particles. Simulations of a fluidised bed provide a very good opportunity for the algorithms developed in this work, as it concerns a two-phase flow with both dilute as well as dense regions, strong inter-phase momentum exchange, and has large source terms and gradients of source terms due to presence of a solids pressure term in the dense regions [88].

The fluidised bed considered in this work is 0.4 m in width and 0.6 m high. The properties of the phases used in the simulations are provided in table 3.5. These are the same properties and fluidised bed geometry as previously simulated by van Wachem *et al.* [87].

Table 3.5: Properties of the phases used in the fluidised bed test case.

Variable	Value
Solid phase maximum packing fraction $\alpha^{s,MAX}$ [-]	0.61
Frictional stress "kick-in" fraction $\alpha^{s,MIN}$ [-]	0.5
Frictional stress model empirical constant, Fr [Pa]	0.05
Frictional stress model empirical constant, n [-]	2
Frictional stress model empirical constant, p [-]	5
Inlet superficial gas velocity $u^{g,in}$ [m s^{-1}]	1.0
Gas density ρ^g [kg m^{-3}]	1.28
Solids density ρ^s [kg m^{-3}]	2600.0
Gas viscosity μ^g [Pa s]	1.7×10^{-5}
Particle diameter d^p [m]	500.0×10^{-6}
Particle coefficient of restitution e^s [-]	0.6

The initial bed height is set to 0.4 m, with a solids phase volume fraction of 0.21. A potential issue in simulating fluidised beds is that the solids phase volume fraction becomes zero in the free-board. To prevent this, the solids volume fraction is set to 1.0×10^{-6} initially in the free-board as well as at the outlet of the fluidised bed during the simulation [87, 89]. The usual outlet boundary conditions are set at the outlet of the fluidised bed, assuming fully-developed flow and ambient pressure. The boundary conditions for the side-walls of the fluidised bed are no-slip for the fluid phase, free-slip for the particle phase, and a zero-gradient for the granular temperature. At the inlet of the fluidised bed, a superficial gas velocity of 1.0 m s^{-1} is given, a zero normal velocity for the particles is given, and a zero gradient for granular temperature is set. The superficial velocity is around four times the minimum fluidisation velocity for the particles, which is the same as one of the cases discussed in van Wachem *et al.* [87].

The fluidised bed is simulated for a physical time of 2 s and instantaneous snapshots of solid phase volume fraction are shown in *fig.* 3.6 for the simulation results from the semi- and fully-coupled algorithms.

The snapshots of the volume fraction fields shows that the comparison between the semi- and fully-coupled algorithms produces very similar results up to about 1 s of real time. After this, the actual time-dependent volume fraction fields start to diverge from each other, due to the highly non-linear nature of the two-fluid model in combination with the KTGF closures. Since small round-off errors are introduced in the results at every time-step, the actual time-dependent results between two simulations start to diverge. However, the statistics predicted by the two algorithms, in terms of bubble size, bed expansion and pressure drop are very similar. These results are in terms of bed expansion and pressure drop, and are compared to the earlier findings with a fully segregated algorithm as published by van Wachem *et al.* [87].

For a given setup of fluidised bed, the pressure drop is very approximately the weight of the particles in the bed as [58]

$$\Delta p^{bed} A^{bed} = \alpha^s \rho^g \left(\rho^s - \rho^g\right) g V^{bed} \tag{3.103}$$

where Δp_{bed} is the pressure drop, A_{bed} the area of the bed, g the gravity vector and V_{bed} is the total volume of the bed at minimum fluidisation conditions.

The pressure drop in the simulations is determined by time-averaging the results between

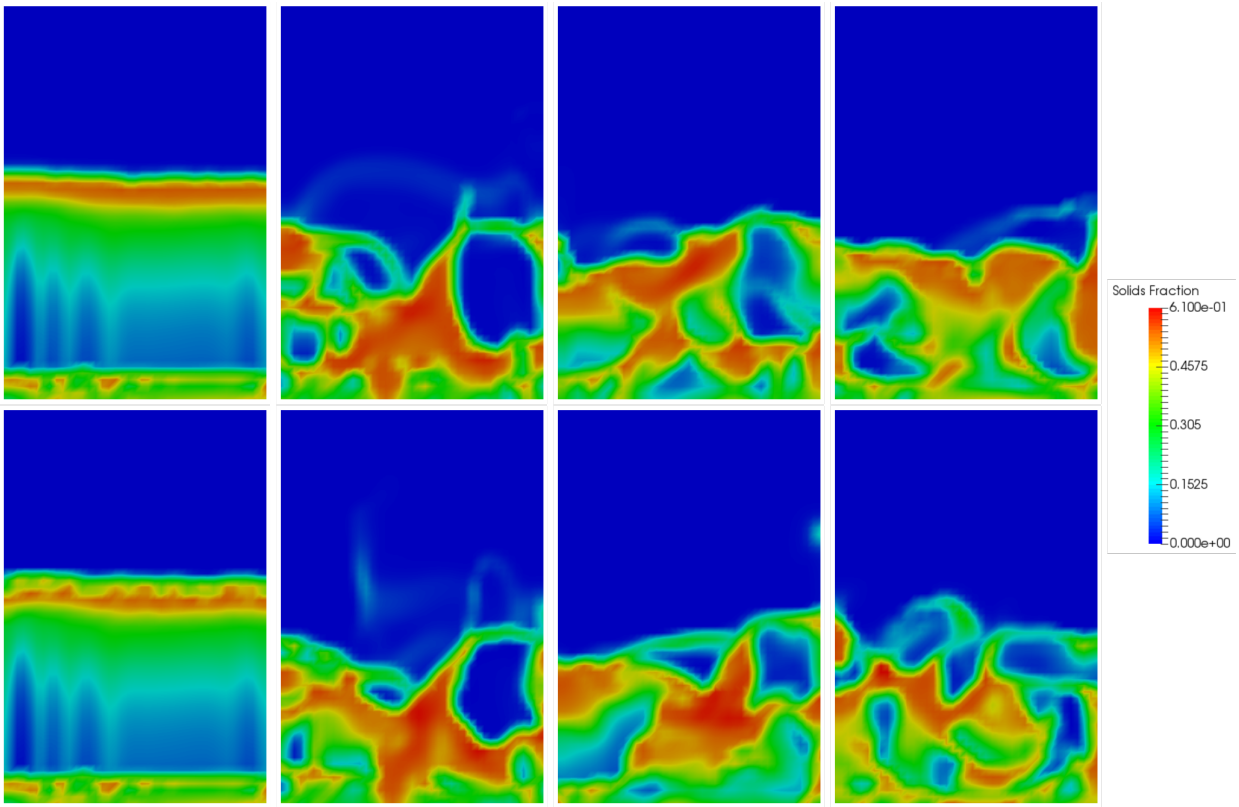

Figure 3.6: Comparison of snapshots of volume fraction fields in a fluidised bed simulation obtained using the semi- and fully-coupled algorithms, shown on the top and bottom rows, respectively. The meaning of the colours is indicated in the legend on the right. Times of snapshot are, from left to right: $t = 0.5$ s, $t = 1.0$ s, $t = 1.5$ s and $t = 2.0$ s.

1.0 and 2.0 s. The comparison of the pressure drop is presented in table 3.6.

Table 3.6: Fluidised bed pressure drop

	Pressure drop [Pa]
$\Delta p^{an.}$	≈ 2600
Δp^{SC}	2291
Δp^{FC}	2215

The prediction of the pressure drop between the two algorithms is very good. The small discrepancy between the analytical pressure drop and the simulated one is attributed to the approximate nature of the analytic expression, as also discussed in [58, 87]. The general dynamics and prediction of both algorithms agree very well with the results of van Wachem *et al.* [87].

To simulate this case, the semi- and fully-coupled algorithms required $37,487$ s and $27,837$ s of wall time, respectively, to simulate 2 s of flow on a 16 core compute node. The relative errors in mass, summing the absolute error for every time-step, for the semi- and fully-coupled

algorithms are 0.186% and 0.152%, respectively.

As expected, the fully-coupled algorithm is computationally a lot more effective for two-phase flow simulations in which the inter-phase coupling is significant and the source terms are appreciable.

3.5 Conclusions

A new framework for discretising and solving the two-fluid model for predicting the behaviour of two-phase flows has been derived and validated in this chapter. In the discretisation of the two-fluid model, both a Picard linearisation and a Newton linearisation have been pursued, leading to the semi-coupled and the fully-coupled algorithms.

In the semi-coupled algorithm, the discretisaton and Picard linearisation lead to a separate pressure-velocity equation system and a separate equation system for the transport of the volume fractions. It is shown that it is beneficial for most cases to solve the pressure-velocity system prior to solving the transport of the volume fractions.

In the fully-coupled algorithm, the discretisation and Newton linearisation lead to a single linearised system of equations for the complete two-fluid model. All the inter-phase coupling terms and linearised source terms are included in this system. Although this system is more expensive to solve per iteration, the increased coupling between the equations and robustness are expected to lead to significantly less required number of iterations per time-step. In this work also strategies are introduced to enforce a diagonally dominant discretisation matrix and boundedness of the volume fractions. This makes the solving of the system possible by any Krylov sub-space method.

The two approaches of the newly proposed framework are validated and verified by application to a range of test cases. These test cases involve horizontal two-phase flow, vertical two-phase flow and a more realistic test case of a bubbling fluidised bed. The horizontal and vertical two-phase flow cases are relatively simple, and both approaches of the framework perform very well and show good results compared to theory. There is very little difference in computational effort to reach steady-state for these two cases.

The two-phase flow simulations of the fluidised bed also show good results in comparison with the expected pressure drop and earlier predictions of van Wachem *et al.* [87]. Because this

case involves a strong inter-phase coupling, as well as a strongly varying source term, *i.e.* the solids pressure, the fully-coupled algorithm is computationally significantly more efficient than the semi-coupled algorithm. The simulation results of the semi- and fully-coupled approaches show a very good agreement with each other.

Chapter 4

Modelling Turbulent Two-Fluid Flows

In this chapter the fully-coupled algorithm developed in chapter 3 is further tested by application to turbulent gas-solid flows. The ensemble averaged two-fluid model, suitable for turbulent gas-solid flows is derived and used to simulate turbulent gas-solid flows in a backward facing step and in a bluff body flow.

4.1 Introduction

Gas-solid flows, a subset of the wider class of dispersed multiphase flows, consists of particles transported by a carrier fluid. Examples of such flows can be found in a range of environmental, industrial and scientific applications: from pollutant dispersal to power generation and fundamental studies of the interaction between the discrete particles and the carrier fluid. Flows of practical interest are frequently turbulent, and this is equally true of gas-solid flows in which the presence of particles plays a significant role in the overall behaviour of the flow. The particles in such flows may either enhance or attenuate the fluid turbulence, in a process known as turbulence modulation [3, 18]. Additionally, particles themselves are generally in fluctuating motion relative to a mean particle velocity field. This resembles the behaviour of molecules, which can be exploited in developing models to describe the behaviour of solid particles [61, 82]. As the fluctuating velocity fields of the fluid and particles interact, the work done by the fluctuating drag forces between the phases results in the transfer of fluctuating kinetic energy, giving rise to

the turbulence modulation observed in gas-solid flows. Capturing this effect is therefore vital to accurate modelling of turbulent gas-solid flows.

The wide range of length scales involved in turbulence and dispersed gas-solid flows makes exact Direct Numerical Simulation (DNS) computationally extremely demanding, as the behaviour of the smallest scales impacts the largest. Frequently, it is the large scale properties of the flow that are of practical interest, for example the pressure drop across a device, mixing rates or the rate of erosion due to particle collisions with the walls that guide the design process. This has lead to the development of methods based on averaging procedures, resolving behaviours occurring on scales that are large, and applying a model to account for the smaller scales. The smaller scales thus no longer need to be resolved, but are modelled. In so doing, the resolution required to simulate a given problem is significantly reduced, making the problem tractable given finite or limited computing resources at the expense of greater up front modelling cost.

In this work, the two-fluid framework [2, 48] is used to approximate the behaviour of turbulent gas-solid flows. The two-fluid model is based on an averaged description of a multiphase flow, resulting in each phase appearing as a continuous fluid occupying the entire domain, interpenetrating and interacting with the other phase by the application of coupling terms. The resulting system of non-linear equations bears similarity to that of single phase flows, consisting of transport equations describing the conservation of momentum, mass *etc.* however, is at least twice as large (at least 8 coupled equations for two phases), necessitating the use of efficient solution algorithms. This is used to test the fully-coupled algorithm developed in chapter 3 for solving the two-fluid model equations in application to flows representative of real world applications.

This chapter is organised as follows: in §4.2, the two-fluid model is presented and the averaged form derived. The fully-coupled algorithm used to solve the two-fluid model equation system is presented in §4.3 and evaluated by application to two test cases in §4.4: the backwards-facing step experiment of Fessler and Eaton [40], used as a validation study by Benavides and van Wachem [8]; and the bluff-body experiment performed by Boree *et al.* [10]. The chapter is concluded in §4.5.

4.2 The Two-Fluid Model

The two-fluid model [2, 47] is a computationally efficient framework for simulating multiphase flows. By describing the flow in terms of volume averages, each phase appears as a continuous fluid occupying the entire domain, interpenetrating and interacting with the other. As a result, the conservation of mass, momentum, *etc.* in each phase may be represented by a general transport equation of the form

$$\frac{\partial \alpha^k \rho^k \phi^k}{\partial t} + \frac{\partial \alpha^k \rho^k \phi^k u_i^k}{\partial x_i} = -\frac{\partial \alpha^k J_i^{\phi^k}}{\partial x_i} + \alpha^k S^{\phi^k} + \sum_{l \neq k} I^{\phi^{kl}} \ , \tag{4.1}$$

where ϕ is the transported variable, ρ is density, $I^{\phi^{kl}}$ is the exchange term describing interphase transfers, $\mathbf{J}^{\phi^k}$ is the diffusion flux, S^{ϕ^k} is the source term, t is time, $\mathbf{u}$ the velocity vector and $\mathbf{x}$ the Cartesian coordinate axis. Subscript i is a vector index, where Einstein summation is implied, and superscripts k and l are phase counters, indicating a variable is associated with a given phase *e.g.* $\mathbf{u}^g$ is the gas phase velocity whilst ρ^s is the solid phase density. Throughout this work, unless stated otherwise, subscript Latin characters represent vector indices and superscript Latin characters are used as phase counters. The additional variable, α^k, appearing in Equation Eq. (4.1) is the volume fraction of phase k, arising as part of the two-fluid model averaging procedure, and as the name suggests is the proportion of the averaging domain occupied by phase k.

Restricting the analysis to flows of phases with constant densities and neglecting mass transfer between phases, the continuity equation for each phase in the two-fluid model, also referred to as the transport equation for volume fraction, is given as

$$\frac{\partial \alpha^k}{\partial t} + \frac{\partial \alpha^k u_i^k}{\partial x_i} = 0 \ . \tag{4.2}$$

The volume fractions, by definition, are individually bounded between zero and one, and when summed over all the phases must sum to unity,

$$\sum_k \alpha^k = 1 \ , \tag{4.3}$$

which ensures that the total volume of the flow is conserved. A continuity equation for the

mixture, referred to as the global continuity equation, is obtained by summing the individual transport equations for volume fractions, Eq. (4.2), over all phases and applying the constraint that volume fractions sum to one, leading to

$$\sum_k \frac{\partial \alpha^k u_i^k}{\partial x_i} = 0 \ , \tag{4.4}$$

which is a statement of the conservation of volume and is the two-fluid model analogue of the incompressibility condition for single phase flows.

Under the same conditions of constant density phases and neglecting mass transfer between phases, the two-fluid model momentum equations are given as [47]:

$$\rho^k \frac{\partial \alpha^k u_j^k}{\partial t} + \rho^k \frac{\partial \alpha^k u_j^k u_i^k}{\partial x_i} = -\alpha^k \frac{\partial p}{\partial x_j} + \frac{\partial \alpha^k \tau_{ij}^k}{\partial x_i} - \frac{\partial p^k}{\partial x_j} + \alpha^k \rho^k g_j^k + I_j^{u^{kl}} \ , \tag{4.5}$$

where $\boldsymbol{\tau}$ is the shear stress tensor, $\mathbf{g}$ the external force vector, p is pressure and $\mathbf{I}^{u^{kl}}$ the momentum exchange term. In modelling gas-solid flows using the two-fluid model, the shared pressure p is taken equal to the gas phase pressure, consequently the phase specific pressure p^k is zero in the gas phase *i.e.* $p^g = 0$ whilst in the solid phase it is non-zero and describes the effect of particle-particle interactions [61].

Equations Eq. (4.2), Eq. (4.4) and Eq. (4.5) represent a single realisation of a multiphase flow. When the flow is turbulent, small variations in boundary or inlet conditions will result in a different observed flow, however statistically each flow is, on average, the same. Generally it is these mean flow statistics which are of interest, not the individual flow realisations. By averaging over an ensemble of flow realisations, each variable can be decomposed as

$$\phi = \overline{\phi} + \phi' \ , \tag{4.6}$$

where $\overline{\phi}$ is the mean value and ϕ' the fluctuation about the mean. The ensemble averaging

operator satisfies the following properties

$$\overline{\overline{\phi}} = \overline{\phi} \ , \tag{4.7a}$$

$$\overline{\phi'} = 0 \ , \tag{4.7b}$$

$$\overline{\overline{\phi}\psi'} = 0 \ , \tag{4.7c}$$

$$\overline{\phi'\psi'} \neq 0 \ , \tag{4.7d}$$

consequently, taking an ensemble average of the governing equations, the governing equations become transport equations for the ensemble mean values with additional turbulent transport terms due to the covariances of fluctuating values Eq. (4.7d). The computational requirements are thus reduced by resolving only the mean flow and accounting for the effects of turbulent fluctuations through the use of turbulence models [9].

It should be noted that standard ensemble averaging of the continuity equations introduces a covariance term, as [78]

$$\overline{\alpha^k u_i^k} = \overline{\alpha}^k \overline{u}_i^k + \overline{\alpha'^k u_i'^k} \ , \tag{4.8}$$

which requires modelling. Although this is possible [36], it is still unclear how to develop a unified approach to closing this term. However, this additional term can be avoided. To avoid introducing this additional term to the continuity equations, the Favré averaged velocity, weighted by volume fraction, is introduced [9]:

$$U_j^k = \frac{\overline{\alpha^k u_j^k}}{\overline{\alpha}^k} \ . \tag{4.9}$$

Following the definition of the Favré averaged velocity, the ensemble averaged phase continuity and global continuity equations of the two-fluid model are given as

$$\frac{\partial \overline{\alpha}^k}{\partial t} + \frac{\partial \overline{\alpha}^k U_i^k}{\partial x_i} = 0 \ , \tag{4.10}$$

and

$$\sum_k \frac{\partial \overline{\alpha}^k U_i^k}{\partial x_i} = 0 \ , \tag{4.11}$$

respectively.

When averaging the momentum equations, the ensemble average of the advection term, $\rho^k \boldsymbol{\nabla} \cdot \alpha^k \mathbf{u}^k \mathbf{u}^k$, gives rise to an analogy of the Reynolds stresses, due to the covariance of velocity fluctuations and an additional term due to velocity-volume fraction fluctuations:

$$\begin{aligned} \overline{\alpha^k u_j^k u_i^k} &= \overline{\alpha}^k U_j^k U_i^k + \overline{\alpha}^k \overline{u_j'^k u_i'^k} + \overline{\alpha'^k u_j'^k u_i'^k} \\ &= \overline{\alpha}^k U_j^k U_i^k - \frac{\overline{\alpha}^k}{\rho^k} \mathcal{R}_{ij}^k + \overline{\alpha'^k u_j'^k u_i'^k} \end{aligned} \quad . \tag{4.12}$$

The first term of Eq. (4.12) is identified as the mean advective transport of momentum, $\boldsymbol{\mathcal{R}}^k = -\rho^k \overline{\mathbf{u}'^k \mathbf{u}'^k}$ is the analogy of the Reynolds stress tensor and $\overline{\alpha'^k \mathbf{u}'^k \mathbf{u}'^k}$ is the triple covariance of velocity and volume fraction fluctuations. The ensemble averaged momentum equations then follow as

$$\begin{aligned} \rho^k \frac{\partial \overline{\alpha}^k U_j^k}{\partial t} + \rho^k \frac{\partial \overline{\alpha}^k U_j^k U_i^k}{\partial x_i} = &-\overline{\alpha}^k \frac{\partial \overline{p}}{\partial x_j} + \frac{\partial}{\partial x_i} \left(\overline{\alpha}^k \left(\mathcal{T}_{ij}^k + \mathcal{R}_{ij}^k \right) \right) - \frac{\partial \overline{p}^k}{\partial x_j} \\ &+ \overline{\alpha}^k \rho^k \overline{g_j}^k + \overline{I_j}^{u^{kl}} \end{aligned} \quad , \tag{4.13}$$

where the triple covariance of velocity and volume fraction fluctuations has been discarded [9].

To close Eq. (4.13), models are required for the fluctuating stress tensors of each phase, the solid phase stress tensor and the ensemble averaged momentum exchange term. These closures are presented in the following subsections.

4.2.1 The Fluid Phase

The ensemble averaged fluid phase momentum equations contains an analogy of the Reynolds stress tensor, which is given as

$$\mathcal{R}_{ij}^g = -\rho^g \overline{u_j'^g u_i'^g} \ , \tag{4.14}$$

representing momentum transport due to turbulent fluctuations. Using a Boussinesq approximation, the Reynolds stress tensor is modelled as

$$\mathcal{R}_{ij}^g = \mu^{g,t} \left(\frac{\partial U_j^g}{\partial x_i} + \frac{\partial U_i^g}{\partial x_j} \right) - \frac{2}{3} \left(\mu^{g,t} \frac{\partial U_k^g}{\partial x_k} + \rho^g k^g \right) \delta_{ij} \ , \tag{4.15}$$

where $\mu^{g,t}$ is the turbulent viscosity, δ_{ij} the Kronecker delta and k^g the kinetic energy of turbulent fluctuations, defined as

$$k^g = \frac{1}{2}\overline{u'^{g2}} \ . \tag{4.16}$$

The turbulent viscosity of each phase is given, based on a mixing length model, as

$$\mu^{g,t} \propto \rho^g l^{g,t} v^g \ , \tag{4.17}$$

where $l^{g,t}$ is a turbulent length scale and $v^g = \sqrt{k^g}$ a velocity scale.

A transport equation describing the evolution of the kinetic energy of turbulent fluctuations is obtained by subtracting the mean momentum equations, Eq. (4.13), from Eq. (4.5), forming the dot product with $\mathbf{u}^g$ and averaging, yielding an equation of the form [9]

$$\rho^g \frac{\partial \overline{\alpha}^g k^g}{\partial t} + \rho^g \frac{\partial \overline{\alpha}^g k^g U_i^g}{\partial x_i} = \underbrace{\frac{\partial}{\partial x_i}\left(\Gamma^g \frac{\partial k^g}{\partial x_i}\right)}_{\text{Diffusion}} + \underbrace{\mathcal{P}^g}_{\text{Production}} - \underbrace{\overline{\alpha}^g \varepsilon^g}_{\text{Dissipation}} + \underbrace{\overline{u_i'^g I_i'^{u^{gs}}}}_{\text{Exchange}} \ . \tag{4.18}$$

In the above equation, Γ^g is the diffusion coefficient modelling transport of turbulent kinetic energy by turbulent fluctuations [9], $\mathcal{P}^g$ is the production of turbulent fluctuations due to mean shear and ε^g is the dissipation of fluctuating kinetic energy, representing viscous dissipation as heat in the fluid phase and dissipation due to inelastic collisions in the solid phase. The final term, distinguishing Eq. (4.18) from the equivalent single phase equation, is the exchange of fluctuating kinetic energy between the fluid and solid phases as a result of work done by fluctuating drag forces. It is this term which gives rise to turbulence modulation observed in turbulent fluid-solid flows whereby the presence of particles may either enhance or attenuate the turbulence of the gas phase [3]. To complete the closure of the stress tensors, closures are required for the fluctuating kinetic energy equations and the turbulent viscosities of each phase.

4.2.1.1 Turbulent Viscosity

As shown above, the turbulent viscosity is a function of a length scale and a velocity scale. The velocity scale is given by $v^g = \sqrt{k^g}$ and is thus known by solving Eq. (4.18) for the fluid phase. In single phase turbulent flows, the length scale is given as $l^t = \dfrac{\sqrt{k^g}}{\varepsilon^g}$ [94], however this does not account for the presence of particles. Benavides *et al.* [9] argued that taking this model as

representative of the length scale of turbulence in the gas phase, a cube of dimension l^{t3} can be defined. In a gas-solid flow this cube contains N particles where, for particles of diameter d^p, N is given as

$$N = \overline{\alpha^s}\frac{l^{g3}}{V^p} = \overline{\alpha^s}\frac{6}{\pi {d^p}^3} l^{g3} \ . \tag{4.19}$$

Assuming the particles are evenly distributed within the volume, an effective length scale, constrained by the particles, follows as [9]

$$l^{g,t\prime} = l^{g,t} - N^{1/3} d^p = \left(1 - \left(\frac{6\overline{\alpha^s}}{\pi \alpha^{s,max}}\right)^{1/3}\right) l^{g,t} \propto \frac{\sqrt{k^{g3}}}{\varepsilon^g} \tag{4.20}$$

were the maximum packing limit, $\alpha^{s,max}$ is introduced to normalise the volume occupied by particles, suppressing the gas phase turbulence as this limit is approached [9]. The gas phase turbulent viscosity then follows as

$$\mu^{g,t} = c^\mu \rho^g \left(1 - \left(\frac{6\overline{\alpha^s}}{\pi \alpha^{s,max}}\right)^{1/3}\right)^{-1} \frac{k^{g2}}{\varepsilon^g} \ , \tag{4.21}$$

and is used to model the turbulent diffusion coefficient as $\Gamma^g = \mu^g + \dfrac{\mu^{g,t}}{\sigma^{g,k}}$. The model constants c^μ and $\sigma^{g,k}$ are given in table 4.1.

Table 4.1: Model constants for the two-fluid model RANS equations [8, 9]

c^μ	$c^{g,\varepsilon 1}$	$c^{g,\varepsilon 2}$	$c^{g,\varepsilon 3}$	$\sigma^{g,\varepsilon}$	$\sigma^{g,k}$	c^L	$\sigma^{s,\Theta}$
0.09	1.44	1.92	1.2	1.3	1.0	$\sqrt{\frac{3}{2}}c^\mu$	0.72

A potential issue with Eq. (4.21), occurs when $\overline{\alpha^s} \geq \dfrac{\pi}{6}\alpha^{s,max}$ leading to a zero or negative denominator, and consequently values asymptotically approaching plus or minus infinity respectively. Similar numerical issues are posed by the radial distribution function, given in table 3.2, when $\overline{\alpha^s} \geq \alpha^{s,max}$ and a similar treatment is applied for each. A point is chosen near the asymptote, for example $\overline{\alpha^s_0} = 0.99\dfrac{\pi}{6}\alpha^{s,max}$ in the case of the viscosity model given in Eq. (4.21), and for volume fractions exceeding this value, the viscosity/radial distribution function computed

by extrapolation, *e.g.*

$$\mu^{g,t} = \begin{cases} c^{\mu}\rho^{g}\left(1 - \left(\frac{6\overline{\alpha^{s}}}{\pi\alpha^{s,max}}\right)^{1/3}\right)^{-1}\frac{k^{g2}}{\varepsilon^{g}} , & \overline{\alpha^{s}} \leq \overline{\alpha_{0}^{s}} \\ \mu_{0}^{g,t} + \left(\overline{\alpha^{s}} - \overline{\alpha_{0}^{s}}\right)\frac{\partial\mu_{0}^{g,t}}{\partial\overline{\alpha^{s}}} , & \text{otherwise} \end{cases} \tag{4.22}$$

where

$$\mu_{0}^{g,t} = c^{\mu}\rho^{g}\left(1 - \left(\frac{6\overline{\alpha_{0}^{s}}}{\pi\alpha^{s,max}}\right)^{1/3}\right)^{-1}\frac{k^{g2}}{\varepsilon^{g}} \tag{4.23}$$

is the viscosity evaluated near the asymptote.

The above extrapolation allows the computation to proceed when the solids phase volume fraction exceeds the safe ranges, in particular the use of extrapolation to compute g_0 for $\overline{\alpha^{s}} \geq \alpha^{s,max}$ ensures that its value, and hence the solids pressure continues to increase rapidly with increasing volume fraction. The model therefore does not prevent the solids phase volume fraction from exceeding $\alpha^{s,max}$ but where this does occur, the solids pressure computed is allowed in a physically realistic manner to exceed the surrounding values with the resulting solids pressure gradient forcing the solids into the neighbouring cells.

Finally, the dissipation of fluctuating kinetic energy in the gas phase is required. By analogy with Eq. (4.18), a model equation is given as

$$\begin{aligned} \rho^{g}\frac{\partial\overline{\alpha}^{g}\varepsilon^{g}}{\partial t} + \rho^{g}\frac{\partial\overline{\alpha}^{g}\varepsilon^{g}U_{i}^{g}}{\partial x_{i}} = \frac{\partial}{\partial x_{i}}\left(\overline{\alpha}^{g}\left(\mu^{g} + \frac{\mu^{t,g}}{\sigma^{g,\varepsilon}}\right)\frac{\partial\varepsilon^{g}}{\partial x_{i}}\right) + \left(c^{g,\varepsilon 1}\mathcal{P}^{g} - c^{g,\varepsilon 2}\overline{\alpha}^{g}\varepsilon^{g}\right)\frac{\varepsilon^{g}}{k^{g}} \\ + c^{g,\varepsilon 3}\overline{u_{i}'^{g}I_{i}'^{us g}}\frac{\varepsilon^{g}}{k^{g}} \end{aligned} , \tag{4.24}$$

where the additional model coefficients can be found in table 4.1.

4.2.2 The Solid Phase

The ensemble averaged equations of the solid phase are obtained from a probability density framework. In a fluid-solid flow, the probability of finding a particle at $\mathbf{x}$ with velocity $\mathbf{c}^{p}$ is given by the particle Probability Density Function (PDF), $f\left(\mathbf{x}, \mathbf{c}^{p}\right)$, obtained from an ensemble average [61, 82]. By analogy with the kinetic theory of gases, the Kinetic Theory of Granular Flows (KTGF) [61] develops the equations required to describe the solid phase as an Eulerian

fluid by assuming the particle PDF obeys the Boltzmann transport equation

$$\frac{\partial f}{\partial t} + c_i^p \frac{\partial f}{\partial x_i} = -a_i^p \frac{\partial f}{\partial c_i^p} + \left.\frac{\partial f}{\partial t}\right|_{coll.} \ , \tag{4.25}$$

where $\mathbf{a}^p$ is the particle acceleration and $\left.\frac{\partial f}{\partial t}\right|_{coll.}$ the particle PDF rate of change as a result of particle collisions. Using the particle PDF, a solid phase averaged variable is given by integrating over the particle phase space [82]

$$\langle \phi^p \rangle = \frac{1}{n^p} \int \phi^p f d\mathbf{c}^p \ , \tag{4.26}$$

where n^p is the particle number density. Multiplying Eq. (4.25) by ϕ^p and integrating, a phase averaged transport equation is obtained as

$$\frac{\partial n \langle \phi^p \rangle}{\partial t} + \frac{\partial n^p \langle \phi^p c_i^p \rangle}{\partial x_i} = n^p \left\langle a_i^p \frac{\phi^p}{c_i^p} \right\rangle + n^p \mathcal{C}^\phi \ , \tag{4.27}$$

where the final term is the collision operator $n^p \mathcal{C}^\phi = \int \phi^p \left.\frac{\partial f}{\partial t}\right|_{coll.} d\mathbf{c}^p$.

Setting $\phi^p = m^p,\ m^p \mathbf{c}^p$, and using the identities

$$n^p m^p = \alpha^s \rho^s \ , \tag{4.28}$$

and

$$\langle c_i^p \rangle = U_i^s \ , \tag{4.29}$$

the solid phase continuity equation is obtained as

$$\frac{\partial \alpha^s \rho^s}{\partial t} + \frac{\partial \alpha^s \rho^s U_i^s}{\partial x_i} = 0 \ , \tag{4.30}$$

and the solid phase momentum equations are given by

$$\frac{\partial \alpha^s \rho^s U_j^s}{\partial t} + \frac{\partial \alpha^s \rho^s U_j^s U_i^s}{\partial x_i} = \alpha^s \rho^s \left\langle a_j^p \right\rangle + \frac{\partial \alpha^s \mathcal{R}_{ij}^s}{\partial x_i} + \alpha^s \rho^s \mathcal{C}^{c_j^p} \ , \tag{4.31}$$

where the first term on the right hand side is due to the body forces working on the particles, the second term represents the kinetic stresses of the particulate phase, and the last term originates from particle-particle collisions. It is assumed that the particles do not breakup or agglomerate during collisions.

The kinetic stress [82] arises through the correlation term $\left\langle c_j^p c_i^p \right\rangle \approx U_j^s U_i^s - \frac{1}{\rho^s}\mathcal{R}_{ij}^s$. The collisional contribution to momentum gives rise to a collisional stress term which is approximated as

$$\alpha^s \rho^s \mathcal{C}^{c_j^p} = \frac{\partial \alpha^s \mathcal{T}_{ij}^s}{\partial x_i} - \frac{\partial p^s}{\partial x_j} \ , \tag{4.32}$$

and the external force term is given by taking the phase average of the particle equation of motion

$$\alpha^s \rho^s \left\langle a_j^p \right\rangle = -\alpha^s \frac{\partial p}{\partial x_j} + \alpha^s \rho^s g_j^s + I_j^{u^{sg}} \ . \tag{4.33}$$

Equations Eq. (4.30) and Eq. (4.31) can be further simplified by considering particles which all have the same, constant, density.

The solid phase kinetic stress tensor can be modelled using a Boussinesq approximation, as previously expressed in Eq. (4.15). The granular temperature, $\Theta^s = \frac{1}{3}\left\langle u'^{p2} \right\rangle$, is used as the measure of the particle fluctuations and is related to the fluctuating kinetic energy as $3\Theta^s = 2k^s$. The evolution of granular temperature is given by the transport equation

$$\frac{3}{2}\left(\rho^s \frac{\partial \overline{\alpha}^s \Theta^s}{\partial t} + \rho^s \frac{\partial \overline{\rho}^s \Theta^s U_i^s}{\partial x_i}\right) = \frac{\partial}{\partial x_i}\left(\kappa^s \frac{\partial \Theta^s}{\partial x_i}\right) + \mathcal{P}^s - \gamma^s + \overline{u_i'^s I_i'^{u^{sg}}} \ , \tag{4.34}$$

where κ^s is the granular conductivity, $\mathcal{P}^s$ is the production of granular temperature due to mean shear, γ^s the dissipation of granular temperature through inelastic collisions and the final term represents the interphase exchange of fluctuating kinetic energy due to work done by fluctuating drag forces.

The viscous stress tensor of the solid phase has two separate components, a kinetic component, $\mathcal{R}_{ij}^s$, and a collisional component $\mathcal{T}_{ij}^s$. This leads to an effective shear viscosity $\mu^s = \rho^s l^s \sqrt{\Theta^s}$ and a bulk viscosity $\lambda^s = \frac{4}{3}\rho^s d^p \overline{\alpha^s} g_0 \sqrt{\Theta^s}$. Closure models for the length scale are developed by arguments to kinetic theory [46, 61] but these do not account for the effect of the interstitial gas. Instead, in this work the model proposed by Benavides and van Wachem [8] is used. It is based on modelling the interaction of particles with turbulent eddies in the gas phase. Based on the

work of Csanady [19], Simonin [82], Simonin *et al.* [83], the turbulent scales as seen by a particle as it crosses a turbulent eddy scale are approximated as

$$\psi^{s,t} \propto \frac{\psi^{g,t}}{\sqrt{1 + c^{\beta}\xi^{r}}} \ , \tag{4.35}$$

where ξ^r accounts for the crossing-trajectory effect [8, 9] and is given as $\xi^r = \sqrt{\frac{3}{2}}\frac{|\mathbf{U}^r|}{\sqrt{k^g}}$. $\mathbf{U}^r$ is the averaged relative velocity between particles and the fluid [82]. The solid phase viscous length scale based on particle-eddy interactions then follows as [8]

$$l^B = \frac{c^L}{\sqrt{1 + c^{\beta}\xi^{r}}}\frac{\sqrt{k^{g3}}}{\varepsilon^g} \ . \tag{4.36}$$

The length scale should also be limited by the particle mean free path $l^{mfp} = \dfrac{d^p/\overline{\alpha}^s}{6\sqrt{2}}$ so that the solid phase length scale is given as [8]

$$l^s = \min\left(l^B, l^{mfp}\right) \ . \tag{4.37}$$

The granular conductivity follows as $\kappa^s = \overline{\alpha^s}\dfrac{\mu^s}{\sigma^{s,\Theta}}$ [8].

The model constants appearing in the solid phase equations can also be found in table 4.1. The outstanding closures required to describe the interphase interactions are presented below.

4.2.3 Momentum Exchange Closure

Before the Reynolds average of the momentum exchange can be taken, a model for the instantaneous exchange of momentum between the phases is required. When there is relative motion between an object and the surrounding fluid, a drag force is exerted upon the object, given by the expression

$$f_j^{drag} = \frac{1}{2}\rho^g \left|\Delta\mathbf{u}\right| \Delta u_j A C^D \ , \tag{4.38}$$

where A is the cross-sectional area perpendicular to the flow, C^D the drag coefficient and $\Delta\mathbf{u}$ the velocity of the object relative to the freestream velocity of the fluid. In addition to drag due to relative motion, lift forces caused by rotation and so-called added mass and history forces are also exerted upon particles carried by a fluid [63], however, considering the typically large solid

to gas density ratios, *e.g.* $\dfrac{\rho^s}{\rho^g} > 1000$, the drag force dominates momentum exchange between the phases [74]. Based on the hindered settling velocity approach developed by Richardson and Zaki [77] the drag force exerted upon a single particle is related to the drag force applied to a particle suspension as

$$I_j^{u^{sg}} = \epsilon\left(\alpha^s\right) f_j^{drag} = \beta\left(u_j^g - u_j^s\right) \ , \tag{4.39}$$

where $\epsilon\left(\alpha^s\right)$ is a function of the solid phase volume fraction and β is the momentum exchange coefficient, used to express the momentum exchange in terms of the relative velocity, emphasising that this term acts to couple the momentum equations together. In this work, the momentum exchange term is modelled using the model developed by Wen and Yu [95], valid for a range of flow conditions [89]. The velocity difference $\mathbf{\Delta u}$ appearing in Eq. (4.38) is given by the velocity of the object relative to the free-stream fluid velocity, the drag force exerted upon the carrier gas should therefore be given in terms of the undisturbed gas velocity, $\widehat{\mathbf{u}}^g$, so that

$$I_j^{u^{gs}} = \beta\left(u_j^s - \widehat{u}_j^g\right) \ , \tag{4.40}$$

and is equal and opposite to the drag force exerted upon the solids. The undisturbed and instantaneous gas velocities are related as

$$\widehat{u}_j^g = u_j^g + U_j^d \ , \tag{4.41}$$

and $\mathbf{U}^d$ is the so-called "*drift velocity*" [9]. The drift velocity results in a dispersive force acting upon the particles as they interact with the fluid turbulence and is modelled as

$$U_j^d = -\mathcal{D}^{sg}\left(\frac{1}{\overline{\alpha}^s}\frac{\partial\overline{\alpha}^s}{\partial x_j} - \frac{1}{\overline{\alpha}^g}\frac{\partial\overline{\alpha}^g}{\partial x_j}\right) \ , \tag{4.42}$$

where $\mathcal{D}^{sg}$ is a dispersion coefficient. The instantaneous drag force model is completed by specifying closures for the dispersion coefficient $\mathcal{D}^{sg}$ and the momentum exchange coefficient β, given in table 4.2.

As the model for β shows, the drag force model is a non-linear function of the velocities and volume fractions of the gas and solid phases, therefore Reynolds averaging the momentum exchange term directly would result in the introduction of multiple unclosed terms. A simplified

Table 4.2: Momentum exchange closure models

Model	Notes
$\mathcal{D}^{sg} = \frac{1}{3}k^{sg}\tau^{t,sg}$, $\tau^{t,sg} = \frac{\tau^{t,g}}{\sqrt{1+c^{\beta}\xi^{r}}}$, $\tau^{t,g} = c^{\mu}\frac{3k^{g}}{2\varepsilon^{g}}$	$\tau^{t,sg}$ and $\tau^{t,g}$ are the eddy-particle interaction and gas turbulent timescale respectively [6]
$c^{\beta} = 1.8 - 1.35\left(\frac{U_i^r U_i^s}{\lvert\mathbf{U}^r\rvert\,\lvert\mathbf{U}^s\rvert}\right)^2$, $\xi^r = \frac{3\mathbf{U}^{r2}}{2k^g}$, $U_i^r = (U_i^s - U_i^g) - U_i^d$	
$\beta = \alpha^s(1-\alpha^s)\frac{3}{4}\frac{\rho^g\lvert\Delta\mathbf{u}^{sg}\rvert}{(1-\alpha^s)^{2.65}d^p}C^D$	Wen and Yu [95] model
$C^D = \begin{cases}\frac{24}{(1-\alpha^s)Re^p}\left(1+0.15((1-\alpha^s)Re^p)^{0.687}\right) & \text{if } (1-\alpha^s)Re^p < 1000 \\ 0.44 & \text{otherwise}\end{cases}$	
$Re_p = \frac{\rho_g d_p\lvert\Delta\mathbf{u}_{gs}\rvert}{\mu_g}$	Particle Reynolds number

expression for the momentum exchange coefficient is therefore sought to avoid introducing additional unclosed terms before proceeding. Based on the approach of Hrenya and Sinclair [46] the momentum exchange coefficient is first rewritten as

$$\beta = \alpha^s F \ , \tag{4.43}$$

so that the instantaneous momentum exchange follows as

$$I_j^{u^{gs}} = \alpha^s F\left(u_j^s - \widehat{u}_j^g\right) \ . \tag{4.44}$$

Taking an ensemble average of Eq. (4.44) gives rise to additional unclosed terms. However, by taking the volume fraction outside the momentum exchange coefficient it can be shown that it gives rise to Favré averaged velocities. The remaining issue is therefore the decomposition and subsequent ensemble averaging of F which is itself a non-linear function of the solid phase volume fraction and the gas and solid phase velocities. Following the work of Hrenya and Sinclair [46], the decomposition of F is obtained by expanding F about the mean value in terms of velocity and volume fraction fluctuations, giving

$$F = \overline{F} + F' = \overline{F} + \alpha'^s\frac{\partial F}{\partial \alpha^s} + u_i'^s\frac{\partial F}{\partial u_i^s} + u_i'^g\frac{\partial F}{\partial u_i^g} \ , \tag{4.45}$$

where $\overline{F}$ is F evaluated using only mean values and F' is the fluctuation about this mean value.

For small particles, these fluctuations may be ignored [9, 46] so that $F \approx \overline{F}$ and as a result of this simplification the ensemble averaged momentum exchange term follows as

$$\begin{aligned}\overline{I_j^{u^{gs}}} = \overline{F}\overline{\alpha^s\left(u_j^s - \widehat{u}_j^g\right)} &= \overline{F}\left(\overline{\alpha}^s U_j^s - \overline{\alpha^s\left(u_j^g + U_j^d\right)}\right) \\ &= \overline{\beta}\left(\left(U_j^s - U_j^g - U_j^d\right) + \frac{\overline{\alpha'^g u_j'^g}}{\overline{\alpha}^g} - \frac{\overline{\alpha'^s u_j'^g}}{\overline{\alpha}^s}\right) ,\end{aligned} \tag{4.46}$$

where the final two terms may be discarded [9]. The ensemble averaged momentum exchange term is then finally given as

$$\overline{I_j^{u^{gs}}} = \overline{\beta} U_j^r , \tag{4.47}$$

where $\overline{\beta} = \overline{\alpha}^s \overline{F}$ is the mean momentum exchange coefficient.

The two-fluid model, with the closures presented above, is implemented in the research code `MultiFlow` [91] and solved using a fully-coupled algorithm, presented briefly in the next section.

4.3 Numerical Method

The equations describing the flow are discretised using FVM on a collocated mesh using momentum-weighted interpolation [76] and solved using the fully-coupled algorithm developed in chapter 3. The fully-coupled algorithm is based on an inexact Newton algorithm [26], treating the two-fluid model as a single, coupled system of equations, yielding superior stability in the presence of highly non-linear source terms and constitutive relations, as appear in the closure of the solid phase stress tensor. This results in a system of coupled equations of the form

$$\mathbf{J}\Delta\boldsymbol{\phi} = -\mathbf{F} , \tag{4.48}$$

where

$$\mathbf{J} = \begin{bmatrix} \mathbf{A}^g + \mathbf{D} & -\mathbf{D} & \mathbf{B}^g & -\mathbf{R}^g \\ -\mathbf{D} & \mathbf{A}^s + \mathbf{D} & \mathbf{B}^s & \mathbf{R}^s \\ \mathbf{H}^g & \mathbf{H}^s & \mathbf{G}^g + \mathbf{G}^s & -\mathbf{E}^g + \mathbf{E}^s \\ \mathbf{0} & \mathbf{H}^s & \mathbf{G}^s & \mathbf{E}^s \end{bmatrix} , \tag{4.49}$$

is the Jacobian,

$$\Delta\boldsymbol{\phi} = \begin{pmatrix} \Delta\mathbf{U}^g \\ \Delta\mathbf{U}^s \\ \Delta\overline{p} \\ \Delta\overline{\alpha}^s \end{pmatrix} , \tag{4.50}$$

is the update vector, and $\mathbf{F}$ is the non-linear residual function, for further details, including the definition of the coefficient matrices, see chapter 3. The fluctuating kinetic energy of both phases is updated separately from the coupled pressure-velocity-volume fraction system and used to calculate the transport coefficients for the next time-step.

4.4 Test Cases and Results

The ensemble and Favré averaged two-fluid model, with the closures presented in §4.2 and solved using the fully-coupled algorithm described in §4.3 is evaluated using two comprehensive and challenging test cases. The first is a vertical particle-laden flow over a backward facing step, based on the experimental data of Fessler and Eaton [40], and simulated previously by Benavides and van Wachem [8]; used here as a validation case. The second case investigated is the particle-laden bluff body flow studied experimentally by Boree *et al.* [10].

The initial conditions and inlet and outlet boundary conditions are specific for each case. However, the boundary conditions applied at the solid walls are the same for both cases. For the fluid phase, it is assumed that the standard wall functions for the $k-\varepsilon$ model are unaffected by the presence of particles. The boundary conditions for the fluid phase at solid walls are given as

$$\tau^{g,w} = \rho^g c^{\mu^{1/4}} \sqrt{k^{g,P}} \frac{\mathcal{U}^{g,P}}{u^+} , \tag{4.51}$$

$$\left.\frac{\partial k^g}{\partial n}\right|^w = 0 , \tag{4.52}$$

and

$$\varepsilon^{g,P} = \frac{c^{\mu^{3/4}} \sqrt{k^{g,P^3}}}{\kappa \Delta y} , \tag{4.53}$$

where $\tau^{g,w}$ is the shear stress acting at the wall, $\mathcal{U}^{g,P}$ is the velocity at cell P tangential to the

wall, u^+ is the tangential velocity in wall units and Δy is the wall-normal distance to cell P.

As a first approximation, free slip boundary conditions are applied at the walls for the solid phase and the normal gradients of granular temperature set to zero. The normal gradients of volume fraction, granular and fluid pressure are set to zero at the walls, except when the wall normal is parallel to the gravity vector in which case the fluid pressure at the wall is extrapolated from the interior of the domain.

4.4.1 Backward Facing Step

The model implementation as described in this chapter is validated against the experimental data of Fessler and Eaton [40] for downwards particle-laden flow over a backwards facing step. The domain consists of an inlet section of height $h = 40$ mm extending $65h$ upwind of the step, and an outlet section extending $34H$ downwind of the step where $H = 26.7$ mm is the step height, as illustrated in *fig.* 4.1. The coordinate origin is located at the base of the step and the x axis aligned with the gravity vector.

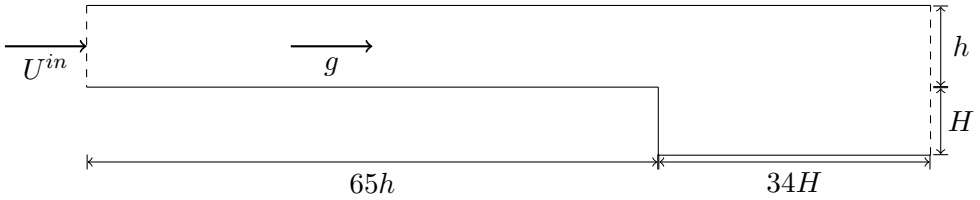

Figure 4.1: Diagram of the backward facing step domain.

Four different flow cases are considered: a single phase flow case, presented in §4.4.1.2, and three gas-solid flow cases, presented in §4.4.1.3. The phase properties are given in table 4.3 and the boundary and initial conditions in §4.4.1.1.

Table 4.3: Backward facing step phase properties

Quantity		Value
ρ^g	[kg m^3]	1.19
ρ^s	[kg m^{-3}]	2500 (case 1) 2500 (case 2) 8800 (case 3)
μ^g	[Pa s]	1.81×10^{-5}
d^p	[μm]	150 (case 1) 90 (case 2) 70 (case 3)
e^s	[-]	0.9

4.4.1.1 Boundary and Initial Conditions

The velocities of both phases, the turbulent kinetic energy and dissipation of the fluid phase and the granular temperature of the solid phase are initialised with uniform fields given by the inlet values, whilst the shared pressure field is uniformly zero initially. The volume fraction field is initialised based on the inlet value above the step ($\alpha^{s,0}\left(y > H\right) = \alpha_s^{in}$) whilst behind the step, a lower initial value ($\alpha^{s,0}\left(y < H\right) = 10^{-5}$) is specified.

Uniform values are specified at the inlet boundary. The fluid inlet velocity is set to $U^{g,in} = 9.3$ m s^{-1} to obtain a centreline velocity of $U^{g,cl} \approx 10.5$ m s^{-1} at the step. The inlet velocity for the solid phase is specified at the inlet based on the particle Reynolds number for each case, given in table 4.4, and the volume fraction determined by satisfying the mass-loading for the case where the mass-loading, $\mathcal{ML}$ is defined as

$$\mathcal{ML} = \frac{\overline{\alpha}^{s,in}\rho^s U^{s,in}}{\left(1-\overline{\alpha}^{s,in}\right)\rho^g U^{g,in}} \ . \tag{4.54}$$

The inlet boundary conditions for the turbulent kinetic energy and granular temperature are given based on a turbulence intensity of $I^t = 1\%$ in both phases, and the dissipation of turbulent kinetic energy defined based on a boundary layer thickness $\delta = \frac{1}{2}h$ and setting the turbulent length scale as

$$l^{g,t} = \frac{k^{g,in}}{\varepsilon^{g,in}} = 0.1\delta \ . \tag{4.55}$$

A fully developed boundary condition is applied at the outlet of the domain with zero normal gradients for all variables except pressure which is fixed at $\overline{p}^{\text{out}} = 0$ Pa.

To allow sufficient time for a steady flow to develop, each flow is simulated for $T = 2.85$ s, corresponding to 10 flow-throughs for the fluid phase based on the inlet velocity. The setup is first validated by simulating a single phase flow, presented in §4.4.1.2, and then simulations of particle-laden flows are presented in §4.4.1.3.

4.4.1.2 Single Phase Flow

To validate the setup of the case, the numerical results are compared against experimental data for single phase flow at several stations downstream of the step. Figure 4.2 shows the streamwise velocity profiles at several stations downstream of the step, normalised by the channel centreline

velocity measured at the step ($x = 0$).

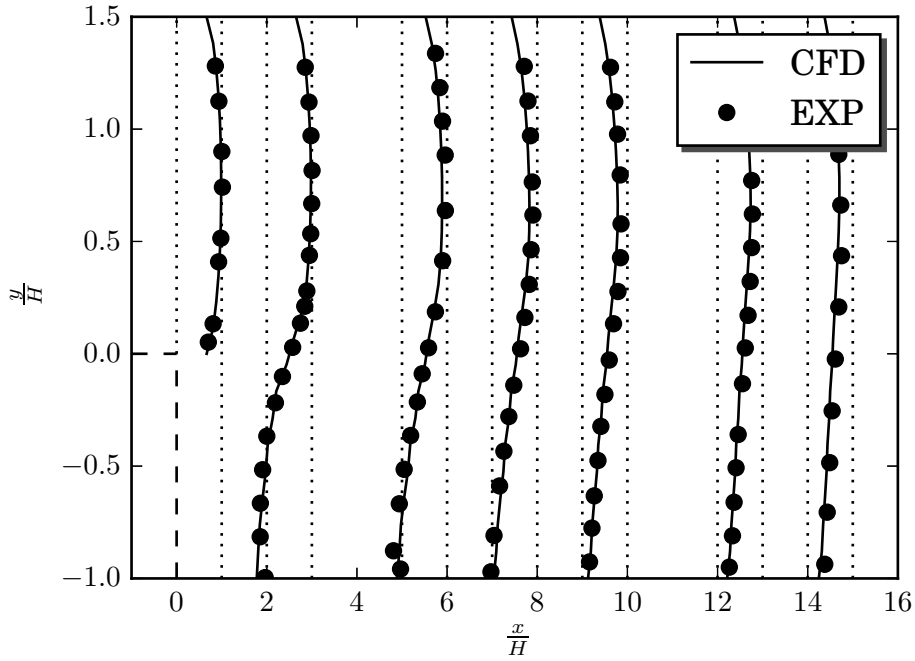

Figure 4.2: Comparison of stream-wise velocity profiles, normalised by $U^{g,cl}$. Experimental data is plotted as points, whilst numerical results are shown as solid lines. Dotted lines indicate the bounds of normalised velocity between zero and one at each station and the step is shown by dashed lines with the corner located at $(0, 0)$.

Comparison of the numerical results with the experimental data shows good agreement between both at all measurement positions. In particular, the recirculation region is well captured and the length of the recirculation region $l_{recirc.} \approx 7H$ is well predicted. Based on this comparison, the mesh is sufficiently refined to capture the essential flow physics and this setup is used to simulate the particle-laden flows.

4.4.1.3 Particle-Laden Flow

Simulations are performed for flows of three different particle types, as detailed in table 4.4. A single mass-loading is considered for cases 1 and 2 whilst two different mass-loadings are considered for case 3. The results obtained are compared with those of Benavides and van Wachem [8] and the experimental data of Fessler and Eaton [40], presented below.

The prediction of the solid phase velocity and fluid phase turbulent kinetic energy shows generally good agreement with the numerical data of Benavides and van Wachem [8] and

Table 4.4: Description of particle phase for particle-laden backward facing step flow.

	$\mathcal{ML}$ [%]	d^p [μm]	ρ^s [kg m^{-3}]	Re^p	St
case 1	40	150	2500	10.1	7.9
case 2	20	90	2500	2.9	3.8
case 3	10 40	70	8800	4.4	7.4

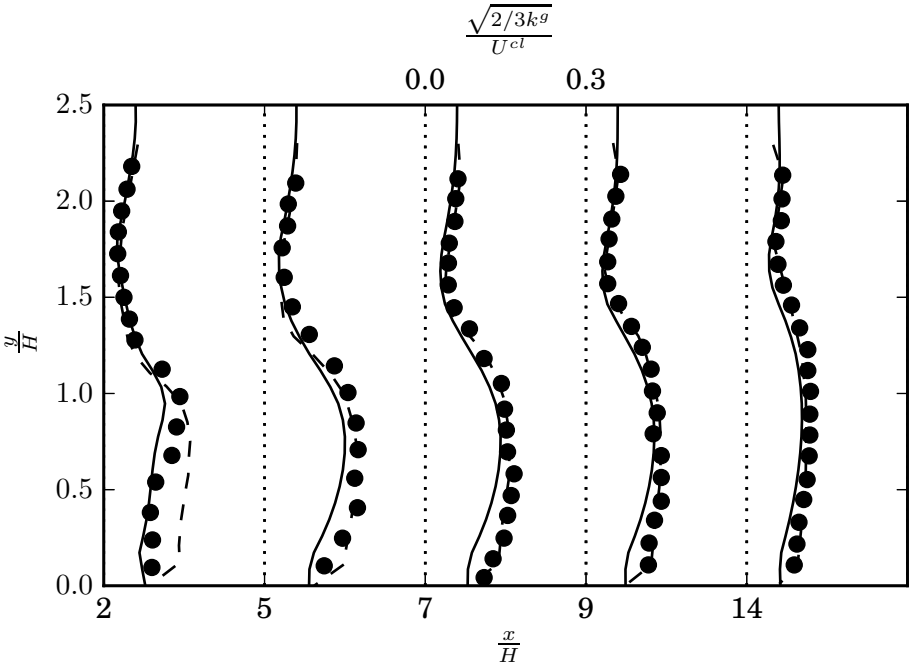

Figure 4.3: Gas phase fluctuating kinetic energy for case 1 at mass loading $\mathcal{ML} = 40\%$. Numerically obtained data is plotted as solid lines, experimental data as points and the numerical data of Benavides and van Wachem [8] as dashed lines.

experimental data of Fessler and Eaton [40], however there is a slight over-prediction of the solid phase velocity compared to the experimental data towards the outlet which is also seen in the numerical data of Benavides and van Wachem [8]. The solid phase velocity predicted numerically in this work does however show a deterioration in agreement with the experimental and numerical data used for comparison towards the lower wall. One possible cause for this discrepancy is the generally poor prediction of granular temperature, however the numerical results of Benavides and van Wachem [8] show a relatively wide spread of granular temperature also. At the same time the better prediction of solid phase velocity by Benavides and van Wachem [8] even where the granular temperature is underpredicted suggests that the simplified boundary conditions applied here in the form of free slip at the wall for the solid phase deserves

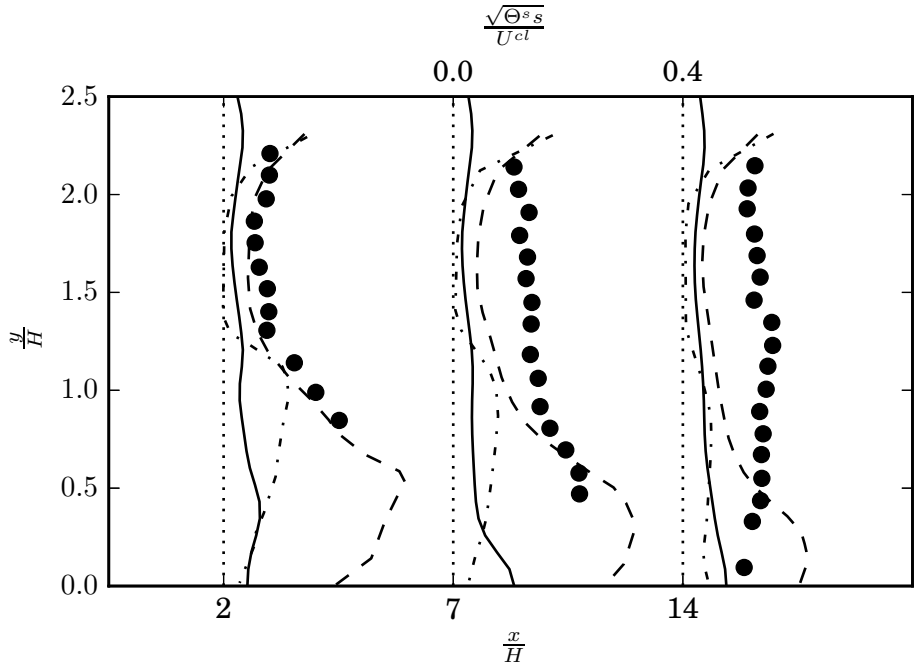

Figure 4.4: Solid phase granular temperature for case 1 at mass loading $\mathcal{ML} = 40\%$. Numerically obtained data is plotted as solid lines, experimental data as points and the numerical data of Benavides and van Wachem [8] as dashed and dash-dotted lines.

revisiting. For example in Benavides and van Wachem [8] a wall stress is imposed in the solid phase similarly to the boundary conditions used for the gas phase, given as

$$\tau^{s,w} = \frac{\pi\alpha^{s,P}}{6\alpha^{s,max}}\rho^s\psi^{s,w}g_0\sqrt{\Theta^{s,P}}\mathcal{U}^{s,P} \tag{4.56}$$

where $\psi^{s,w} = 0.005$ is the specularity coefficient, the proportion of collisions transferring momentum to the wall. By changing the shear stress at the wall, this would also have an impact on the production of granular temperature. In particular, the predictions for granular temperature in this work show worst agreement in the near wall regions towards the walls and it is thought this can be attributed, at least in part, to the lack of production there due to the free slip boundary condition. It is noted that Benavides and van Wachem [8] also imposed a boundary condition for granular temperature based on a balance of energy at the wall, however it has elsewhere been reported that the granular temperature is relatively insensitive to the use of adiabatic boundary conditions as applied here [6, 89].

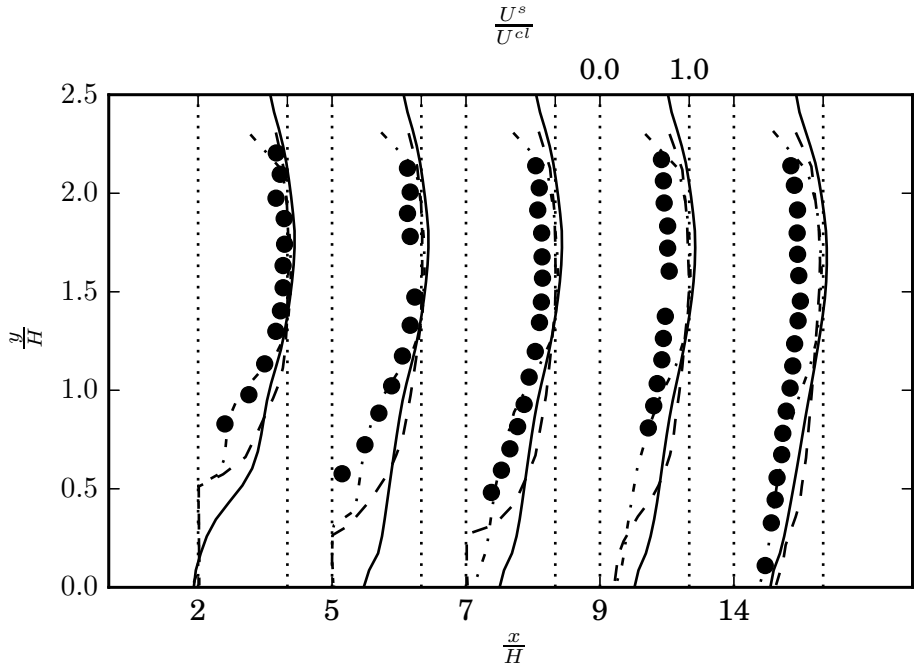

Figure 4.5: Solid phase stream-wise velocity for case 1 at mass loading $\mathcal{ML} = 40\%$. Numerically obtained data is plotted as solid lines, experimental data as points and the numerical data of Benavides and van Wachem [8] as dashed and dash-dotted lines.

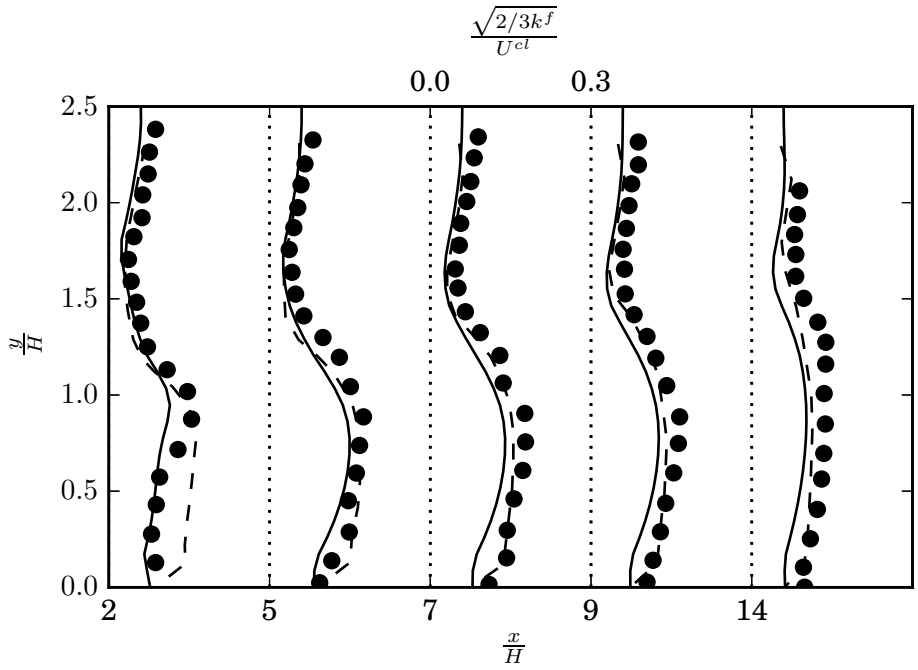

Figure 4.6: Gas phase fluctuating kinetic energy for case 2 at mass loading $\mathcal{ML} = 20\%$. Numerically obtained data is plotted as solid lines, experimental data as points and the numerical data of Benavides and van Wachem [8] as dashed lines.

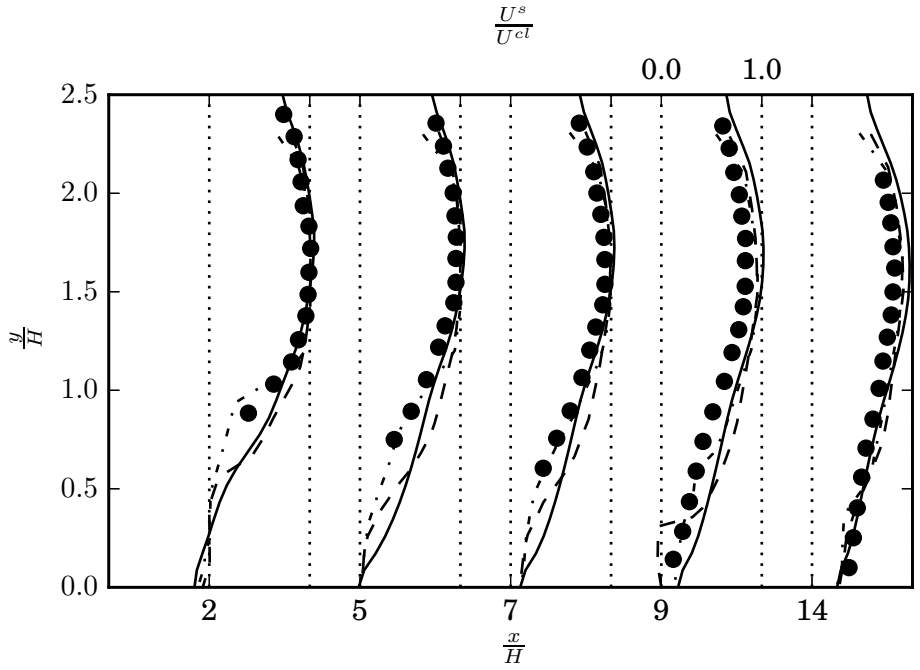

Figure 4.7: Solid phase stream-wise velocity for case 2 at mass loading $\mathcal{ML} = 20\%$. Numerically obtained data is plotted as solid lines, experimental data as points and the numerical data of Benavides and van Wachem [8] as dashed and dash-dotted lines.

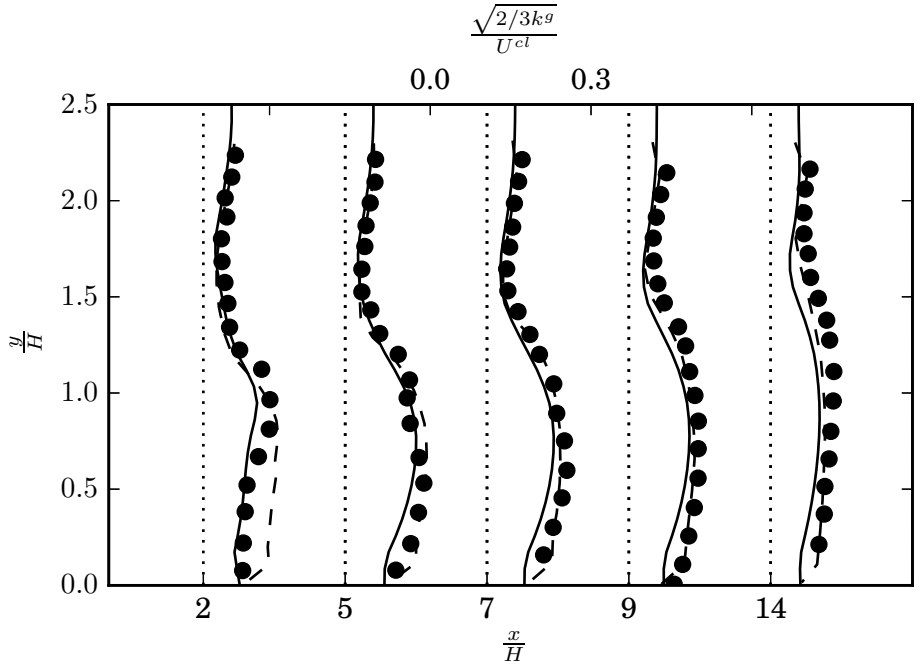

Figure 4.8: Gas phase fluctuating kinetic energy for case 3 at mass loading $\mathcal{ML} = 40\%$. Numerically obtained data is plotted as solid lines, experimental data as points and the numerical data of Benavides and van Wachem [8] as dashed lines.

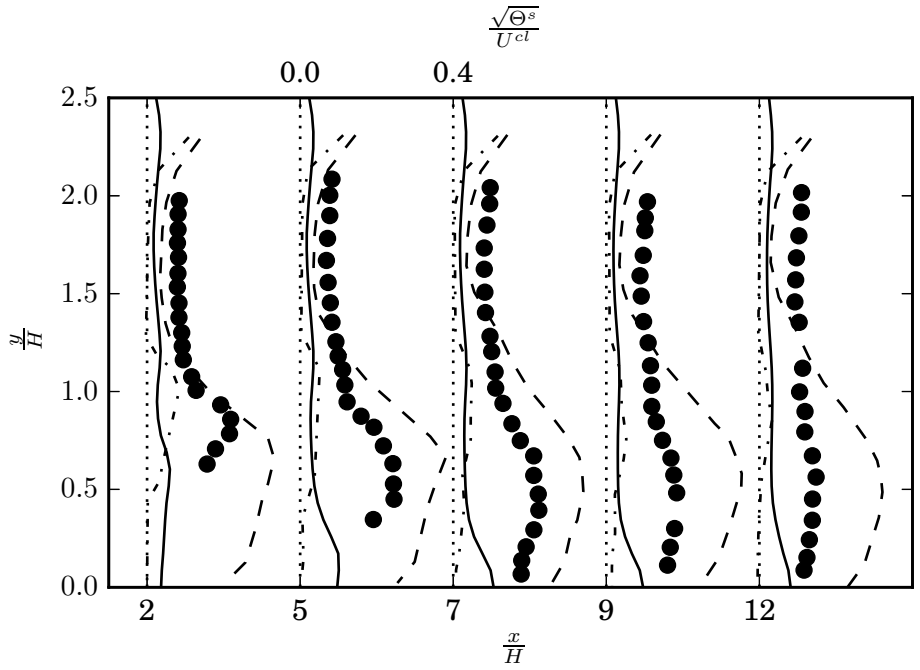

Figure 4.9: Solid phase granular temperature for case 3 at mass loading $\mathcal{ML} = 10\%$. Numerically obtained data is plotted as solid lines, experimental data as points and the numerical data of Benavides and van Wachem [8] as dashed and dash-dotted lines.

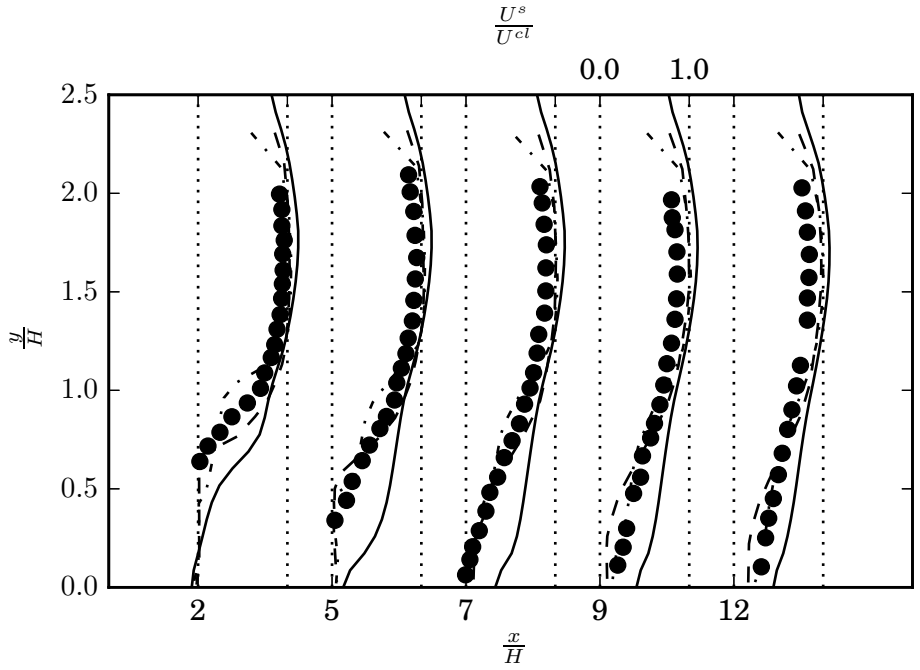

Figure 4.10: Solid phase stream-wise velocity for case 3 at mass loading $\mathcal{ML} = 10\%$. Numerically obtained data is plotted as solid lines, experimental data as points and the numerical data of Benavides and van Wachem [8] as dashed and dash-dotted lines.

4.4.2 Bluff Body Flow

The bluff body flow studied experimentally by Boree *et al.* [10] consists of a central jet and a coaxial flow discharging into a plenum as shown in *fig.* 4.11. Three different flows are considered: a single phase flow and two gas-solid flows with glass beads injected into the central jet to give mass loading ratios of $\mathcal{ML} = 22\%$ and $\mathcal{ML} = 110\%$. The phase properties, flow conditions and dimensions of the domain are given in table 4.5. In the experiment the solid phase consists of polydispersed particles with diameters in the range 20 μm $\leq d^p \leq$ 100 μm [10], here the solid phase is represented by a single Eulerian phase using the mass-averaged particle diameter and it is this value that is reported in table 4.5.

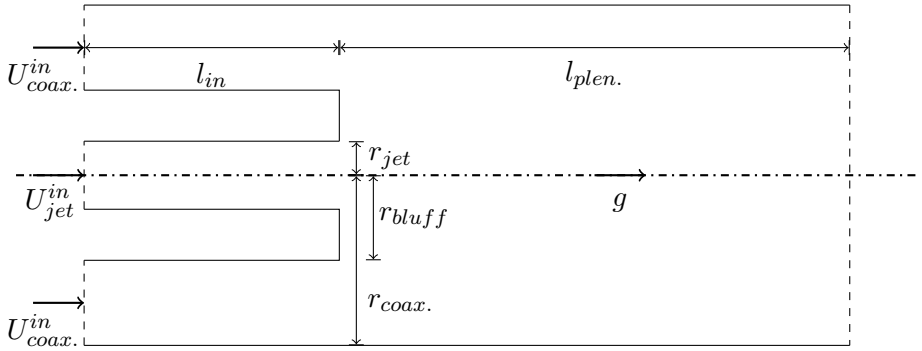

Figure 4.11: Diagram of the bluff body domain.

Table 4.5: Bluff body flow conditions.

Quantity		Value
r_{jet}	[m]	10×10^{-3}
r_{bluff}	[m]	75×10^{-3}
$r_{coax.}$	[m]	150×10^{-3}
l_{in}	[m]	200×10^{-3}
$l_{plen.}$	[m]	500×10^{-3}
$U^{g,cl}_{jet}$	[m s^{-1}]	4.1
$U^{g,cl}_{coax.}$	[m s^{-1}]	6
$\dot{m}^s_{jet}$	[kg h^{-1}]	1 ($\mathcal{ML} = 22\%$) 5 ($\mathcal{ML} = 110\%$)
d^p	[μm]	63
ρ^g	[kg m^{-3}]	1.19
ρ^s	[kg m^{-3}]	2470
μ^g	[Pa s]	1.81×10^{-5}

The computational domain is truncated at the inlet rather than use the full 2 m length of inlet in the experiment and similarly the plenum is truncated to reduce computation time. As

reported, the length of the jet inlet is sufficiently long for the gas to reach a fully-developed state whilst the coaxial flow is thought to be slightly underdeveloped [10], therefore to account for the truncation of the computational domain, one-seventh power law profiles are specified as inlet conditions for the gas phase velocities. The solid phase is introduced at the jet inlet with velocity equal to the gas velocity and the volume fraction determined by satisfying the mass loading conditions for the given case. A small amount of particles are also introduced in the coaxial flow for the simulations to prevent the solid phase attaining unreasonably high velocities there which may impact upon the gas phase, setting a mass loading $\mathcal{ML} \approx 2 \times 10^{-3}$ %, their presence should have a negligible effect on the gas phase. All variables are initialised to their inlet values in the jet and coaxial inlet regions ($z < 0$ mm) whilst in the plenum ($z > 0$ mm) they are initialised with area averaged values. Based on the experimental data, the turbulent intensity of the single phase flow in the jet and coaxial sections is estimated to be $I^t_{jet} = 10.4\%$ and $I^t_{coax.} = 8\%$ respectively.

Grid dependence of the simulation is investigated by first simulating the single phase flow on three meshes of increasing resolution, presented in §4.4.2.1. In all cases the numerical results are compared against the experimental data available at [50][1].

4.4.2.1 Single Phase Flow

Of particular interest in this flow is the recirculation region and the stagnation points which occur within it and how the particles interact with these flow structures. The single phase flow is therefore used to study grid dependence, paying particular attention to the prediction of the stagnation points. Three meshes are considered, approximately doubling the number of cells in each coordinate direction with each refinement, corresponding to $1,092$, $9,975$ and $79,856$ cells respectively and referred to as the coarse, medium and fine meshes below.

The numerically obtained velocity profiles on the three meshes are plotted at several stations downstream of the bluff body and compared against experimental data in *fig.* 4.12. All three meshes show good agreement with each other and the experimental data in the outer or annular region of the flow. The main observed difference between numerical predictions occurs at the station corresponding to non-dimensional location $\frac{3z}{r_{coax.}} = 1.6$ where it can be seen that the

[1]The database is no longer available at the original location ([49]) referenced by Boree *et al.* [10] and was accessed at [50] using the web archive.

axial velocity is severely underpredicted on the centreline on the coarse mesh. The medium mesh shows very good agreement with the centreline velocity, however the shape of the velocity profile in the recirculating region (approximately $0.067 < \frac{r}{r_{coax.}} < 0.5$) is best predicted by the fine mesh data.

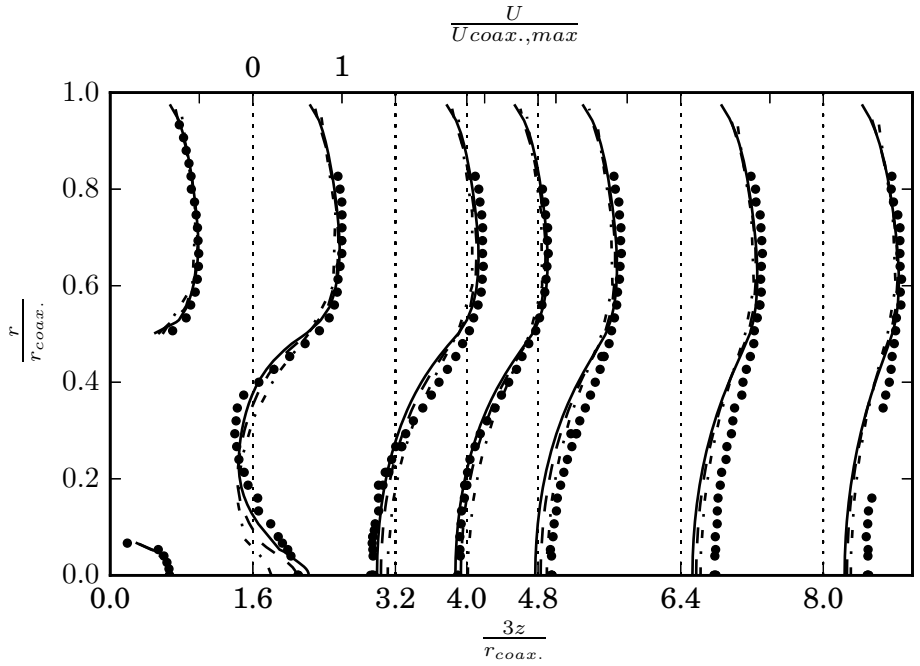

Figure 4.12: Comparison of experimental and numerically predicted velocity profiles downstream of the bluff body. Experimental data is indicated by points, numerical data on the coarse mesh with dash-dotted lines, numerical data on the medium mesh with dashed lines and numerical data on the fine mesh with solid lines. The zero velocity at each axial station is marked by fine dotted lines.

The prediction of the stagnation points, located at $z \approx 112.5$ mm and $z \approx 216.7$ mm respectively [10], is investigated by plotting the axial velocity along the domain axis, shown in *fig.* 4.13. The predicted location of the first stagnation point is in good agreement with the experimental data. This is important in the context of continuing these simulations for particle-laden flows as, at least in the case of the lower mass loading, the particles will stagnate also and be dispersed into the recirculation region [10]. The location of the second stagnation point shows poorer agreement with the experimental data, it is in fact best predicted by the medium mesh. However, it is thought that the location of the first stagnation point, indicating the penetration of the central jet into the recirculation zone is most important, particularly as Boree *et al.* [10] show in their gas-solid flow experiments, when the mass-loading is increased

(hence the jet to coaxial momentum ratio) the jet extends through the recirculation zone. In an attempt to improve the prediction of the second stagnation point location a refinement of the fine mesh (fine-ref), refining only in the axial direction for $z \geq 0$ mm is considered, the numerical data for which is shown in *fig.* 4.13 as a dotted line. This shows little or no change relative to the fine mesh data, hence considering these observations and those above comparing the velocity profiles at several downstream locations, the fine mesh is used for the gas-solid flow simulations.

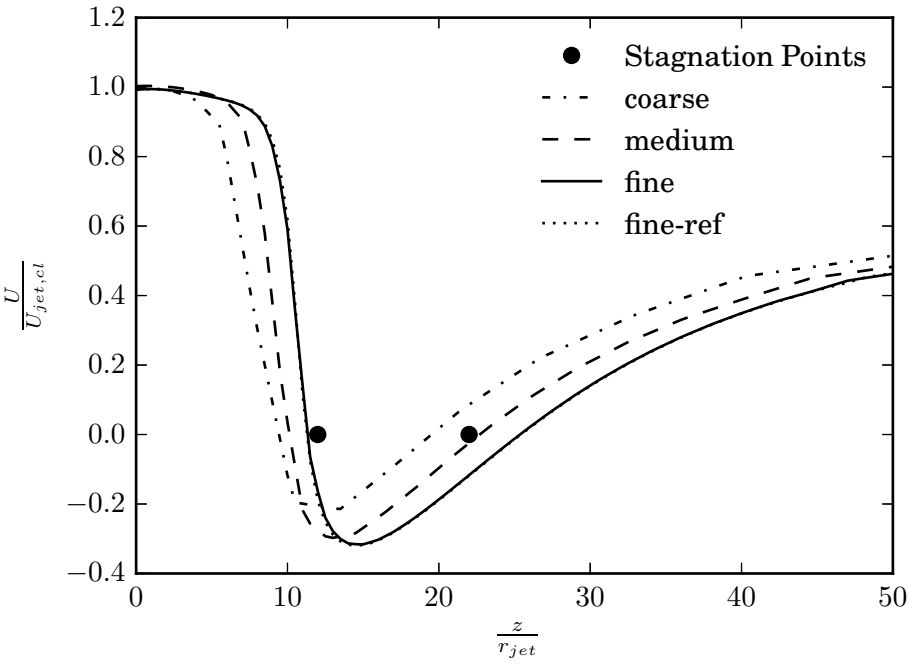

Figure 4.13: Comparison of numerically predicted axial evolution of axial velocity with experimental location of stagnation points. The location of the stagnation points is indicated by points and the numerical data obtained on the coarse, medium and fine meshes with dash-dotted, dashed and solid lines respectively. The data obtained on the fine mesh with axial refinement (fine-ref) is indicated by the dotted line.

4.4.2.2 Particle-Laden Flow

In this section, the results of the particle-laden flow simulations are presented. As identified in the single phase results, presented above in §4.4.2.1, the "fine" and "fine-ref" meshes show convergence of the axial velocity profile and give good prediction of the first stagnation point of the central jet, thought to be critical in predicting the behaviour of the particles, hence the "fine" mesh is used for the particle-laden simulations. Before presenting the numerical results for particle-laden flow, changes which were made to the model to obtain a solution are discussed.

Of particular concern in this simulation is that the coaxial flow of gas is significant and much of the domain clear of particles, representing a similar numerical problem for the two-fluid model as in the fluidised bed simulation discussed in §3.4.4; the problem is again countered, as in §3.4.4, by introducing a small flux of particles in the coaxial flow. To further guard against poor numerical behaviour of the momentum equations as $\alpha^s \to 0$, the solids phase volume fraction is clipped at a small, non-zero value,[2] $\alpha_c^s \ll 1$, when computing the momentum exchange term. This clipping prevents the solids phase momentum equations becoming singular in regions where $\alpha^s \to 0$, instead the solids phase momentum equations tend to $\mathbf{u}^s = \mathbf{u}^g$ as the volume fraction approaches zero.

During simulations it was found that the closure for k^{sg}, the correlation of gas and solids fluctuating velocities, given by Koch [57] as

$$k^{sg} = \frac{\beta d^p (\mathbf{U}^g - \mathbf{U}^s)^2}{4\alpha^s \rho^s g_0 \sqrt{\pi \Theta^s}} \ , \tag{4.57}$$

used initially presented difficulties in obtaining a solution. Equation (4.57) shows that as α^s or Θ^s approach zero this term becomes very large, representing significant sources in the gas turbulent kinetic energy and solids granular temperature transport equations. Therefore a simpler model, given as $k^{sg} = c^{sg}\sqrt{k^g \Theta^s}$ with $c^{sg} = 0.2$ [7], which tends to zero with gas phase turbulent kinetic energy and solids phase granular temperature was used and found to be more stable.

The particle-laden flow at 22% mass loading was simulated using the semi-coupled algorithm and the numerical results obtained compared with the experimental data of Boree *et al.* [10] and the numerical data from a Eulerian-Eulerian Large Eddy Simulation by García *et al.* [41]. As in §4.4.2, the defining features of the flow are the recirculation zones and corresponding stagnation points of the gas and solids phases. Figure 4.14 shows the axial evolution of the gas and solids phase axial velocity obtained numerically alongside the experimental and LES data. One of the key features of the flow at 22% mass loading is the stagnation of both the gas and solids phases, with the solids phase stagnation point occurring downstream of that of the gas phase. This behaviour is visible in *fig.* 4.14 showing the centreline values of the gas and solids phase axial velocities.

[2]This approach, to clip the solids phase volume fraction when used in computation of the momentum exchange term was suggested by Alan Burns in private communication.

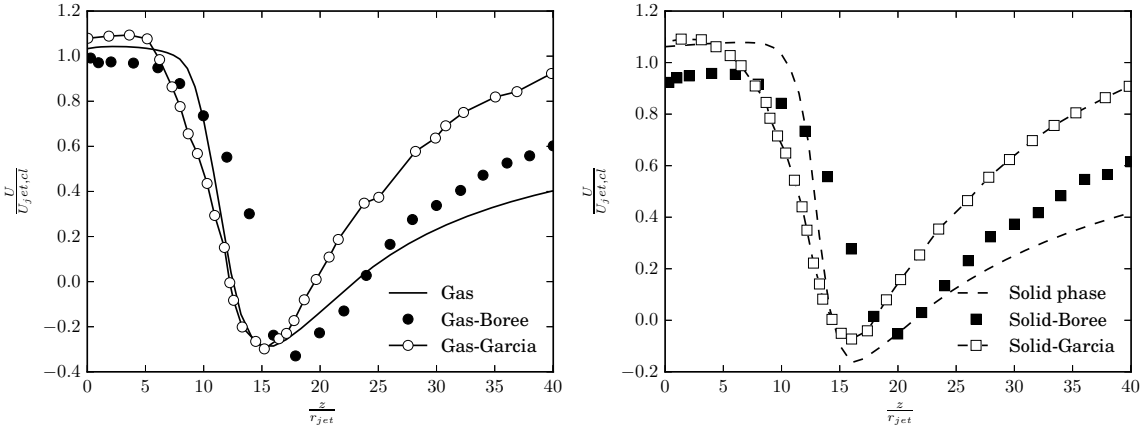

(a) Gas phase axial velocity

(b) Solids phase axial velocity

Figure 4.14: Axial evolution of gas and solids phase axial velocities. The numerical data are represented by lines, the experimental data of Boree *et al.* [10] by solid markers and the LES data of García *et al.* [41] by lines with open symbols.

Both the numerical data obtained here and the LES data used for comparison agree reasonably well for the gas phase velocity up to the minimum occurring at $z \approx 15r_{jet}$ after which there is a marked difference with the data obtained in this work underpredicting the recovery of gas phase velocity whilst in the LES data it is overpredicted. A consequence of the underpredicted recovery of the axial velocity (also observed in the solids phase) is that the second stagnation point for both phases is predicted well, however the predicted length of the recirculation zones suffers as a result relative to that predicted by García *et al.* [41] which more closely matches the experimental values.

The first stagnation point of the solids phase can also be seen by examining the axial profile of solids phase volume fraction, plotted in *fig.* 4.15. In this figure, the axial location of peak concentration for $d^p = 60$ μm class particles reported by Boree *et al.* [10] is indicated by a dotted line at $z = 16r_{jet}$. As can be seen, the peak solids phase volume fraction predicted numerically occurs at $z \approx 14r_{jet}$, slightly upstream of the experimental location of peak concentration of $d^p = 60$ μm class particles. This offset in the predicted location of the volume fraction peak is to be expected based on the location of zero axial velocity predicted numerically versus the experimental location shown in *fig.* 4.14. The peak volume fraction is also overpredicted, Boree *et al.* [10] report a peak concentration of approximately 3 times the inlet value whereas here the peak is seen to be approximately 7 times the inlet value. This overprediction is potentially caused by the use of a monodispersed solids phase in the simulations assigning the constant

diameter as the mass averaged value: $d^p = 63$ μm; in contrast to the experiments of Boree *et al.* [10] which have a polydispersed solids phase with diameters in the range 20 μm $\leq d^p \leq$ 100 μm. Therefore in the numerical simulations, all the particles are stagnating at a single location, leading to a high volume fraction whereas in the experiments each class of particles, representing only a proportion of the solids phase, stagnate at different points due to differences in particle response times, resulting in a relatively lower peak in volume fraction.

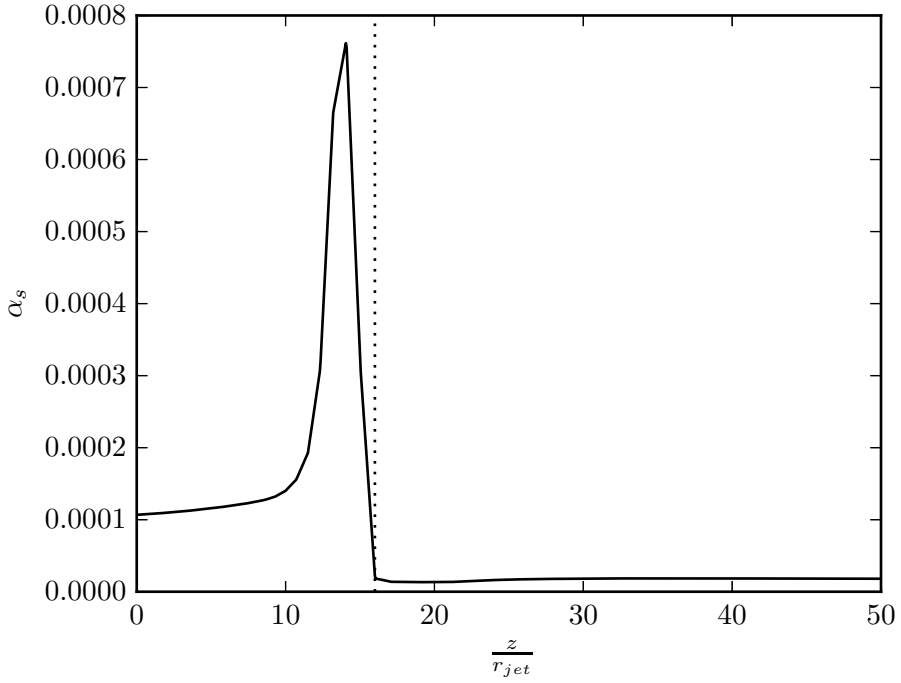

Figure 4.15: Axial evolution of solids phase volume fraction. Numerical data is indicated with a solid line whilst the location of peak concentration for $d^p = 60$ μm particles reported by Boree *et al.* [10] is indicated by a dotted line.

In addition to the axial profiles, the radial profiles of axial velocity of both phases are plotted at several stations downstream of the bluff body: $z = 3r_{jet}$, $z = 80r_{jet}$, $z = 160r_{jet}$ and $z = 240r_{jet}$, shown in *fig.* 4.16 and *fig.* 4.17 for gas and solids phases respectively.

The numerical predictions of the velocity profiles for the gas phase are generally in good agreement with the experimental data. The major discrepancies are the underprediction of the strength of recirculation visible at station $z = 80r_{jet}$ (*fig.* 4.16b), and the evidence of the stagnation of the gas phase occurring too early in the numerical results is visible as the underprediction of velocity at the centreline of station $z = 160r_{jet}$ (*fig.* 4.16c). The solids phase velocity profiles are again in good agreement with the experimental data of Boree *et al.* [10] and

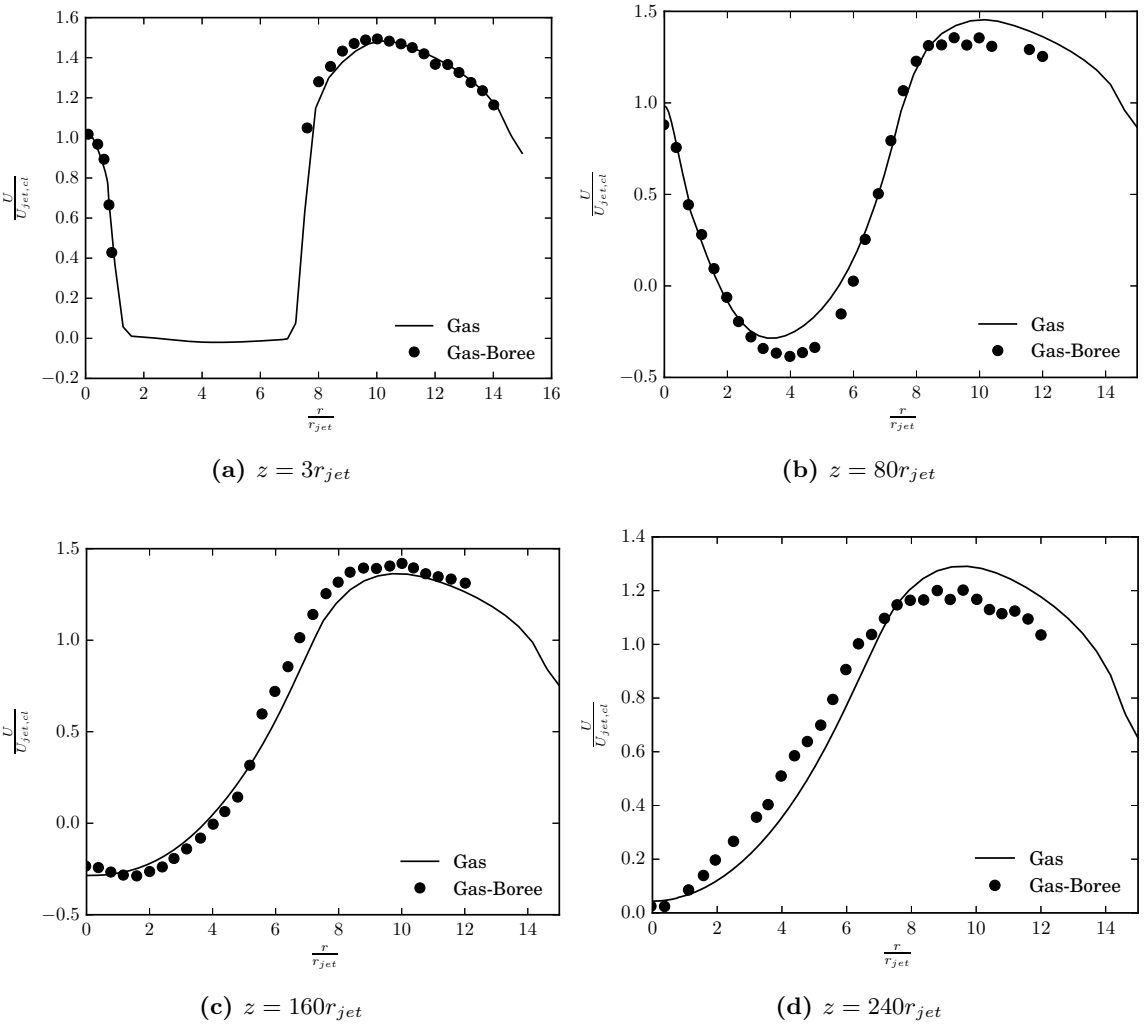

(a) $z = 3r_{jet}$ **(b)** $z = 80r_{jet}$

(c) $z = 160r_{jet}$ **(d)** $z = 240r_{jet}$

Figure 4.16: Radial profiles of gas phase velocity at several axial stations. Numerical data is indicated by a solid line, the experimental data of Boree *et al.* [10] is indicated by solid symbols.

the LES results of García *et al.* [41], except at station $z = 160r_{jet}$ at which both the numerical results presented here, and those of García *et al.* [41], significantly underpredict the penetration of the solids jet as visible in the difference between the numerical data (which are in good agreement) and the experimental data near the centreline.

The good prediction of velocity profiles at the first station ($z = 3$ mm) with subsequent deterioration downstream observed in both the axial and radial profiles of velocity is attributed to the poor prediction of turbulent statistics, related in part to a lack of upstream data for boundary conditions. For example, as described in §4.4.2, the velocity profiles at the inlets to the jet and coaxial flow are determined by assuming that the gas phase is a fully developed turbulent flow following a $1/7^{th}$ power law profile and the velocity of the solids phase set equal to

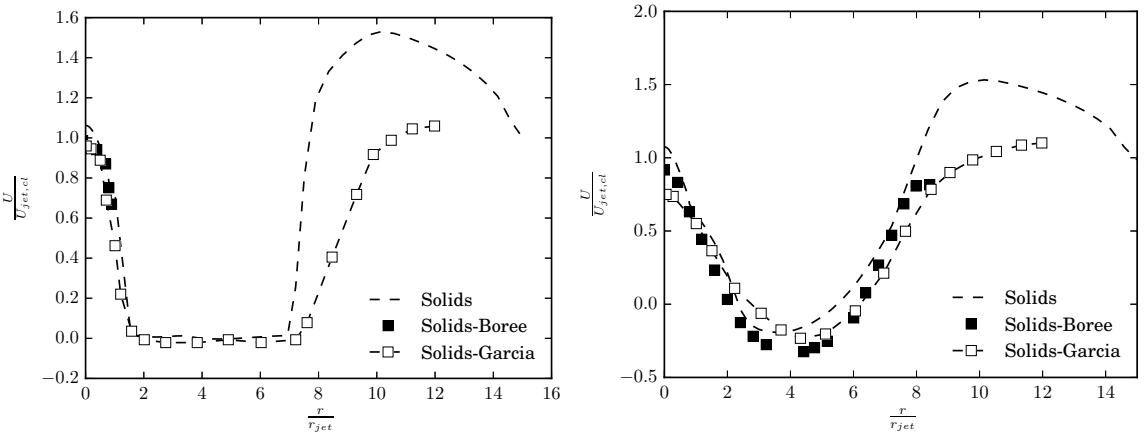

(a) $z = 3r_{jet}$ **(b)** $z = 80r_{jet}$

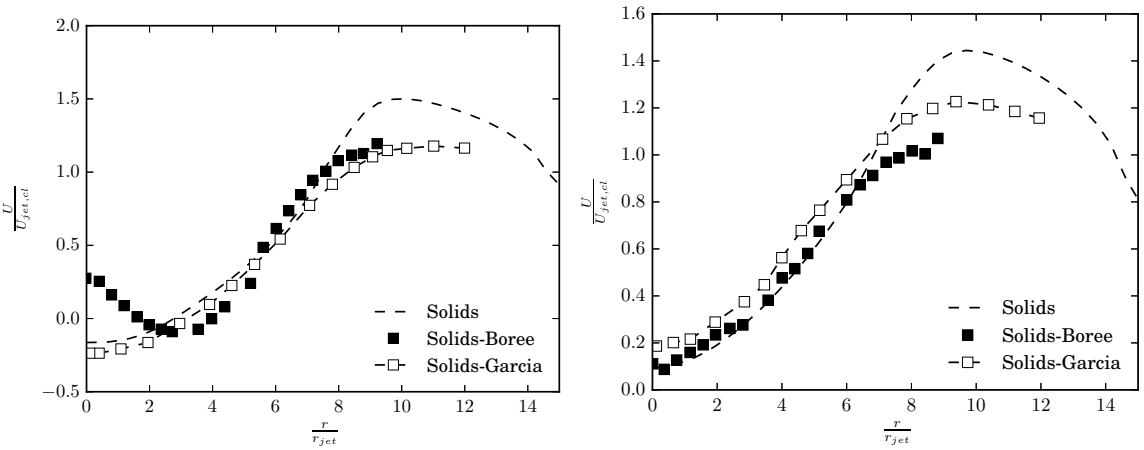

(c) $z = 160r_{jet}$ **(d)** $z = 240r_{jet}$

Figure 4.17: Radial profiles of solids phase velocity at several axial stations. Numerical data is indicated by a dashed line, the experimental data of Boree *et al.* [10] is indicated by solid symbols and the numerical data of García *et al.* [41] by dashed line with open symbols.

the gas phase. The volume fractions at the inlet are then specified to satisfy the given mass flow rates in the experiment, and as *fig.* 4.16a and *fig.* 4.17a show, there is good agreement between the numerically predicted and experimental velocity profiles at the first station. However, the first data available for turbulent quantities is at the first station, and this was used as the inlet boundary condition, with ε estimated using the approach given by Ferziger and Perić [39]

$$\varepsilon^{g,in} \approx \frac{{k^{g,in}}^{1.5}}{l^{g,in}} \ , \tag{4.58}$$

where $l^{g,in}$ is equal to $1/10^{th}$ the height of the shear layer at the inlet. This, of course, does not take into account turbulent dissipation within the upstream region of the flow. To resolve these

issues, forcing was applied to the transport equations for tubulent quantities so that the radial profiles match the experimental data at the first measurement location. The forcing takes the form:

$$\alpha^g \rho^g \frac{Dk^g}{Dt} = F^{k,g} + c\left(k^{g,in} - k^g\right) \ , \tag{4.59}$$

for $z \leq 0$ where $\frac{D(\cdot)}{Dt}$ is the material derivative; the diffusion, production and dissipation terms in the model have been collected into $F^{k,g}$ for clarity; and the additional forcing term added is comprised of the inlet value, $k^{g,in}$, (estimated using the experimental data at $z = 3$ mm) and $c \gg 1$ chosen sufficiently large that the transport equation in the inlet section reduces to

$$k^g = k^{g,in} \ , \tag{4.60}$$

ensuring that at the jet/coaxial flow exit the turbulent quantities remain near the reported values. An equivalent approach is also taken in the transport equations for dissipation of gas phase turbulent kinetic energy and the solids phase granular temperature. The numerical results obtained using such an approach are presented below and compared with the original numerical results and the experimental data of Boree *et al.* [10].

The comparison between the initial results and those with forced turbulent quantities illustrate the sensitivity of this case to the turbulent quantities in the gas and solids phases. In particular, the stagnation points of the gas and solids phases are delayed relative to the initial numerical results. Consequently, the penetration of the solids phase jet to station $z = 160 r_{jet}$ (*fig.* 4.19c) can be seen, whereas both the initial numerical results presented earlier, and those of García *et al.* [41] failed to capture this.

Finally, the case is also simulated with the fully-coupled algorithm and the results compared against those obtained with the semi-coupled algorithm; the results presented are those obtained using forcing of the turbulent quantities in the inlet region described above.

As expected, the semi- and fully-coupled algorithms show excellent agreement with each other with only minor discrepancies. These minor discrepancies, noting the generally good agreement between both algorithms, suggest that the solution is close to, but has not quite reached, a steady state. The wall clock times were $46,046$ s and $41,223$ s running on 16 cores for the semi- and fully-coupled algorithms respectively, however it should be noted that the

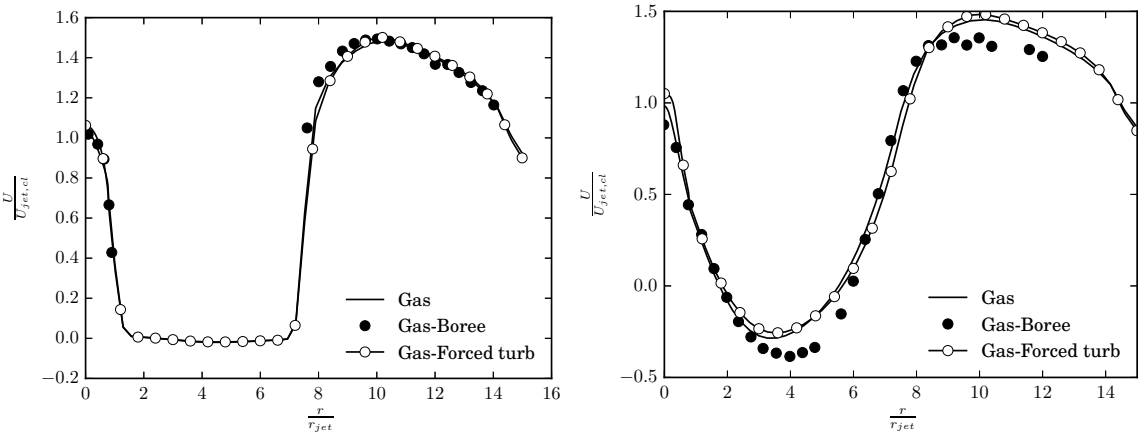

(a) $z = 3r_{jet}$ **(b)** $z = 80r_{jet}$

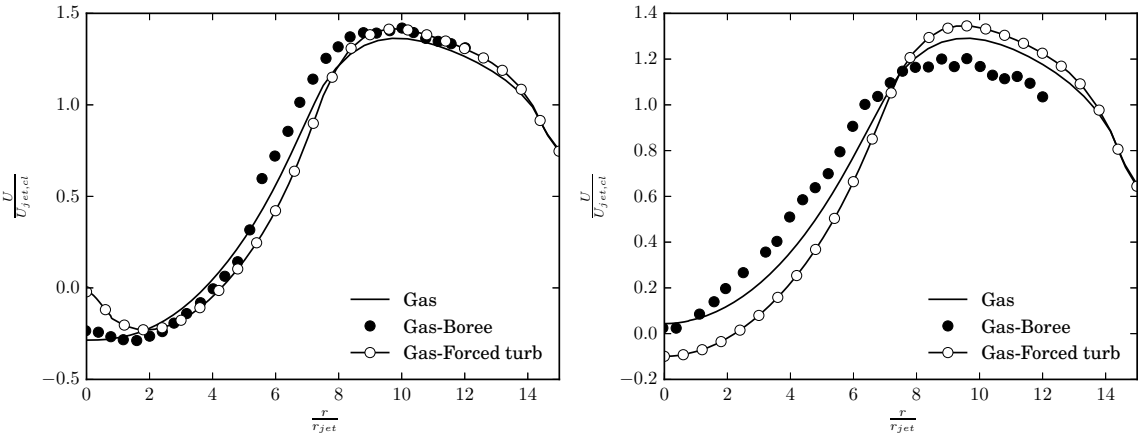

(c) $z = 160r_{jet}$ **(d)** $z = 240r_{jet}$

Figure 4.18: Radial profiles of gas phase velocity at several axial stations. Numerical data as originally simulated is indicated by a solid line, experimental data of Boree *et al.* [10] by solid symbols and numerical data obtained with forcing of turbulence in inlet by solid line with clear symbols.

simulations were performed with adaptive time-steps, using the criterion $CFL \leq 0.2$, making it difficult to draw meaningful performance conclusions from this data.

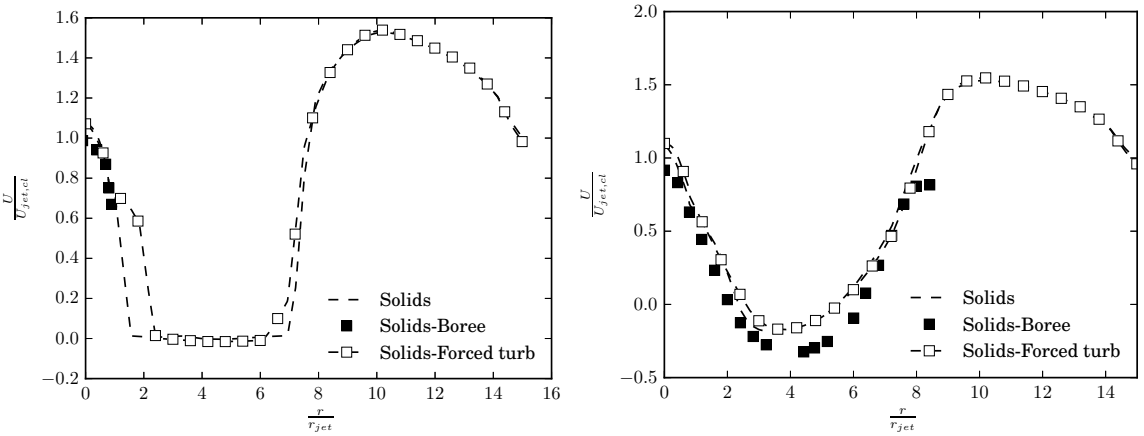

(a) $z = 3r_{jet}$ **(b)** $z = 80r_{jet}$

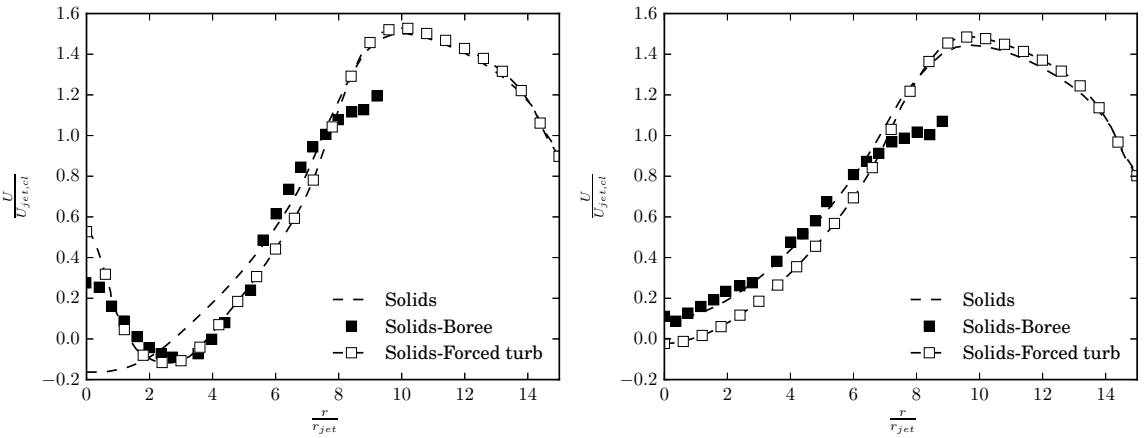

(c) $z = 160r_{jet}$ **(d)** $z = 240r_{jet}$

Figure 4.19: Radial profiles of solids phase velocity at several axial stations. Numerical data as originally simulated is indicated by a dashed line, experimental data of Boree *et al.* [10] by solid symbols and numerical data obtained with forcing of turbulence in inlet by dashed line with clear symbols.

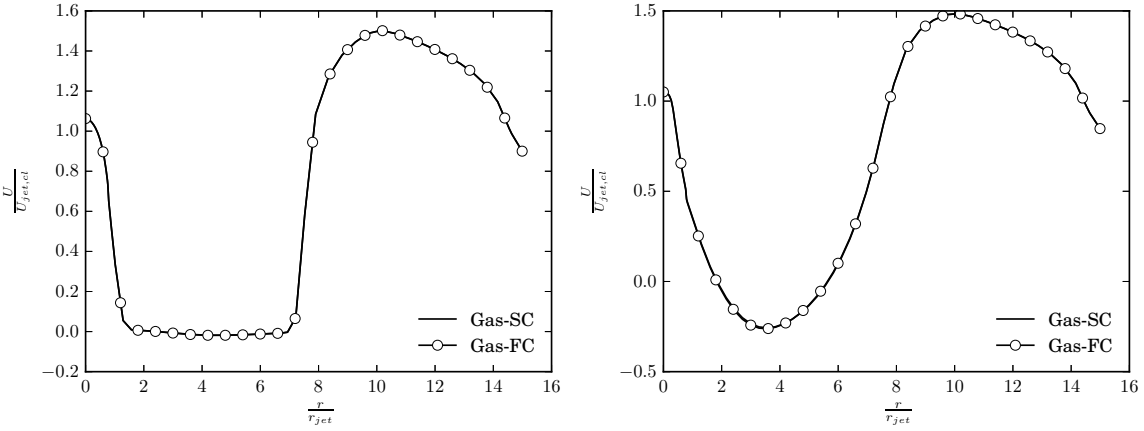

(a) $z = 3r_{jet}$ **(b)** $z = 80r_{jet}$

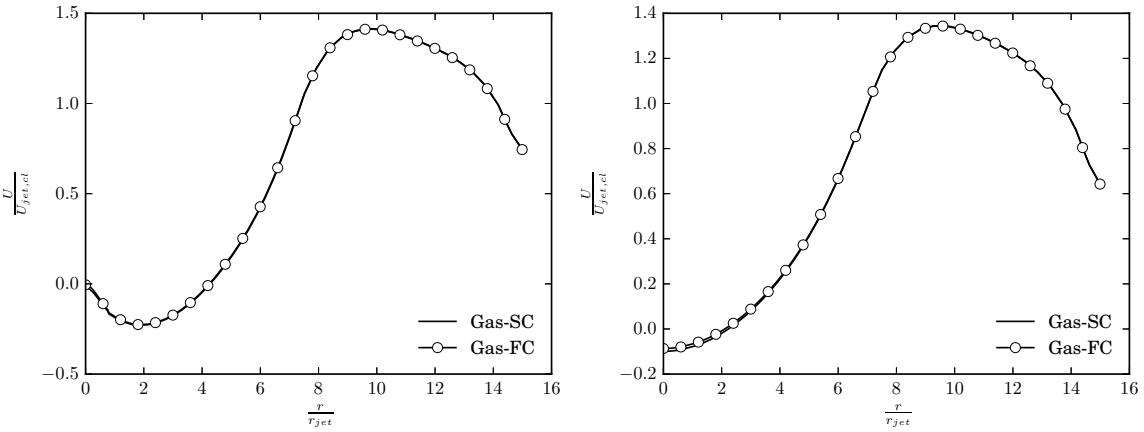

(c) $z = 160r_{jet}$ **(d)** $z = 240r_{jet}$

Figure 4.20: Radial profiles of gas phase velocity at several axial stations. Both sets of data simulated with forcing of turbulence in inlet. Numerical results for semi-coupled algorithm indicated by solid line and for fully-coupled algorithm by solid line with clear symbols.

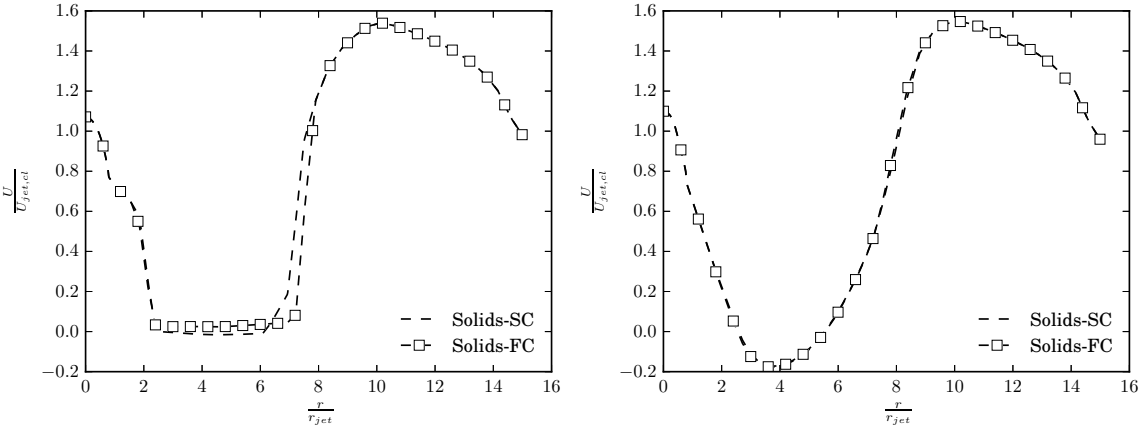

(a) $z = 3r_{jet}$ **(b)** $z = 80r_{jet}$

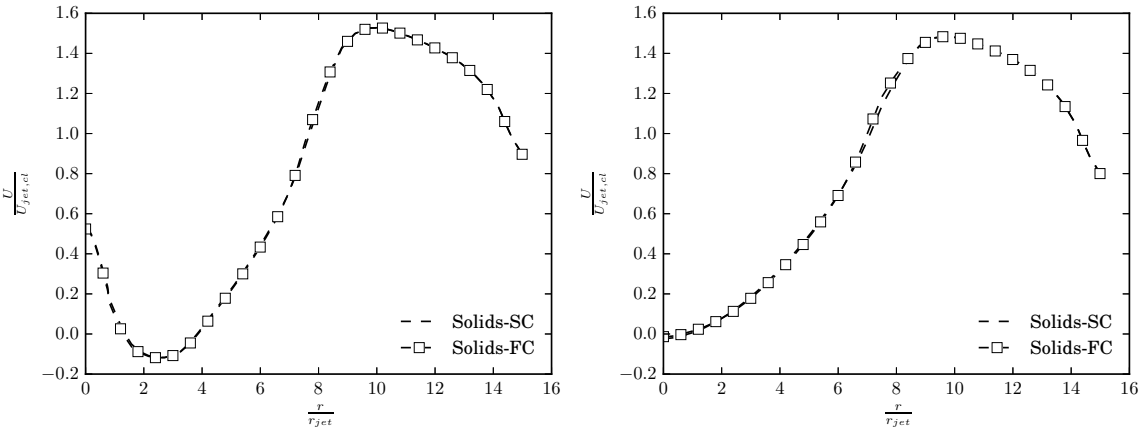

(c) $z = 160r_{jet}$ **(d)** $z = 240r_{jet}$

Figure 4.21: Radial profiles of solids phase velocity at several axial stations. Both sets of data simulated with forcing of turbulence in inlet. Numerical results for semi-coupled algorithm indicated by dashed line and for fully-coupled algorithm by dashed line with clear symbols.

4.5 Conclusions

Turbulent flows have been simulated in two configurations: a backwards facing step and a bluff body flow. In both cases single phase and gas-solid flows are considered, with the gas-solid flows modelled with the two-fluid model. The gas phase turbulence was modelled using the $k-\varepsilon$ model and turbulence in the dispersed phase using KTGF with the viscosity closure models proposed by Benavides *et al.* [9] and Benavides and van Wachem [8], accounting for the interaction between particles and turbulent eddies in the gas. The two-fluid model with the presented closures was solved using the fully-coupled algorithm developed in chapter 3.

The numerical results obtained for the single phase flow in the backwards facing step showed good agreement with experimental data, however it was found that there is room for improvement in the simulation of gas-solid flow. In particular, the use of simplified boundary conditions for the solid phase in the form of free slip at the wall is identified as a possible cause for the discrepancy with the fluctuating energy of the gas phase showing good agreement with the experimental data and the numerical data of Benavides and van Wachem [8] used for comparison.

Results for the single phase flow in the bluff body case show good prediction of the location of the first of two stagnation points. As the purpose of this test case is to investigate the dispersal of the particles in the recirculation region, accurate prediction of these flow structures is vital, however further axial refinement of the "fine" mesh in the plenum did not improve the prediction of the second stagnation point (which was in fact better on a coarser mesh) and the "fine" mesh was taken as the mesh to work with for the particle-laden flow. The numerical predictions of the particle-laden flow showed generally good agreement for the gas phase with the experiments, however the location of the stagnation points was poorly predicted, as also found in García *et al.* [41], and the recovery of axial velocity is underpredicted in contrast to García *et al.* [41] where it is overpredicted. The situation for the solid phase is similar with both the numerical data presented here and that of García *et al.* [41] underpredicting the penetration of the central jet of solids into the domain. An attempt was made to improve the results by forcing the turbulent quantities in the inlet region owing to lack of data for the inlet boundary condition, leading to some improvement in terms of predicting the penetration of the central jet of solids, however it is clear that the case is extremely dependent on these quantities and further work is required.

Chapter 5

Conclusion

In this thesis, a fully-coupled solution algorithm for the two-fluid model was developed. Driving this development was the highly non-linear nature of the two-fluid model and the stiff source terms which can arise both within and between each phase when modelling gas-solid flows. By solving the two-fluid model implicitly, as in the fully-coupled algorithm, these stiff source terms might be treated implicitly due to the additional coupling between equations resulting from Newton linearisation. By treating these stiff source terms implicitly, the aim was to obtain a more robust algorithm. An additional benefit is that, being based on Newton's algorithm, convergence should be fast for starting data sufficiently close to the solution. In developing the fully-coupled algorithm, it was noted that the Newton linearisation of the momentum equations gave rise to terms implicit in volume fraction (specifically the transient and advective contributions) that could become large relative to the main diagonal terms acting on velocity if the volume fraction approaches zero. Numerically, it is desirable to maintain diagonal dominance to promote stability when using iterative solvers, therefore it was proposed to discretise the momentum equations according to the practice proposed by Patankar [71]. This enhances the diagonal dominance of the momentum equations in the fully-coupled algorithm by removing the transient contribution coming from volume fractions. Furthermore when the velocity field is uniform, the volume fraction terms drop out entirely, resulting in an easier equation to solve.

For comparison purposes a semi-coupled algorithm based on a Picard linearisation of the two-fluid model was also implemented. By using a Picard linearisation, the two-fluid model segregates into two smaller sub problems: a coupled pressure-velocity equation system and a separate equation system for the volume fraction transport. Applying both algorithms to several test

cases showed that in a complex transient flow such as a fluidised bed, the fully-coupled algorithm offers some benefit in terms of time-to-solution, however in simpler flows the difference between the two algorithms is minimal with the simplest case favouring the semi-coupled algorithm. The theorised improvement in robustness of the fully-coupled algorithm over the semi-coupled algorithm was not realised, in practice it was found that the same time-step was required to simulate the fluidised bed as for the semi-coupled algorithm. This suggests that it is the implicit coupling of pressure and velocity and the implicit treatment of interphase coupling terms that is shared by both the semi- and fully-coupled algorithms that contribute most to the robustness of the algorithms.

Both algorithms were implemented in the context of an unstructured FVM code using a collocated variable arrangement. To prevent pressure-velocity decoupling in collocated variable arrangements, a discretisation enforcing a link between adjacent pressure values, such as MWI, is required. Due to the additional complexity of the two-fluid model as applied to gas-solid flows sharing a single pressure field between both phases, and the central role played by MWI in forming the discrete pressure equation, a detailed study of MWI starting from first principles was undertaken. It was shown that as MWI enforces a spatial coupling of the discrete pressure field, when the problem gives rise to pressure fields the discretisation cannot reproduce, this error results in a force imbalance, accelerating the fluid. Situations in which this can arise include discontinuities in the momentum source term or density fields. In both cases, the correct solution is a discontinuous pressure gradient, however a linear discretisation of the pressure field cannot reproduce this discontinuous gradient, leading to artificial accelerations as described above. It was shown that by rediscretising the source terms consistently with the pressure gradient, this might be avoided, however care must be taken in unstructured meshes to ensure that the discretisation of the pressure gradient and the source term exactly match otherwise force imbalances may still occur on complex meshes. Also it was shown that the rediscretisation of the source terms is dissipative, essentially smoothing discontinuities in the source term field. When rediscretising a point source on nonuniform meshes, the total force is reduced, leading to the pressure drop being underpredicted. This was resolved by accounting for the mesh nonuniformity in the source term discretisation, ensuring the force applied by the input, and rediscretised source is the same, giving the correct prediction of pressure drop even on highly stretched meshes. These proposed modifications to MWI are generally applicable to the discretisation of flows

using a collocated variable arrangement.

5.1 Future Work

The work presented in this thesis demonstrates that a fully-coupled algorithm is a viable approach for solving the two-fluid model. However, as noted, the difference in performance relative to the semi-coupled algorithm is marginal in many cases. One potential area for improvement is the development of a custom preconditioner for the fully-coupled algorithm. A starting point for the development of such a preconditioner would be to extend the SIMPLE-type preconditioners employed in coupled solvers for single phase flows [55] to the two-fluid model based on the IPSA algorithm [84]. This would also be of benefit to the semi-coupled algorithm as the velocity prediction - pressure correction step embedded within the IPSA algorithm could be used to precondition the coupled pressure-velocity problem of the semi-coupled algorithm. Indeed, just as the development of the semi- and fully-coupled algorithms complemented each other, so too could the preconditioner be developed in stages, first as a preconditioner for the semi-coupled algorithm before being extended to the fully-coupled algorithm. In theory the semi-coupled algorithm itself could be used as a preconditioner to the fully-coupled algorithm, however there is a trade-off between the power of the preconditioner and the effort required in its application. It is expected that whilst such an approach would likely be robust, the resulting solver would require significant computational effort.

In both the semi- and fully-coupled algorithms $\alpha^k > 0$ is required to prevent the momentum equations for phase k becoming singular (see for example the discussion relating to the freeboard of the fluidised bed in §3.4.4 and [87, 89]). Oliveira and Issa [69] present an approach to circumvent this problem by solving the two-fluid model equations in non-conservative form, allowing the momentum equations to be divided through by volume fraction prior to discretisation and linearisation, avoiding the problem of singular equations as $\alpha^k \to 0$. This approach was not pursued here because, as Venier *et al.* [93] show, the two-fluid model should be solved in conservative form to ensure good prediction of transient behaviours. However, if the equations are discretised in conservative form, a similar approach might be taken by dividing the resulting algebraic equations by the diagonal volume fraction, *i.e.* $\alpha^{k,P}$. This would ensure for example that the transient term always contributes a non-zero value to the discretised equations, preventing

singular equations if the phase disappears. Care would still have to be taken in the treatment of the advection terms as the ratio $\frac{\alpha^{k,f}}{\alpha^{k,P}}$ would need to be evaluated, however as Oliveira and Issa [69] point out evaluating a similarly problematic term, use of the average of face values to evaluate the denominator ensures the ratio reaches zero before the denominator.

Multiphase flows were shown to present multiple difficulties in the MWI, in particular the discontinuous source term and density fields that characterise multiphase flows. As shown, these features result in discontinuous pressure gradients that cannot be represented by the linear interpolation used to discretise the pressure gradient at cell centres. The proposed modifications in the form of rediscretising the source terms and using density weighting in MWI are designed to overcome these shortcomings and are shown to be successful. However there are trade-offs inherent in these solutions: the rediscretised source terms are diffuse relative to the input sources whilst the density weighting stabilises the solution by forcing the pressure gradient across a density jump to take the value in the lighter fluid. An alternative approach would be to reexamine the discretisation of the pressure gradient itself, as these issues demonstrate the current discretisation fails in these situations. A potential remedy would be to combine the current discretisation using interpolation to evaluate face values with an extrapolation based approach evaluating face values by extrapolating from cell centres. Combined with a suitable indicator function this would allow retaining the current discretisation where the pressure gradient varies smoothly and switching to extrapolation at discontinuities. This should allow the use of MWI without rediscretising the source terms or density weighting and could be compared with the current approach to investigate the accuracy and robustness of both approaches.

Bibliography

[1] Anderson, J. D. (2003). *Modern Compressible Flow: With a Historical Perspective*. McGraw-Hill New York.

[2] Anderson, T. B. and Jackson, R. O. Y. (1967). A fluid mechanical description of fludized beds. *I&EC Fundamentals*, **6**(4), 524–539.

[3] Balachandar, S. and Eaton, J. K. (2010). Turbulent Dispersed Multiphase Flow. *Annual Review of Fluid Mechanics*, **42**(1), 111–133.

[4] Balay, S., Abhyankar, S., Adams, M. F., Brown, J., Brune, P., Buschelman, K., Dalcin, L., Eijkhout, V., Kaushik, D., Knepley, M. G., May, D. A., McInnes, L. C., Gropp, W. D., Rupp, K., Sanan, P., Smith, B. F., Zampini, S., Zhang, H., and Zhang, H. (2017a). PETSc Users Manual. Technical Report ANL-95/11 - Revision 3.8, Argonne National Laboratory.

[5] Balay, S., Abhyankar, S., Adams, M. F., Brown, J., Brune, P., Buschelman, K., Dalcin, L., Eijkhout, V., Gropp, W. D., Kaushik, D., Knepley, M. G., McInnes, L. C., Rupp, K., Smith, B. F., Zampini, S., Zhang, H., and Zhang, H. (2017b). PETSc Web page. `http://www.mcs.anl.gov/petsc`.

[6] Benavides, A. (2009). *Eulerian-Eulerian Modelling of Turbulent Gas-Particle Flow*. Ph.D. thesis, Chalmers University of Technology.

[7] Benavides, A. and van Wachem, B. (2008). Numerical simulation and validation of dilute turbulent gas–particle flow with inelastic collisions and turbulence modulation. *Powder Technology*, **182**(2), 294–306.

[8] Benavides, A. and van Wachem, B. (2009). Eulerian-Eulerian prediction of dilute turbulent

gas-particle flow in a backward-facing step. *International Journal of Heat and Fluid Flow*, **30**(3), 452–461.

[9] Benavides, A., van Wachem, B., Nijenhuis, J., and van Ommen, J. (2008). Comparison of experimental and simulation results for turbulent gas-solid riser flow. In *Circulating Fluidized Bed Technology IX. Proceedings of the 9th International Conference on Circulating Fluidized Beds, CFB-9. May 13-16, 2008. Hamburg, Germany.*

[10] Boree, J., Ishima, T., and Flour, I. (2001). The effect of mass loading and inter-particle collisions on the development of the polydispersed two-phase flow downstream of a confined bluff body. *Journal of Fluid Mechanics*, **443**(01), 129–165.

[11] Carver, M. (1982). A method of limiting intermediate values of volume fraction in iterative two-fluid computations. *Journal of Mechanical Engineering Science*, **24**(4), 221–224.

[12] Chen, Z. and Przekwas, A. J. (2010). A coupled pressure-based computational method for incompressible/compressible flows. *Journal of Computational Physics*, **229**(24), 9150–9165.

[13] Choi, J.-H., Byun, K.-R., and Hwang, H.-J. (2003). Quality-improved local refinement of tetrahedral mesh based on element-wise refinement switching. *Journal of Computational Physics*, **192**(1), 312–324.

[14] Choi, S. (1999). Note on the use of momentum interpolation method for unsteady flows. *Numerical Heat Transfer Part A*, **36**, 545–550.

[15] Chorin, A. J. (1997). A Numerical Method for Solving Incompressible Viscous Flow Problems. *Journal of Computational Physics*, **135**, 118–125.

[16] Clift, R., Grace, J., and Weber, M. (1978). *Bubbles, Drops and Particles*. Academic Press, New York.

[17] Cordier, F., Degond, P., and Kumbaro, A. (2012). An Asymptotic-Preserving all-speed scheme for the Euler and Navier–Stokes equations. *Journal of Computational Physics*, **231**(17), 5685–5704.

[18] Crowe, C. T. (2000). On models for turbulence modulation in fluid-particle flows. *International Journal of Multiphase Flow*, **26**(5), 719–727.

[19] Csanady, G. T. (1963). Turbulent diffusion of heavy particles in the atmosphere. *Journal of Atmospheric Sciences*, **20**, 201–208.

[20] Cubero, A. and Fueyo, N. (2007). A Compact Momentum Interpolation Procedure for Unsteady Flows and Relaxation. *Numerical Heat Transfer, Part B: Fundamentals*, **52**(6), 507–529.

[21] Darwish, M. and Moukalled, F. (2014). A fully coupled navier-stokes solver for fluid flow at all speeds. *Numerical Heat Transfer, Part B: Fundamentals*, **65**(5), 410–444.

[22] Darwish, M., Moukalled, F., and Sekar, B. (2001). A Unified Formulation of the Segregated Class of Algorithms for Multifluid Flow At All Speeds. *Numerical Heat Transfer, Part B: Fundamentals*, **40**(2), 99–137.

[23] Darwish, M., Rached, J., and Moukalled, F. (2009). Unstructured Adaptive Mesh Refinement and Coarsening for Fluid Flow at All Speeds Using a Coupled Solver. In T. Simos, G. Psihoyios, and C. Tsitouras, editors, *International Conference on Numerical Analysis and Applied Mathematics*, volume 577, pages 577–680, 18–22 September 2009, Rethymno, Greece. American Institute of Physics.

[24] Darwish, M., Aziz, A., and Moukalled, F. (2010). A Coupled Finite Volume Solver for the Simulation of Disperse Multiphase Flows. In *7th International Conference on Multiphase Flows 2010*, Tampa, FL USA.

[25] Darwish, M., Aziz, A., and Moukalled, F. (2015). A Coupled Pressure-Based Finite-Volume Solver for Incompressible Two-Phase Flow. *Numerical Heat Transfer, Part B: Fundamentals*, **67**(1), 47–74.

[26] Dembo, R., Eisenstat, S., and Steihaug, T. (1982). Inexact newton methods. *SIAM Journal on Numerical Analysis*, **19**(2), 400–408.

[27] Demirdžić, I. (1982). *A Finite Volume Method for Computation of Fluid Flow in Complex Geometries*. Ph.D. thesis, Imperial College London.

[28] Demirdžić, I. and Muzaferija, S. (1995). Numerical method for coupled fluid flow, heat transfer and stress analysis using unstructured moving meshes with cells of arbitrary topology. *Computer Methods in Applied Mechanics and Engineering*, **125**(1-4), 235–255.

[29] Demirdžić, I., Lilek, v., and Perić, M. (1993). A collocated finite volume method for predicting flows at all speeds. *International Journal for Numerical Methods in Fluids*, **16**(January), 1029–1050.

[30] Denner, F. (2013). *Balanced-Force Two-Phase Flow Modelling on Unstructured and Adaptive Meshes*. Ph.D. thesis, Imperial College London.

[31] Denner, F. and van Wachem, B. (2014a). Accurate advection of sharp interfaces on arbitrary meshes. In *2nd International Conference on Numerical Methods in Multiphase Flows*, 30 June - 2 July 2014, Darmstadt, Germany.

[32] Denner, F. and van Wachem, B. (2014b). Capillary time-step constraint with implicit and explicit treatment of surface tension. In *2nd International Conference on Numerical Methods in Multiphase Flows*, 30 June - 2 July 2014, Darmstadt, Germany.

[33] Denner, F. and van Wachem, B. (2015a). Numerical time-step restrictions as a result of capillary waves. *Journal of Computational Physics*, **285**, 24–40.

[34] Denner, F. and van Wachem, B. (2015b). TVD differencing on three-dimensional unstructured meshes with monotonicity-preserving correction of mesh skewness. *Journal of Computational Physics*, **298**, 466–479.

[35] Eisenstat, S. C. and Walker, H. F. (1996). Choosing the Forcing Terms in an Inexact Newton Method. *SIAM Journal on Scientific Computing*, **17**(1), 16–32.

[36] Elghobashi, S. and Abou-Arab, T. (1983). A two-equation turbulence model for two-phase flows. *Physics of Fluids*, **26**, 931.

[37] Ellison, J., Hall, C., and Porsching, T. (1987). An unconditionally stable convergent finite difference method for Navier-Stokes problems on curved domains. *SIAM Journal on Numerical Analysis*, **24**(6), 1233–1248.

[38] Evans, K. J., Knoll, D., and Pernice, M. (2006). Development of a 2-D algorithm to simulate convection and phase transition efficiently. *Journal of Computational Physics*, **219**(1), 404–417.

[39] Ferziger, J. and Perić, M. (2002). *Computational Methods for Fluid Dynamics*. Springer Verlag, Berlin Heidelberg New York, 3. edition.

[40] Fessler, J. R. and Eaton, J. K. (1999). Turbulence modification by particles in a backward-facing step flow. *Journal of Fluid Mechanics*, **394**, 97–117.

[41] García, M., Riber, E., Simonin, O., and Poinsot, T. (2007). Comparison between Euler/Euler and Euler/Lagrange LES Approaches for Confined Bluff-Body Gas-Solid Flow Prediction. In *ICMF*, pages 1–11.

[42] Gidaspow, D. (1994). *Multiphase Flow and Fluidization: Continuum and Kinetic Theory Descriptions*. Academic Press.

[43] Gropp, W., Kaushik, D., Keyes, D., and Smith, B. (2000). Performance Modeling and Tuning of an Unstructured Mesh CFD Application. *ACM/IEEE SC 2000 Conference (SC'00)*, pages 1–15.

[44] Harlow, F. H. and Welch, J. E. (1965). Numerical Calculation of Time-Dependent Viscous Incompressible Flow of Fluid with Free Surface. *Physics of Fluids*, **8**(12), 2182–2189.

[45] Hirt, C. and Nichols, B. (1981). Volume of fluid (VOF) method for the dynamics of free boundaries. *Journal of Computational Physics*, **39**(1), 201–225.

[46] Hrenya, C. and Sinclair, J. (1997). Effects of particle-phase turbulence in gas-solid flows. *AIChE journal*, **43**(4), 853–869.

[47] Ishii, M. (1975). *Thermo-Fluid Dynamic Theory of Two-Phase Flow*. Eyrolles, Paris.

[48] Ishii, M. and Hibiki, T. (2006). *Thermo-Fluid Dynamics of Two-Phase Flow*. Springer New York.

[49] Ishima, T., Boree, J., Fanouillere, P., and Flour, I. (13 - 16 April 1999). Presentation of a data base obtained in a confined bluff body flow laden with polydispersed solid particles.

[50] Ishima, T., Boree, J., Fanouillere, P., and Flour, I. (2017). Two-Phase Flow data base obtained on the Flow Loop Hercule. `web.archive.org/web/20011022033918fw_/http://www-mvt.iw.uni-halle.de:80/mvt-home_e.html`.

[51] Johnson, P. C. and Jackson, R. (1987). Frictional–collisional constitutive relations for granular materials, with application to plane shearing. *Journal of Fluid Mechanics*, **176**, 67–93.

[52] Johnson, P. C., Nott, P., and Jackson, R. (1990). Frictional-collisional equations of motion for particulate flows and their application to chutes. *Journal of Fluid Mechanics*, **210**, 501–535.

[53] Karimian, S. and Straatman, A. (2006). Discretization and parallel performance of an unstructured finite volume Navier–Stokes solver. *International Journal for Numerical Methods in Fluids*, **52**(6), 591–615.

[54] Kazemi-Kamyab, V., van Zuijlen, A. H., and Bijl, H. (2012). Higher Order Implicit Time Integration Schemes To Solve Incompressible Navier-Stokes on Co-Located Grids Using Consistent Unsteady Rhie-Chow. In *European Congress on Computational Methods in Applied Sciences and Engineering*.

[55] Klaij, C. M. and Vuik, C. (2013). SIMPLE-type preconditioners for cell-centered, colocated finite volume discretization of incompressible Reynolds-averaged Navier-Stokes equations. *International Journal for Numerical Methods in Fluids*, **71**(7), 830–849.

[56] Knoll, D. A. and Keyes, D. E. (2004). Jacobian-free Newton-Krylov methods: A survey of approaches and applications. *Journal of Computational Physics*, **193**(2), 357–397.

[57] Koch, D. (1990). Kinetic theory for a monodisperse gas–solid suspension. *Physics of Fluids A: Fluid Dynamics*, **2**, 1711.

[58] Kunii, D. and Levenspiel, O. (1991). *Fluidization Engineering*, volume 2. Butterworth-Heinemann Boston.

[59] Lai, Y., So, R., and Przekwas, A. (1995). Turbulent transonic flow simulation using a pressure-based method. *International Journal of Engineering Science*, **33**(4), 469–483.

[60] Lo, S. (1989). Mathematical basis of a multi-phase flow model. Technical report, Harwell Laboratory.

[61] Lun, C. K. K., Savage, S., Jeffery, D. J., and Chepurniy, N. (1984). Kinetic theories for granular flow: Inelastic particles in Couette flow and slightly inelastic particles in a general flowfield. *J. Fluid Mech*, **140**, 223–256.

[62] Majumdar, S. (1988). Role of Underrelaxation in Momentum Interpolation for Calculation of Flow With Nonstaggered Grids. *Numerical Heat Transfer*, **13**(1), 125–132.

[63] Maxey, M. R. (1987). The gravitational settling of aerosol particles in homogeneous turbulence and random flow fields. *Journal of Fluid Mechanics*, **174**, 441.

[64] Mencinger, J. and Zun, I. (2007). On the finite volume discretization of discontinuous body force field on collocated grid: Application to VOF method. *Journal of Computational Physics*, **221**(2), 524–538.

[65] Miller, T. F. and Schmidt, F. W. (1988). Use of a Pressure-Weighted Interpolation Method for the Solution of the Incompressible Navier-Stokes Equations on a Nonstaggered Grid System. *Numerical Heat Transfer*, **14**(2), 213–233.

[66] Moguen, Y., Kousksou, T., Bruel, P., Vierendeels, J., and Dick, E. (2012). Pressure-velocity coupling allowing acoustic calculation in low Mach number flow. *Journal of Computational Physics*, **231**(16), 5522–5541.

[67] Moukalled, F., Mangani, L., and Darwish, M. (2016). *The Finite Volume Method in Computational Fluid Dynamics: An Advanced Introduction with OpenFOAM and Matlab*. Springer.

[68] Nordlund, M., Stanic, M., Kuczaj, A., Frederix, E., and Geurts, B. (2016). Improved PISO algorithms for modeling density varying flow in conjugate fluid–porous domains. *Journal of Computational Physics*, **306**, 199–215.

[69] Oliveira, P. J. and Issa, R. I. (2003). Numerical aspects of an algorithm for the Eulerian simulation of two-phase flows. *International Journal for Numerical Methods in Fluids*, **43**(10-11), 1177–1198.

[70] Pascau, A. (2011). Cell face velocity alternatives in a structured colocated grid for the unsteady Navier-Stokes equations. *International Journal for Numerical Methods in Fluids*, **65**, 812–833.

[71] Patankar, S. (1980). *Numerical Heat Transfer and Fluid Flow*. Hemisphere Publishing Company.

[72] Perić, M., Kessler, R., and Scheuerer, G. (1988). Comparison of finite-volume numerical methods with staggered and colocated grids. *Computers & Fluids*, **16**(4), 389–403.

[73] Perot, B. (2000). Conservation properties of unstructured staggered mesh schemes. *Journal of Computational Physics*, **159**(1), 58–89.

[74] Prosperetti, A., Sundaresan, S., Pannala, S., and Zhang, D. (2007). Segregated methods for two-fluid models. In A. Prosperetti and G. Tryggvason, editors, *Computational Methods for Multiphase Flow*, pages 320–386. Cambridge University Press, Cambridge, UK.

[75] Rahman, M., Miettinen, A., and Siikonen, T. (1996). Modified SIMPLE formulation on a collocated grid with an assessment of the simplified QUICK scheme. *Numerical Heat Transfer Part B: Fundamentals*, **30**(3), 291–314.

[76] Rhie, C. M. and Chow, W. L. (1983). Numerical study of the turbulent flow past an airfoil with trailing edge separation. *AIAA Journal*, **21**(11), 1525–1532.

[77] Richardson, J. F. and Zaki, W. N. (1954). The sedimentation of a suspension of uniform spheres under conditions of viscous flow. *Chemical Engineering Science*, **3**(2), 65–73.

[78] Rundqvist, R., Ljus, C., and van Wachem, B. (2005). Experimental and numerical investigation of particle transport in a horizontal pipe. *AIChE journal*, **51**(12), 3101–3108.

[79] Schneider, G. E. and Raw, M. J. (1987a). Control volume finite-element method for heat transfer and fluid flow using colocated variables - 1. Computational procedure. *Numerical Heat Transfer*, **11**(4), 363–390.

[80] Schneider, G. E. and Raw, M. J. (1987b). Control volume finite-element method for heat transfer and fluid flow using colocated variables - 2. Application and validation. *Numerical Heat Transfer*, **11**(4), 391–400.

[81] Shen, W., Michelsen, J., and Sørensen, J. (2001). An improved Rhie-Chow interpolation for unsteady flow computations. *AIAA journal*, **39**(12).

[82] Simonin, O. (1996). Continuum modelling of dispersed two-phase flows. *Lecture series-van Kareman Institute for fluid dynamics*, **2**, K1–K47.

[83] Simonin, O., Deutsch, E., and Minier, J. (1993). Eulerian prediction of the fluid/particle correlated motion in turbulent two-phase flows. *Applied Scientific Research*, **51**(1-2), 275–283.

[84] Spalding, D. (1983). Developments in the IPSA procedure for numerical computation of multiphase-flow phenomena with interphase slip, unequal temperatures, etc. *Numerical Properties & Methodologies in Heat Transfer*, pages 421–436.

[85] Stanic, M., Nordlund, M., Frederix, E., Kuczaj, A., and Geurts, B. (2016). Evaluation of oscillation-free fluid-porous interface treatments for segregated finite volume flow solvers. *Computers & Fluids*, **131**, 169–179.

[86] van Wachem, B. and Gopala, V. (2006). A coupled solver approach for multiphase flow calculations on collocated grids. In *European Conference on Computational Fluid Dynamics, ECCOMAS CFD, TU Delft*, pages 1–16.

[87] van Wachem, B., Schouten, J., and Krishna, R. (1998). Eulerian simulations of bubbling behaviour in gas-solid fluidised beds. *Computers & Chemical Engineering*, **22s**, 299–307.

[88] van Wachem, B., Schouten, J., Krishna, R., van den Bleek, C., and Sinclair, J. (2000). Overview of CFD Models for Laminar Gas-Solid Systems. In *AMIF-ESF Workshop "Computing Methods for Two-Phase Flow"*, pages 1–8.

[89] van Wachem, B., Schouten, J., van den Bleek, C., Krishna, R., and Sinclair, J. (2001). Comparative Analysis of CFD Models of Dense Gas – Solid Systems. *AIChE Journal*, **47**(5).

[90] van Wachem, B., Benavides, A., and Gopala, V. (2007). A coupled solver approach for multiphase flow problems. In *6th International Conference on Multiphase Flows 2007*, page Paper No 183, Leipzig, Germany.

[91] van Wachem, B., Mallouppas, G., Denner, F., Evrard, F., and Bartholomew, P. (2016). http://www.multiflow.org/. *website*.

[92] Vanka, S. P. and Leaf, G. K. (1983). Fully-coupled solution of pressure-linked fluid flow equations. Technical Report ANL-83-73, Argonne National Lab., IL (USA).

[93] Venier, C. M., Marquez Damian, S., and Nigro, N. M. (2016). Numerical aspects of Eulerian gas–particles flow formulations. *Computers & Fluids*, **133**, 151–169.

[94] Versteeg, H. K. and Malalasekera, W. (2007). *An Introduction to Computational Fluid Dynamics: The Finite Volume Method*. Pearson Education, 2 edition.

[95] Wen, C. and Yu, Y. (1966). Mechanics of fluidization. *Chem. Eng. Prog. Symp. Ser.*, **62**(62), 100–111.

[96] Wenneker, I., Segal, A., and Wesseling, P. (2003). Conservation properties of a new unstructured staggered scheme. *Computers and Fluids*, **32**(1), 139–147.

[97] Wesseling, P. (2001). *Principles of Computational Fluid Dynamics*. Springer.

[98] Xiao, C.-N., Denner, F., and van Wachem, B. (2017). Fully-coupled pressure-based finite-volume framework for the simulation of fluid flows at all speeds in complex geometries. *Journal of Computational Physics*, **346**, 91–130.

[99] Yu, B., Kawaguchi, T., Tao, W.-Q., and Ozoe, H. (2002a). Checkerboard pressure predictions due to the underrelaxation factor and time step size for a nonstaggered grid with momentum interpolation method. *Numerical Heat Transfer Part B*, **41**, 85–94.

[100] Yu, B., Tao, W.-Q., Wei, J.-J., Kawaguchi, T., Tagawa, T., and Ozoe, H. (2002b). Discussion on momentum interpolation method for collocated grids of incompressible flow. *Numerical Heat Transfer Part B*, **42**, 141–166.

[101] Zhang, S., Zhao, X., and Bayyuk, S. (2014). Generalized formulations for the Rhie-Chow interpolation. *Journal of Computational Physics*, **258**, 880–914.

[102] Zwart, P. (1999). *The Integrated Space-Time Finite Volume Method*. Ph.D. thesis, University of Waterloo.